IMPROVED SPATIAL RESOLUTION FOR DOUBLE-SIDED STRIP DETECTORS USING LITHIUM INDIUM DISELENIDE SEMICONDUCTORS

A Dissertation Presented for the

Doctorate of Philosophy

Degree

The University of Tennessee, Knoxville

Jake Alexander Gallagher

May 2023

ACKNOWLEDGEMENTS

I would like to acknowledge and thank Dr. Eric Lukosi for his constant guidance and mentorship as my advisor. I would also like to thank my loving wife, Micah, for always supporting my dreams. Thank you to my father, James, for instilling in me my fascination for all things nuclear. Lastly, I would like to thank some of my fellow graduate students and friends from the University of Tennessee, Heath Davis, Corey Ahl, and Ryan Stewart, for their friendship and support. Without them, the probability of graduating in four years goes down drastically.

This research was conducted at the Institute for Advanced Materials and Manufacturing (IAMM) at the University of Tennessee-Knoxville. This material is based upon work supported by the U.S. Department of Energy, Office of Science, USA, Office of Basic Energy Sciences, USA, under Award Number DE-SC-0019446. Part of this work was conducted in the Micro-Processing Research Facility, a University of Tennessee Core Facility.

ABSTRACT

This research focuses on the evaluation of lithium indium diselenide (LISe) semiconductors in double-sided strip detector (DSSDs) designs as an example for the potential to achieve unparalleled neutron detection efficiency, spatial resolution, and timing resolution detection. LISe semiconductors offer high neutron detection efficiency due to the ~25% atomic ratio of Lithium-6, maximizing its efficiency of ~75% with 1 mm thickness at 2.8 angstroms. Furthermore, the 4.78 MeV Q-value enables high intrinsic gamma discrimination in a pixelated design (electron range). These characteristics make LISe an alternative option for neutron radiography, energy-resolved imaging, and other neutron interrogation techniques. This dissertation summarizes my current efforts to enhance LISe-based neutron imaging systems to achieve an end goal of sub-5 μm spatial resolution and sub-1 μs timing resolution. My research focuses on using MATLAB and Silvaco to simulate the expected response of a LISe DSSD. These various datasets are then trained to Machine Learning models in order to predict the neutron interaction location based upon the induced signal across multiple strip electrodes. In addition, various DSSD designs were simulated to determine the strip electrode width/pitch that optimizes the tradeoff between signal integrity and reconstruction of the neutron absorption location. The addition of electronic and statistical noise to the signal as well as varying the charge collection efficiency was also explored. The improvement upon current neutron imaging systems has the opportunity to open new avenues of research that are not possible today.

TABLE OF CONTENTS

LIST OF TABLES

LIST OF FIGURES

LIST OF ABBREVIATIONS

AC	Capacitive coupling
ACF	Anisotropic conductive film
ASIC	Application Specific Integrated Circuit
BEPO	British Experimental Pile 0
CCDs	Charge-coupled Devices
CCE	Charge collection efficiency
CERN	European Organization for Nuclear Research
CVT	Chemical vapor transport
CZT	CdZnTe
DAQ	Data acquisition board
DC	Direct coupling
DDTC	Double type column
DFT	Discrete Fourier Transformation
DOE	Department of Energy
DSSD	Double-sided strip detector
EDS	Energy dispersive X-ray spectroscopy
ERC	Electronic readout circuit
ERI	Energy Resonance Imaging
FPGA	Field-programmable gate array
FZ	Float-zone
HCPs	Heavy charged particles
HL-LHC	High-Luminosity Large Hadron Collider
HPGe	High-purity Germanium
HSDD	High-speed double-disk
IAMM	Institute of Advanced Materials and Manufacturing
ID	Identification

LHC	Large Hadron Collider
LIPSe	Lithium indium phosphorus selenium or $LiInP_2Se_6$
LISe	Lithium indium diselenide or $LiInSe_2$
LSF	Line Spread Function
MCP	Micro-channel plate
MIPs	Minimum ionizing particles
ML	Machine Learning
MPRF	Micro-Processing Research Facility
MTF	Modulation Transfer Function
NDT	Non-destructive testing
NU	Northwestern University
ORNL	Oak Ridge National Laboratory
PCB	Printed circuit board
PHS	Pulse height spectrum
PSF	Point Spread Function
PTRAC	Particle track output
RF	Radio frequency
RMSE	Root mean square error
SEM	Scanning electron microscope
SNS	Spallation Neutron Source
TOT	Time-over-threshold
TRISO	Tri-structural isotropic particle fuel
UTK	University of Tennessee – Knoxville
UV	Ultraviolet

CHAPTER ONE: BACKGROUND

1.1 Neutron Imaging

Shortly after the discovery of the neutron by English physicist Chadwick, J., in 1932, Kallmann, H., and Kuhn's, E., research birthed the field of neutron imaging [1-4]. Early neutron radiographs suffered from poor resolution due to weak/uncollimated beams [5]. Kallmann, H., and Kuhn's, E., research was put on hold during the Second World War. It would not continue until 1956 when Thewlis, J., and Derbyshire, R. T. P., used thin layers of boron to create neutron radiographs using the 8 MW, graphite-moderated British Experimental Pile 0 (BEPO) reactor [6]. This method was used to take neutron radiographs of Boral sheets and uranium, which demonstrated this technique as a tool for the non-destructive testing (NDT) of materials. Previously, this field of study was not practical due to the low intensity of the neutron sources. This field of study became functional with the implementation of high flux reactors such as the High Flux Isotope Reactor and high energy pulsed neutron sources.

One of these high-energy pulsed neutron sources is the Spallation Neutron Source (SNS) at Oak Ridge National Laboratory (ORNL). The SNS produces neutrons by delivering short proton pulses to a liquid mercury target [7]. This process starts with negatively charged hydrogen ions that are accelerated from 1 MeV to 1 GeV by a linear accelerator [8]. From here, they are impinged upon a 20-ton liquid mercury target where the high energy protons hit the nucleus of mercury atoms [9]. For every mercury atom that these protons hit, twenty to thirty neutrons will be released. After traveling down a flight-tube, these fast and slow neutrons will arrive at a detector at slightly different times. Since the higher energy neutrons are traveling faster, they reach the detector before lower energy neutrons. The neutron cross sections for interactions with nuclei are both energy and isotopic dependent. Therefore, an energy-sensitive detector can be used to identify the signature of various isotopes. This principle is used for neutron stimulated emission computed tomography [10]. In pixelated detectors, a Timepix Application Specific

Integrated Circuit (ASIC) chip is used to correlate the neutron energy spectrum at each pixel within the device [11]. So, by precise timing of this neutron pulse, one can determine isotopic information from the object of interest due to resonant neutron absorptions [12]. A high-speed double-disk (HSDD) chopper can be used to segregate a specific energy range for the neutrons. However, this technique will usually remove quite a large majority of the epithermal neutrons, so it is only used on an experiment-by-experiment basis [13].

Neutron imaging is the direct production of images by transmitting a neutron beam through an object and onto a detector medium, in my case, LISe. Reconstructing the image in two-dimensions is referred to as radiography, and the reconstruction of the image in three-dimensions is referred to as tomography [14, 15]. Neutron radiography produces a two-dimensional attenuation map of how far neutron radiation has penetrated the sample. Neutron detectors ranging from plastics, scintillators, semiconductors, and gas detectors, are currently employed at beamlines around the world. Each detector has advantages and drawbacks, some of those being timing, spatial resolutions, neutron detection efficiency, and neutron/gamma discrimination [16]. There is currently not a single detector that covers all experimental requirements for imaging with neutrons. For these reasons, the DOE has called for the development of next-generation thermal neutron imaging sensors [17].

For neutron radiography and tomography, the incident flux, wavelength spectrum spread ($\frac{\Delta\lambda}{\lambda}$), and beam divergence are the key parameters to consider [15, 18]. In Equation (1), neutron flux (Φ) is equal to the neutron density (n) multiplied by the neutron velocity (v). From Equation (2) , the deBroglie equation, the neutron wavelength (λ) is equal to Planck's constant (h) divided by the neutron mass (m) times its velocity (v). Lastly, in Equation (3) the beam divergence (ϕ) is approximately the neutron wavelength (λ) divided by width of the imaging slit (d). The flux and wavelength of the neutron beam are directly related to one another, because as ($\frac{\Delta\lambda}{\lambda}$) gets smaller, so does the incident flux. In addition, this holds true for the spatial resolution. A higher spatial resolution is the result of the smaller pixel sizes, which means that the integrated flux at the pixel will be smaller as well.

$$\Phi = nv \tag{1}$$

$$\lambda = \frac{h}{mv} \tag{2}$$

$$\phi \sim \frac{\lambda}{d} \tag{3}$$

Neutron imaging systems share many similarities with x-ray imaging systems, the primary difference being the interaction mode with the object of interest [19]. X-rays interact with the electron cloud of the atoms, while neutrons interact with the atomic nuclei. Unlike x-rays, neutrons can be attenuated by light atoms such as hydrogen and carbon. This allows for neutron imaging to have an advantage over x-ray imaging for visualizing the inside of a material that is comprised of high Z materials [20]. Additionally, neutrons are sensitive to light elements and easily penetrate thick samples, compared to X-rays. These properties allow users to image very complex materials. Over the past 35 years, neutron sources have increased the brightness of their pulses by over 100 times [21]. These sources have advanced to the point where the current detectors are the most significant limitation for neutron experiments [17]. Current neutron imaging techniques have limited applications mainly due to their poor spatial resolution. However, neutron imaging is a fundamental non-destructive characterization technique that is used at neutron scattering facilities around the world to image a wide range of sample materials [15, 19, 22]. Due to the uncharged state of neutrons, they are not easily detected by conventional detectors, and unique detectors are required to detect them. Recently, there has been a call by the Department of Energy (DOE) to develop next-generation thermal and cold neutron imaging systems [17]. Given that these devices require thermal or cold neutrons to operate, they are typically only operating at expensive neutron scattering facilities. This section will also discuss some of the research regarding the use of energy resonance imaging (ERI) for the non-destructive assay of materials. This field of study has been known by many different names: Neutron Energy Resonance Imaging, Energy-Resolved Neutron Imaging, Neutron

Absorption Imaging, along with Resonance Absorption Imaging [23-25]. All of these fields refer to the same method of using neutron resonance peaks to identify isotopic composition information [19]. The form of ERI that will be discussed within this dissertation makes use of epithermal neutrons ranging from 1 eV to 1,000 eV and thermal neutrons. By varying the neutron energy, we use the resonances inside the neutron energy spectra to identify isotopes within the object of interest [26]. Thermal and epithermal neutrons are required to obtain spectral data in the neutron resonance region, given absorption is quite unlikely at fast neutron energies.

For a standard neutron radiography experiment, a total of 36 radiographs are taken by rotating the sample of interest in 5° steps over the course of 0° to 175°. The time stamp of each radiograph is then correlated to the neutron energy using the time-of-flight method. Given the low count rate for most of the pixels in a detector, the neutron energy spectrum is usually summed across a pixel or two in order to have a good signal-to-noise ratio [27]. The off-line analysis involves analyzing the data to find dips in the neutron absorption as a function of time, so a dark flash in the image is produced by the neutron absorption of a specific isotope. The data that would correspond to that neutron absorption would then be summed in order to map individual isotopes of interest.

1.2 Fundamentals of Neutron Interactions

Since we are interested in detecting neutrons, it is important to understand how they interact with matter. The secondary radiations resulting from neutron interactions with matter are heavy charged particles (HCPs) [19]. Neutron detectors will utilize the conversion of the incident neutron into secondary charged particles, which are easier to detect. This is the basis for neutron imaging and the semiconductor, LISe, on which this research was performed. Neutrons are usually divided into two categories: fast and slow (thermal), with a cut-off of ~0.5 eV between the two. This 0.5 eV cut-off corresponds to the ^{113}Cd cut-off, where neutrons below this energy will be absorbed, and those above will be transmitted.

While most applications of neutron imaging employ slow/thermal neutrons, reactor beamlines often have fast neutrons in the mix; for these reasons, it is essential to discuss fast neutrons. Fission reactions usually produce fast neutrons with initial energy ranging from 0.1 – 3 MeV. Since fast neutrons possess a significant amount of kinetic energy, the capture process probability for nuclear reactions is relatively low. Fast neutrons are usually moderated or slowed down to lower energies before they can be captured [28]. Low Z materials such as hydrogen are good at detecting neutrons. As stated before, we typically moderate the neutron down to the thermal energy range, which has an increased probability of the neutron being captured and inducing an interaction that is detectable.

Unlike fast neutrons, thermal neutrons have an energy of 0.025 eV. These slow neutrons are useful because they create secondary radiations that can be directly detected [19]. These secondary radiations are usually in the form of HCPs, which tend to travel in a straight line and lose their energy through the direct ionization of atomic electrons. These HCPs must have a sufficiently high Q-value such that direct ionization is possible. The nuclear cross-section is used to determine the probability that a nuclear reaction will occur. This cross-section is calculated independently for every isotope. In neutron imaging, we want to employ a detector with a high thermal neutron capture cross-section [29]. The main isotopes that are used for neutron imaging are ^{157}Gd (254,000 barns), ^{113}Cd (20,600 barns), ^{3}He (5,333 barns), ^{10}B (3,837 barns), and ^{6}Li (940 barns) [30, 31]. When these isotopes interact with neutrons, they produce a particle or particles that we can detect. For instance, in ^{6}Li-based semiconductors, the neutron capture reaction results in an alpha particle and triton that generate electron/hole pairs as they move through the detector medium. When designing thermal neutron imaging detectors, one will typically incorporate one or more of these isotopes into the detector medium in order to sense neutrons [31, 32]. Most neutron detectors consist of low Z isotopes, which are able to sense neutrons selectively.

1.3 Neutron Detectors

Compared to most other forms of radiation, neutrons are able to penetrate and have the capability to distinguish between different materials with similar chemical and physical

properties. The interaction of neutrons with the nuclei is governed not by the laws of classical physics but by quantum mechanics. Due to the uncharged nature of neutrons, they are not easily detected using conventional detectors such as high-purity germanium (HPGe) [33, 34]. The only practical method for detecting neutrons is by observing the ionization in the detection medium caused by the reaction products that follow neutron capture or inelastic neutron scatter. There are two main methods for neutron detection; direct and indirect detection. For scintillators, the incoming energy is converted into visible wavelength photons which are then converted to electrons by the charge-coupled devices (CCDs) that these scintillators are usually fixed to. For semiconductors, the indirect method involves placing a thin layer of neutron-absorbing material on top of the active detector medium. This layer of neutron-absorbing material is usually either Li^{6}, B^{10}, or Gd^{157} [5]. Neutrons are converted into charged particles in this thin layer of absorbing material following neutron capture. These charge particles are then detected by the detector medium. The practicality of this technique limits the detector efficiency to approximately 4% [35]. It is worth noting that while Gd^{157} has the highest neutron capture cross-section, it also emits gamma-rays which can overwhelm the detector neutron response. Direct neutron detection is where the neutron absorbing material is part of the detector and operates as both the neutron absorber and detector. Semiconductors fall under this detection method, and these systems greatly increase the detector efficiency when compared to indirect neutron detection systems, also called neutron conversion systems [36].

There are many different neutron detection systems currently on the market; additionally, there are many parameters to consider when comparing the performance of different systems. High neutron detection efficiency results in lower data-collection times, allowing for more experiments to be performed compared to systems with low neutron detection efficiency. Excellent temporal resolution allows for the detection of more minor features such as defects, impurities, superlattices, and clusters within the object of interest. Gamma-ray discrimination is a function of the energy released in the thermal neutron absorption spectrum and how the detector responds to neutron interaction and background gamma-rays. Neutron detection efficiency is one of the main parameters to consider when selecting viable neutron imaging systems, where detection sensitivity is dependent upon

the gamma-ray absorption efficiency. CdZnTe (CZT) detectors are a good x-ray and gamma-ray medium, which creates a high gamma-ray background that masks the presence of neutrons; thereby making it challenging for CZT detectors to distinguish between neutrons and gamma-rays [37, 38]. GS20 is a ^{6}Li-loaded glass scintillator that is used in a wide variety of applications ranging from neutron porosity measurements in the oil well logging industry to a time-of-flight single-crystal diffraction Anger camera at SNS [39, 40]. This loaded glass scintillator is very fast (70 ns) and offers neutron/gamma discrimination; however, it has a low light output of 6,000 photons per MeV and internal defects that are challenging to overcome [41]. Current ZnS:LiF-based systems are bright with a theoretical light yield of 100,000 photons per MeV but have limited timing properties and spatial resolution [38, 42]. Due to its Li^{6} enrichment (95%), a low Z-value, and a high Q-value, LISe possesses inherent neutron and gamma-ray pulse discrimination properties. The Q-value for LISe is 4.78 MeV, which is due to its thermal capture reaction energy. Ideally, this 4.78 MeV neutron capture reaction results in a Gaussian distribution that is separate from the gamma-ray and noise floor, allowing for pulse discrimination.

Helium-3 neutron detectors are widely considered the most versatile neutron imaging system and are used at neutron scattering facilities worldwide [43]. This is mainly due to its high capture cross-section for thermal neutrons, non-toxicity, and low-Z, which leads to excellent neutron/gamma discrimination. Helium-3 is collected as a byproduct from the radioactive decay of tritium at the Savannah River Site in South Carolina [44]. As a direct result of the nuclear weapons stockpile reduction, the production of helium-3 from tritium decay has declined. To develop a neutron detector, we must create them out of materials with high absorption cross-sections. Because of this, lithium-6 has been explored to replace helium-3 in neutron detectors. Although lithium-6 has a lower thermal neutron capture cross-section than helium-3, lithium-6 has a higher atomic density. This results in better thermal neutron absorption for solid detectors.

LISe is a semiconductor that meets the proposed DOE requirements for next-generation thermal neutron imaging detectors [45, 46]. Therefore, LISe shows potential for addressing the current need for next-generation thermal neutron imaging sensors at neutron scattering facilities. LISe also can operate as both a scintillator and semiconductor with a

relatively low Z-value and high Q-value, which makes pulse height discrimination of gamma rays possible. Due to its high neutron detection efficiency, LISe would lower the imaging time compared to current systems.

1.3.1 Semiconductor Detectors

Semiconductors are defined by the conductivity/resistivity of the material. Resistivity and conductivity quantify the ability of a material to resist current flow in the presence of an external bias [47, 48]. The bandgap of the material governs these properties. This bandgap is the distance between the conduction and valence bands in energy space. The valence band is the highest energy state that an electron can occupy without becoming excited. While the lowest energy state that an electron can occupy is the conduction band. This conduction band is where electrons are loosely bound and can drift and diffuse between atoms. The distribution of electrons within the available states depends on the thermal energy available and is described by the Fermi-Dirac distribution described by Equation (4).

$$f(\epsilon) = \frac{1}{\exp\left(\frac{(\epsilon - E_F}{kT}\right) + 1} \tag{4}$$

In Equation (4), ϵ is the energy level, k is the Boltzmann constant, E_F is the fermi level, and T is the temperature. The Fermi-Dirac distribution shows that the density of electrons in the conduction band is directly proportional to the temperature. This relationship is vital to understanding the performance and operation of semiconductor devices. When an electron is excited into the conduction band, it leaves behind a positively charged vacant state in the valence band. This positively charged vacant state is referred to as a hole. The W-value is the average energy required to produce an electron/hole pair and is determined by the average energy spent by a charged particle to produce a single

electron-hole pair. This W-value can be estimated by using Equation (5), where E_g is the bandgap [49].

$$W = 2E_g + 1.43\ eV \quad (5)$$

When charge carriers are generated inside a semiconductor, they are driven to the electrodes by the internal electric field generated from the applied bias voltage. When a charged particle enters a biased semiconductor device, such as LISe, the ionization caused by these charged particles will create a pulse. If this pulse is large enough, the semiconductor device can be coupled with electronics to form a neutron detector. The coupling capacitor then collects this charged pulse as this pulse enters the electronic readout circuit (ERC). The main advantage of using semiconductors over traditional detection methods is that semiconductors have a high data rate, low power requirement, and small size. Since the current flowing through the semiconductor depends on the drift velocity, a larger mobility results in increased performance for semiconductors. Mobility is a function of the effective mass of charge carriers and the mean time between scattering events within the semiconductor. Simply put, it defines how charge carriers move through a semiconductor.

Holes exhibit a lower mobility-lifetime product compared to electrons, which is typical for tertiary compound semiconductors [50, 51]. Charge-carrier lifetime is a combination of defect states, spatial distribution, and their capture cross-sections. Larger values for the charge-carrier lifetime result in better semiconductor radiation sensors because this allows charge to be collected before recombining. In addition, the neutron converter, Li^6, is intrinsic to the semiconducting material as opposed to extrinsic. Due to this intrinsic neutron reactive material, the bulk of the semiconductor can capture thermal neutrons, resulting in an effective absorption efficiency of 82% at thermal energy for LISe [45].

The Shockley-Ramo Theorem allows us to derive the induced signal of any electrode design from the motion of charge carriers through the bulk. This induced charge is multiplied by the fraction of potential it has moved through. Three main things go into

calculating the induced signal: the electric potential, weighting field, and weighting potential; this is because charge carriers will follow the electric field line until they are collected by the collecting electrode. The electric and weighting potential are found using SILVACO to solve Poisson's equation, current continuity equation, energy-balance equation, and lattice heat equation for electrons and holes.

The current induced on a given electrode is found by using Equation (6). Where q is the charge of the carrier, $\vec{v}$ is the velocity, and $\vec{E}_0$ is the weighting field. Another way to describe this is that the induced charge (Q) is equal to the charge of the carrier multiplied by the difference in the weighting potential (φ_0) from the start to the end of the carrier path, found in Equation (7). Using Equation (8), the electric field ($\vec{E}$) at any point is found by taking the gradient of the electric potential (φ). The text "Radiation Detection and Measurements, Appendix D" details these Shockley-Ramo Theorem derivations [38]. These three equations are the primary basis for the η-function developed to date.

$$i = q\vec{v} \cdot \vec{E}_0 \tag{6}$$

$$Q = q\Delta\varphi_0 \tag{7}$$

$$\vec{E} = -grad(\varphi) \tag{8}$$

A pulse height spectrum (PHS) built from the distribution of thousands of voltage pulses can be used to identify the radiation source or the composition of an unknown sample [52]. The accuracy of these spectra depends upon the charge carrier transport, charge collection efficiency, and the system noise. One of the main things to overcome regarding system noise is the leakage current. The leakage current is the flow of electrons in a semiconductor under bias without the presence of an excitation source such as ionizing radiation. The reduction of this leakage current improves the signal-to-noise ratio within our detector, increasing the detector performance. Because of the direct charge readout, solid-state detectors offer fast response times and high energy resolution [53]. LISe has a

wide bandgap (E_g > 2 eV) which makes it ideal for room temperature radiation detection. A wide bandgap reduces the leakage current and allows for smaller signals to be detected at room temperature [54]. This also removes the need for a turbo-vacuum pump or chiller during operation.

Spatial resolution quantifies the smallest feature a device can resolve. A low spatial resolution is desired for thermal neutron imaging applications. The knife-edge resolution test is the current method for determining spatial resolution [55]. The knife-edge is a highly attenuating material (typically Gd-based) with enough size to shield part of the detector from the incident neutron beam. To reduce blurring effects from the neutron beam, the knife-edge is placed as close to the surface of the detector medium as possible and is tilted to provide the appropriate edge sampling. The modulation transfer function is a method for comparing spatial resolution across varying imaging systems. The relationship between contrast and spatial frequencies defines the framework for the modulation transfer function (MTF), where contrast is a measurement of the intensity range for a given imaging system [56]. To obtain this modulation transfer function, the knife-edge response is extracted and differentiated. This differentiation leads to the line spread function, which has a Gaussian shape. Discrete Fourier Transformation (DFT) of the Line Spread Function (LSF) gives us the MTF for the detector [45, 55]. Spatial resolution is often defined as being 10% of the MTF.

Image processing is another crucial step to consider for neutron imaging. There are many ways to recreate images based on raw data, and a few of them are considered below. A Timepix ASIC coupled system is typically operated in counting mode to minimize the number of saturated pixels [57]. The system acquires multiple frames in quick succession, which are then averaged to create an image with good contrast. This ensures that hot pixels from noise and background radiation are minimized. The Point Spread Function (PSF), also known as the impulse response, is another way to reconstruct images from raw data [58]. The PSF involves taking the raw data from the detector response and performing a Fourier transform on it.

It should be noted that the detector resolution needs to be defined for this PSF to reconstruct images accurately. The MTF is derived from the Fourier transformation of the

PSF. In addition, the pixel and background efficiencies must be accurately calculated in order to have proper image reconstruction using this PSF. Poor Fourier transformation of the raw data will lead to errors in the image reconstruction phase. A more efficient method for image reconstruction is filtered back-projection. This method involves reconstructing slices from 0º to 180º versus using the typical rectangular coordinate system. These reconstructed slices are then layered on each other to create the image field referred to as the projection. The Shannon theorem is described by Equation (9) and is used to determine the optimum number of projections to stack, M [59]. Where N is the number of steps required to produce a single projection. Simply put, N and M determine the best resolution for the reconstructed image. Typically, the two-dimensional images are layered or stacked to form the three-dimensional images post image reconstruction. The two-dimensional images are completely reconstructed before they are stacked to create three-dimensional images.

$$M \geq \frac{\pi}{2} * N \tag{9}$$

The DOE has called for the development of next-generation thermal neutron imaging sensors, which is why we are designing a neutron imaging system with LISe [17]. Their report expressed the need for 1-10 µm spatial resolution systems while maintaining a sub-1 µs temporal resolution, with high count rate capabilities and excellent gamma/neutron discrimination. To meet these goals, we propose using a lithium-based semiconductor, such as LISe, in a double-sided strip detector (DSSD) design. LISe has excellent cold neutron detection capabilities, exhibiting a neutron mean free path of 474 µm at 3.3 Å. In addition, the 4.78 MeV Q-value for the ^{6}Li(n,^{3}H)^{4}He reaction results in high intrinsic gamma discrimination [45, 46, 50, 57, 60, 61].

1.4 Energy Resonance Imaging

The typical setup for ERI experiments includes a time-gated detector and pulsed

neutron source. The object of interest is placed near the detector window; for most of these experiments, it is within ~15 mm of the detector's window [62]. To turn the neutrons into detectable signals, one could use a scintillator system with a HSSD chopper at a reactor beamline or a micro-channel plate (MCP) amplifier coupled to a Timepix readout system [63]. As seen in Figure 1, a photocathode converts the incoming particle into electrons which are amplified by a chevron stack of MCPs [64, 65]. A readout system subsequently encodes this electron cloud (Timepix3). In Figure 1, a double-strip detector array utilizes charge division or charge propagation time to determine the neutron interaction location; typically, a Timepix3 chip collects the neutron energy at each pixel. The micro-channel plate amplifier consists of micro-capillary arrays doped with Boron-10 that amplify incoming particles by a factor of 103 – 107 electrons [66]. The main downside of this detector is that it requires a large turbo-vacuum pump and has a pixel-ghosting effect. This ghosting effect is an afterimage resulting from the electrons' interaction within the micro-capillary array [67]. When this device is put in front of a neutron beam, the object of interest will forever be burned into the micro-capillary array.

The detector array consists of four Timepix3 chips tiled together in a quad array. This encoded readout system has a timing resolution of ~1.56 ns. It should be noted that time resolution is the uncertainty in the peak width; for most spectral applications, we want a very fast timing resolution. The signal from the Timepix3 chips is then sent to a field-programmable gate array (FPGA) at a rate of 100 MHz. This FPGA, in-turn, sends the data to a graphical user interface with a frame rate of 1,200 frames/s [68]. This data is typically stored on an external computer, where off-line analysis is performed to calculate the neutron energy at a given time with ns timing resolution. The amount of data stored will depend upon the experiment and what the user would like to save. It is also worth noting that the Timepix4 chip will allow users to tile detectors on all four sides and offer sub-200 ps timing capabilities [69]. This system will be able to operate in a data driven or frame-based mode.

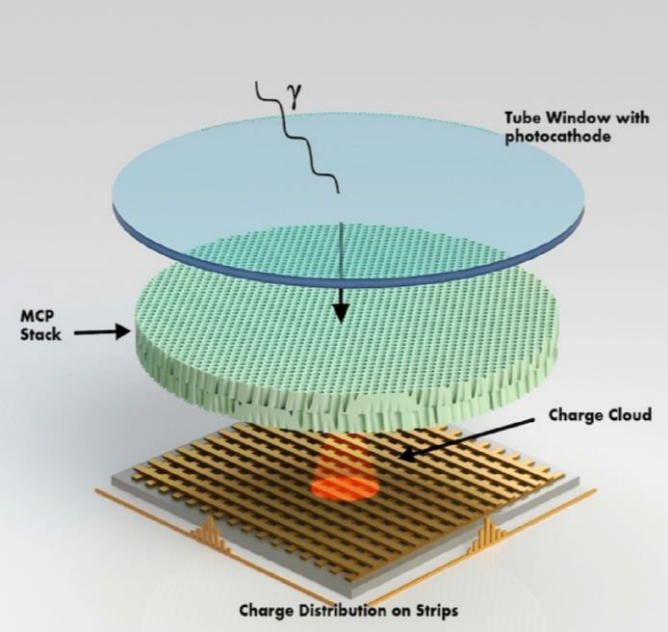

Figure 1. Schematic representation of a detector coupled with a micro-channel plate amplifier. The amplifier will amplify incoming electrons by a factor of $10^3 – 10^7$ [65].

$$E = \frac{mL^2}{2 * (T + \Delta T_0)^2} \tag{10}$$

In Equation (10), the neutron energy E is related to the mass of the neutron m, ΔT_0 is the time delay of the trigger pulse compared to the time of spallation, T is the time of the transmission spectra of interest, and L is the distance between the spallation target and the detector of interest [62]. Given that each detector pixel is operated independently, many simultaneous events are recorded at every pixel. In addition, with enough data for each pixel, all the time steps are binned together to form an accurate neutron transmission spectrum. This can then be used to determine isotopic and elemental compositions. The energy-dependent transmission ($Tr(E)$) for each sample can then be calculated from the Beer-Lambert Law given by Equation (11).

$$Tr(E) = exp\left[-\sum_i N_i d_i \sum_j \sigma_{ij}(E) A_{ij}\right] \tag{11}$$

Where N_i is the number of atoms per unit volume, d_i is the thickness of the elements along the neutron path, σ_{ij} is the neutron attenuation cross-section, and A_{ij} is the isotopic abundance of that specific element. As is typical for solid materials, the number of atoms per unit volume can be calculated from the material's density and atomic mass values. When experiments are performed with gases, the ideal gas equation can calculate the number of atoms per unit volume. Doing this allows for the quantitative characterization of neutron transmission spectra.

This MCP detector array currently has a 50% neutron detection efficiency for thermal neutrons and 70% for epithermal neutrons [70]. These systems have been shown to produce the most advanced energy resonance images to-date. Current research is being performed to replace these MCPs with LISe to eliminate the need for a turbo-vacuum pump and no longer have the permanent pixel ghosting effect. While MCPs have Boron-10 within the glass micro-capillaries, LISe has Lithium-6 within the semiconducting material. In

addition, LISe has been shown to have an 81% neutron detection efficiency for thermal neutrons, which is much higher than current MCPs [71]. For these reasons, LISe is being explored to replace current MCPs in thermal neutron imaging detectors for ERI. It is worth noting that a consortium of European Organization for Nuclear Research (CERN) researchers are working on releasing a Timepix4 chip, with the capability of ~200 ps timing resolution [72].

1.4.1 Energy Resonance Imaging Experiments

Several experiments are worth noting regarding this field of neutron imaging. The first experiment that will be discussed was performed by Tremsin et al. in 2017 [62]. This experiment consisted of taking various ~5-10 mm thick gold samples and analyzing their specific neutron absorption resonance in the spatial distribution of palladium and lead to map isotopic concentration. This experiment showed the possibility and application of measuring neutron transmission spectra simultaneously over an extensive range of energies, ranging from epithermal to thermal neutrons. This spans six orders of magnitude in the neutron energy spectrum and allows for the characterization of bulk microstructures, phases, textures, and strain distributions within a given sample. As stated previously, neutron resonances in the thermal and epithermal range of energies can be used to identify/map the elemental/isotopic distributions within the sample of interest. As can be seen in Figure 2, this experiment utilized thermal/epithermal neutron diffraction and neutron resonance spectroscopy to determine the internal structures and elemental compositions of various natural gold samples with a final spatial resolution of 100 μm.

One conclusion that can be drawn from Figure 2 (b) is that the gold from samples N2 and N3 were single morphologic crystals, whereas samples N1 and N2 appear to be polycrystalline in structure with the varying isotopic concentration of palladium and lead within. The Timepix detector provides the position and time-of-flight for every detected neutron. The energy of each neutron is calculated from the time-of-flight that is measured (triggered) by each spallation pulse. In order to eliminate the effects of spatial differences in the neutron beam, all transmission spectra were normalized compared to the open beam

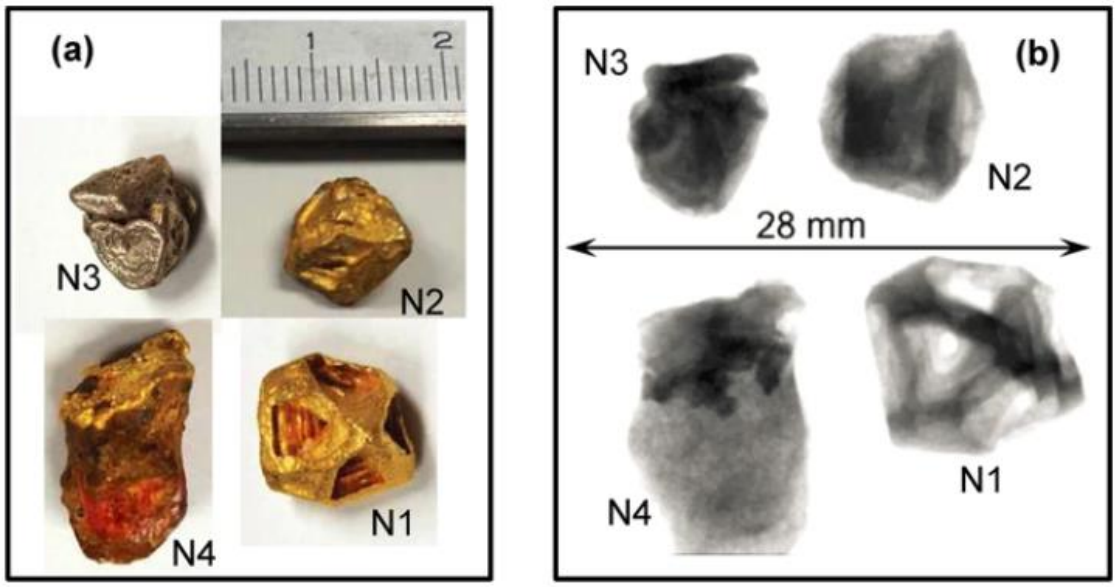

Figure 2. (a) Images of analyzed gold samples ranging from ~5-10 mm. (b) White beam neutron radiographs show the crystalline structure of various gold samples [51].

time-of-flight spectra. Based on the neutron transmission spectra measured for this experiment, palladium, and lead resonances were found in samples N2 and N3. This experiment showed the capability of thermal/epithermal neutrons to penetrate materials typically opaque to a conventional non-destructive assay of materials techniques. It should also be noted that the spatial distribution of palladium and lead can be reconstructed from the same experimental data shown in Figure 2. It is also possible to create a gold-only transmission image by taking the image in Figure 2 and subtracting the resonances for palladium and lead.

The second experiment worth mentioning was performed by Myhre et al. at the Spallation Neutron Source in early 2019 [23]. In this experiment, spectral data from the epithermal neutron energy range was used to map the isotopic composition of uranium and gadolinium in tri-structural isotropic particle fuel (TRISO) kernels. The end goal of this experiment was to topographically map elements within the structure of small spherical metal oxide kernels that are used in the production of TRISO kernels. The uranium is used as a fissile material, and the gadolinium is used as a burnable poison in these TRISO kernels. The distribution and mapping of these elements are essential considerations for fuel design. Current techniques employ destructive methods of assay for these materials, and this experiment was the first study on the non-destructive assay of uranium oxide kernels by ERI. Several grams of these spheres were loaded into special vanadium cans for neutron imaging at the Spallation Neutron Source. Vanadium was chosen as the can material because it is transparent in the epithermal neutron energy region [73]. Considering this experiment was quite similar to the previous gold experiment, multiple radiographs were taken at the angles of interaction. These radiographs were taken using the MCP detector that Tremsin et al. developed. Figure 3 consists of the total ERI data collected and is given as neutron energy versus neutron attenuation. The absorption peaks for gadolinium and uranium are both labeled on the graph. This technique allows for mapping isotopic concentration within tiny microspheres to assist in developing and designing next-generation reactor fuel. In addition, this research has paved the way for using ERI to study nuclear fuel materials at neutron scattering facilities around the world.

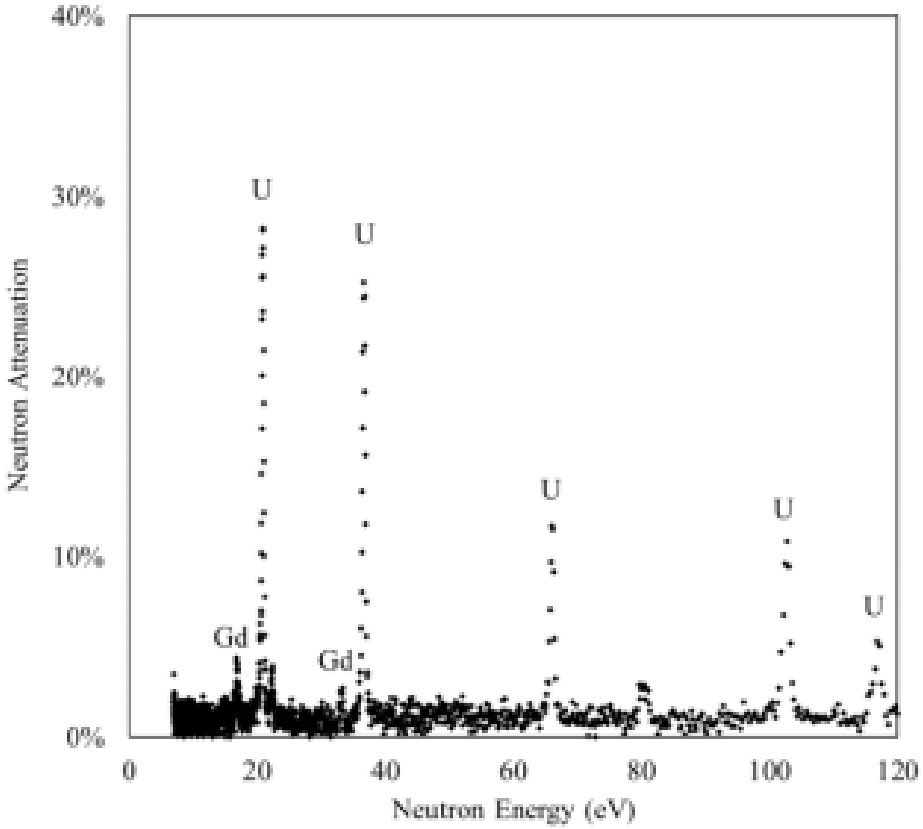

Figure 3. ERI spectra of uranium and gadolinium microspheres ranging from 0 eV to 120 eV. This attenuation spectra is the inverse of the counts seen by the detector, where the uranium “peaks” are labeled with U and gadolinium “peaks” are tagged with Gd [5].

Another ERI experiment was performed at the Lujan Neutron Scattering Center at Los Alamos National Laboratory by Tremsin et. al. in 2017 [74]. For this experiment, non-contact measurements of the partial pressure of krypton and xenon gases were taken while passing these gases through a neutron beam with various high-Z materials present. This experiment was a proof of principle demonstration using ERI as a non-destructive technique for measuring elemental compositions within fuel rods/assemblies. This technique was employed previously for solids; however, this was the first demonstration of mapping gases encapsulated within high-Z materials such as uranium, tungsten, and steel. For the most part, this technique will be beneficial for studying spend nuclear fuel assemblies. This experiment showed the multipurpose applications for ERI by mapping elements that are opaque to most other neutron imaging methods. The ability to image materials with phase separations is paramount for the non-destructive assay of spent fuel rods [75].

Using Equation (10), the energy of the detected neutron is determined from its time-of-flight. This experiment consisted of placing two separate tubular containers with natural xenon and krypton next to each other. These tubes were then mounted in various configurations relative to uranium fuel pellets, tungsten, and steel. The results from this experiment can be seen in Figure 4. A width of 270 ns base-to-base separated the neutron pulses for this experiment. It should be noted that the intrinsic time resolution of this detector setup increases with increasing neutron energy. As is typical with most common experiments, open beam normalization was performed to eliminate the effects of beam spectra and detector ghosting [76]. Since this had a short beam time, neighboring pixels were integrated to reduce the noise of the quantitative analysis. During this experiment, 3,000 spectra slices were recorded at each angle of interest to provide individual transmission images corresponding to a specific neutron energy range. A typical experiment employs choppers to mitigate the background; however, for this experiment, choppers were not fast enough to reduce the background without getting rid of the epithermal neutrons [13, 77]. In addition, post-experiment data binning allows for selective isotopic analysis of the reconstructed image. This experiment reinforces the use of ERI to image metals and that the gaseous partial pressure can be reconstructed in places where

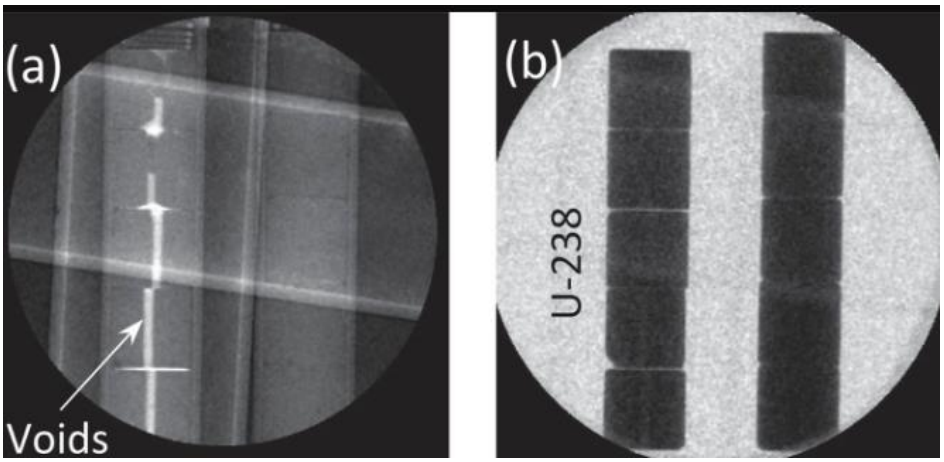

Figure 4 (a) Image of voids within uranium dioxide fuel pellets can be seen. (b) Element-specific images of U-238 were taken during this experiment by ERI. Both of these images have been normalized against the open beam to remove ghosting from the MCPs [74].

high-Z materials hide gases. This research paves the way for ERI to be used to image fuel assemblies and gases included within those assemblies.

The last experiment that will be discussed was performed at Lujan Neutron Scattering Center at Los Alamos National Laboratory by Tremsin et al. in 2017 [78]. In this experiment, phase separation during crystal growth was observed *in situ* by using ERI. Similar to all other ERI experiments, neutrons are time tagged by an external trigger to calculate the neutron energy precisely. In this experiment, a furnace with a seed-crystal inside was placed in front of the detector at this beamline. Crystals were then grown using the Vertical Bridgman crystal growth method. The Vertical Bridgman crystal growth method relies upon the slow solidification of the melt with a controlled temperature profile. The heat transfer between the melt/solid interface is vital for crystal growth, and changing this profile can result in added point defects and inclusions. Considering these crystals usually take weeks, if not months, to grow, the ability to determine the crystal structure in real-time will revolutionize this field while saving material scientists numerous months of research while optimizing crystal growth parameters. For this reason, various crystals were grown inside the furnace and imaged during their growth with ERI to perfect the crystal growing parameters.

As shown in Figure 5, the analysis of this spectrum allows for the investigation of properties such as crystallinity and phase separation. Crystallinity in the crystal boules is visible due to Bragg scattering within the lattice structure of the material [79]. Phase separation is visual once the sample has been reconstructed due to the temperature profile within the furnace. ERI allowed for the collection of multiple process parameters during crystal growth. These process parameters included the location and shape of liquid and solid phases, phase separations, point detects and inclusions and isotopic distributions during *in situ* growth. As we can see from some of these experiments, ERI is an exciting new scientific field. Not only will it save material scientists time, but it will also allow for the determination of multiple process parameters simultaneously. Additional experiments have explored using ERI to map the residual strain within bulk metal samples [80]. This tool helps quantify the residual stress within processed samples such as additive

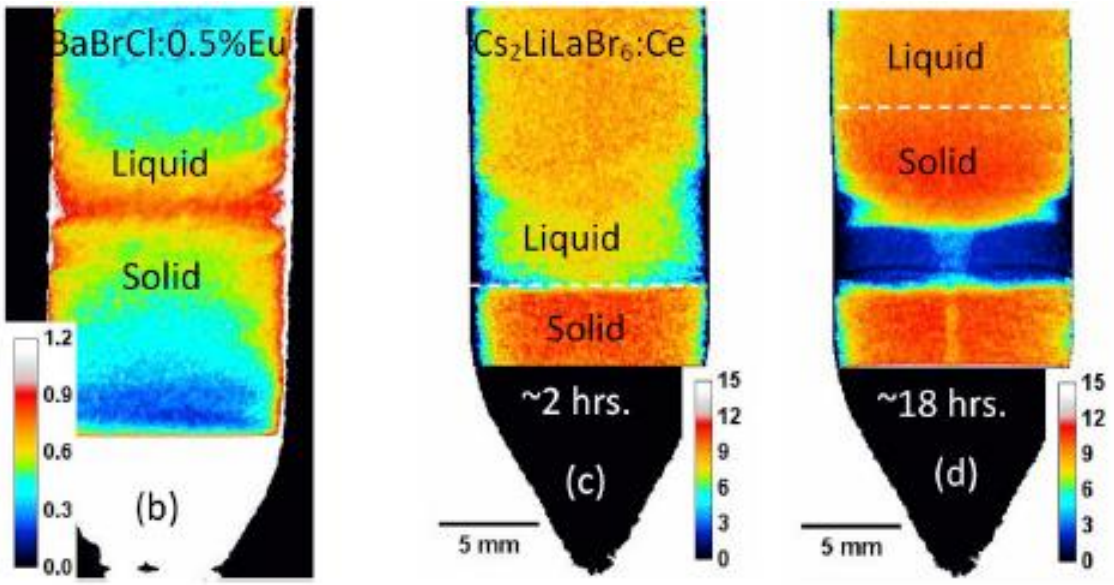

Figure 5. (b) *In situ* mapping of europium concentration from ERI data for BaBrCl:0.5%Eu can be seen above. The europium content appears to be distributed only along the edges of the solid crystal. (c-d) *In situ* mapping of lithium concentrations from ERI data for Cs2LiLaBr6:Ce can be seen above. The clear band (blue) of lithium separation seen in (d) is a result of phase separation [78].

manufacturing and welding. In addition, ERI has been used to map discontinuity, grain orientation, alloy composition, and hardness of various samples for a plethora of engineering/material science applications [81-83]. This section has shown numerous applications for ERI detectors and the need to improve our current systems. We propose to improve the existing systems by implementing LISe detectors at neutron imaging facilities around the world.

1.5 Strip Detectors

The method for enhancing the spatial resolution using a double-sided strip design is similar to the η-function developed by the high energy physics community for MIPs tracking using single-sided silicon strip detectors at the Large Hadron Collider (LHC) [84, 85]. Using this method, the charge is shared across multiple strips in a strip detector to enhance the spatial resolution by as much as a factor of ten. The goal of this application at the LHC is not position sensing of the MIPs but reconstructing the neutron interaction location from the induced signal on the strip electrodes. To properly spread the signal out across multiple electrodes, for our application, the electrode pitch must not be significantly larger than the combined ~47.5 μm range of the secondary charged particles (alpha/triton).

The value of this double-sided strip detector design lies in its ability to log and interpret the energy deposition profile of the secondary charged particles. This also gives us the significant benefit of reducing the number of readout channels from N^2 to 2N for direct coupling to the ASIC, which allows for a higher count rate. The DSSD design enables low-power processing electronics at a reduced data transfer rate, benefitting large-area neutron imaging. Using this design, the neutron-induced signals may be measured using ASIC and signal trace lines over direct coupling, which avoids the challenges associated with device density when using the direct coupling technique via flip-chip bonding.

According to the Shockley-Ramo theorem, the signal measured is through the formation of charge on the strip electrodes, maximizing the signal on a single strip as the charge cloud approaches the crystal boundary [86]. By time correlating the signal of each

strip in the double-sided strip design, we can determine the interaction voxel. This voxel has a square edge equal to the strip electrodes' pitch. Significant effort has been taken to develop an η-function to enhance the neutron capture point beyond this voxel (see Section II.I η-function Design).

1.5.1 Silicon Strip Detectors

Silicon tracking detectors are an established technology used for the inner tracking layers of particle tracking at the LHC and proposed for use in its upgrade to the High-Luminosity Large Hadron Collider (HL-LHC) [87-89]. The two primary devices under consideration are double-sided 3D strip detectors (double-sided, double-type column (DDTC) 3D sensors) and planar strip detectors. These are charge induction detectors where charge carriers absorb energy from the detector stored on the readout electrodes. In principle, the energy the silicon absorbs induces charge formation on the electrodes by moving through the bulk. This induction of charge is used to measure the radiation interaction. Figures 6-7 shows the respective detectors.

The columns in Figure 6 are etched into the front and back of the sensor and do not go through the entire detector. On the sensor's front face, the columns are connected to the readout strips and are usually referred to as readout columns. The columns on the back face of the sensor are connected to the backplane and provide the ohmic contact. It is worth noting that each column is centered between four other columns with the opposite dopant type. For this to work correctly, the doping concentration for all columns is higher than that of the bulk substrate. High-resistive float-zone (FZ) silicon was used as the bulk material for these detectors. One challenge with this design is that the charge collection of double-sided 3D detectors is slower than full 3D detectors. To increase the timing of these detectors, one can increase the depth of the columns [90]. These planar silicon detectors are typically 300 μm thick but can vary based on application. It is also worth noting that the HL-LHC will deliver a peak luminosity of approximately 5×10^{34} $cm^{-2}s^{-1}$, so these detectors must be very radiation tolerant [89, 91]. Shown in Figure 7, the idea behind planar

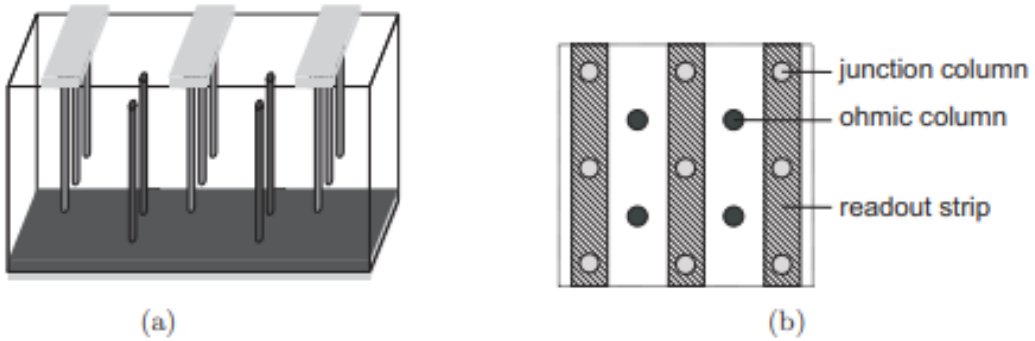

Figure 6. Principle of double-sided 3D strip detectors: (a) three-dimensional view, (b) horizontal projection. The junction columns extend into the substrate from the front side and are connected to readout strips. The ohmic columns are extended into the substrate from the backplane and are all connected together [88].

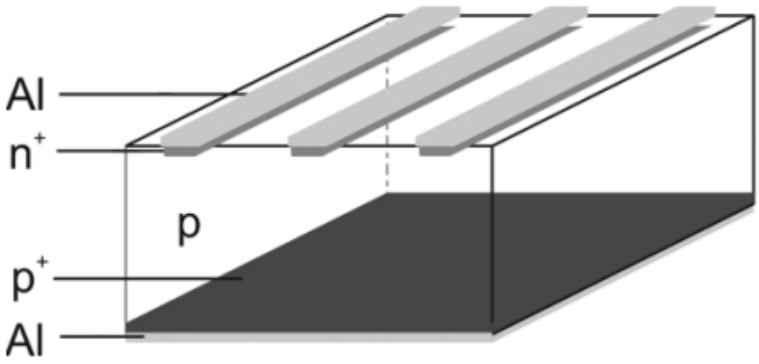

Figure 7. The principle design of a planar strip detector. P-stop implantations, which are present between the strips in the planar design, are omitted [89].

strip detectors is to share the induced charge across multiple strips (charge sharing) to determine the particle interaction with sub-pitch spatial resolution. Typical silicon strip detectors are either p^+-n-n^+ or p^+-p-n^+ design, where the sensor is either lightly n/p-doped. The doping concentration of the strips is much higher than the doping concentration of the bulk silicon. The strip pitches for these detectors at the LHC typically vary between 50-100 μm. In addition, strips are often metalized above the dopant implantations to form capacitive coupling (AC). Inversely, if the implantations are directly coupled to the readout electronics, this would be direct coupling (DC). Similar to the DDTC design, the doping concentration must be several orders of magnitude larger than the substrate doping concentration. In addition, strip detectors will usually have metalized strips above the implants, which leads to capacitive coupling between the strip implantations and the metalized strips. To prevent the depletion zone from reaching the planar metal contact, the p-n junction is formed close to the top surface, and the dopant layer (p^+ or n^+) is on the bottom surface. This depletion zone is where the semiconductor is depleted of free charge carriers. A p-n junction is a junction created between an n-type and a p-type region. Electrons and holes from each region diffuse into the other region and will recombine with excess charge carriers. The p-n junction for this design is kept narrow by the high dopant concentration on the bottom side of the detector, which leads to good ohmic contact performance from these devices.

The electrode pitch is the main factor determining these detectors' spatial resolution. A uniform probability distribution is assumed for a single particle interaction over a single strip. Suppose a single electrode collects the charge induced by a single interaction. In that case, the spatial resolution of the detector is the standard deviation of the uniform probability density distribution, Equation (12).

$$\sigma = \sqrt{\langle x^2 \rangle - \langle x \rangle^2} = \frac{p}{\sqrt{12}} \tag{12}$$

In this equation, σ is the uniform probability density distribution, x is the coordinate within one strip, and p is the strip pitch. For a strip pitch of 50 μm, the single strip or binary

resolution would be 14.43 μm and is highly dependent upon allowing diffusion to occur. Charge sharing across adjacent strips is utilized to improve the spatial resolution of these detectors. The main drawback of charge sharing is that it can lead to lower signals measured per readout strip, which can decrease detector efficiency. As one can see, a smaller strip pitch increases the charge-sharing probability. To properly understand these devices, one must realize there is a tradeoff between spatial resolution and the amount of signal measured per strip. In addition, one must consider the physical limitations of the strip electrode width/pitch using current strip electrode fabrication methods. Using photolithography at the University of Tennessee's Micro-Processing Research Facility (MPRF), we can consistently make 1 μm features and ~3-5 μm strips.

1.6 Lithium indium diselenide

LISe is room-temperature semiconductor comprised of three starting materials: lithium, indium, and selenium. Indium and selenium can be purchased at a 7N purity, whereas lithium-6 must be vacuum distilled to a minimum of 5N purity [92]. The first two elements, lithium and indium, are combined in a 1:1 molar ratio in a pyrolytic boron nitride crucible and heated. At this point, excess lithium is added to ensure proper molar ratios within LISe. Two moles of selenium are then added to the compound and heated. This is then sealed in an ampule, pressurized, and heated. The final product results in the polycrystalline form of LISe. Changing the stoichiometric concentration of selenium from two to anything other than two results in point defects and inclusions in the polycrystalline material [93]. These polycrystalline seed crystals are then grown into LISe crystal boules using the Vertical Bridgman growth method [94].

The Vertical Bridgman growth method relies upon slow solidification of the melt under a controlled temperature profile. This requires precise and accurate control of the crystal's temperature profile. Changing the thermal gradient across the melt/solid interface results in added point defects and inclusions. This reinforces the earlier statement that the heat transfer between the melt/solid interface is essential for crystal growth [78]. These crystal boules can be produced at 5-10 mm/day [95-98]. After they are grown, these crystal

boules are annealed in a lithium-rich environment to remove point defects and inclusions and maintain the stoichiometry (Se=1:1:2) within LISe. This annealing step is not required; however, it dramatically improves the performance of LISe as a semiconductor. This annealing step results in a yellow LISe crystal color.

The LISe boules are typically sliced into individual bulk sensors with a diameter of 13 mm and thickness ranging from 1.0 mm to 2.0 mm. These bulk sensors are then polished to enhance contact adhesion and etched in a 5% bromine/ethanol solution to remove surface contamination and defects. Photolithography is then performed, and gold ohmic contacts are sputtered onto the sensor. In the past, LISe sensors have been flip-chip bonded to a Timepix ASIC chip. This Timepix ASIC chip correlates the neutron energy spectrum at each pixel within a pixilated device [11]. This Timepix ASIC readout can be operated as a counting and high-resolution centroiding system. The Timepix ASIC associated with LISe operates in the counting mode. This Timepix coupling system resulted in the first high-resolution direct conversion semiconductor for neutron detection and imaging [57].

When a thermal neutron is absorbed by lithium-6 within the LISe polycrystalline structure, alpha particles and triton are emitted as the products. This reaction is shown in Equation (13). Note that the triton takes more (~57 percent) of the energy from the neutron capture reaction than the alpha particle.

$$ {}^{6}_{3}Li + {}^{1}_{0}n \rightarrow {}^{3}_{1}H(2.75\ MeV) + {}^{4}_{2}He(2.05\ MeV) \qquad (13) $$

Conservation of momentum is conserved such that the lighter product receives the most kinetic energy. Due to this, large Q-values are desirable for neutron detection because larger signals are produced within the semiconducting material. The energy deposition for LISe is large enough to allow for the discrimination between neutrons and gamma-rays. The energy these daughters carry is converted into electron/hole pairs within the bulk of LISe and swept away to the collector by the applied bias. Using a high isotopic enrichment of lithium-6 of 95% results in a higher neutron absorption cross-section because the neutron absorption cross-section for lithium-6 is 940 barns versus 45 millibarns for lithium-7.

Lithium-7 is not wanted since it does not produce heavy charged particles after a neutron absorption reaction. Due to this inherently large content of lithium-6 within the composition of LISe, approximately 75% of the incident thermal neutrons are captured. This theoretical yield can be calculated by taking the ratio ^{6}Li and dividing it by all other isotopes in LISe. This is called capture efficiency, not neutron detection efficiency, because not all neutron captures result in a signal above the noise floor due to poor charge collection efficiency (CCE). It should be noted that solid lithium-6 deuteride is used as the fusion fuel for the second stage of thermonuclear weapons, and as such, the export and use are tightly controlled [38, 99]. It should also be noted that the competing indium-115 (n,γ) reaction has a somewhat high thermal neutron absorption cross-section of 202 barns. This secondary gamma is highly likely to escape and is not wanted during the signal development step.

The desired ambient temperature thermal neutron detector bandgap is between 1.8 and 2.0 eV. This desired bandgap is such that thermal photons cannot excite electrons into the conduction band, resulting in indistinguishable signal and noise [100]. This phenomenon is often referred to as dark noise. The bandgap for LISe is 2.8 eV, which is above this ideal range, but it still works as a room-temperature semiconductor. Within LISe, the 4.78 MeV Q-value of the ^{6}Li reaction creates localized regions of electron-hole pairs. Creating these electron-hole pairs requires the daughters (alpha/triton) to transfer energy to the bound valence electron. Direct ionization is the process by which these excited daughters transfer their energy. This ionization energy is the energy required to produce an electron-hole pair within a semiconductor. The total charge generated by incident radiation, Q_0, is dependent upon the elementary charge of an electron, q, and the number of charge carriers generated, N. Based upon a given energy deposition, E, and the ionization energy, W, Equation (14) is defined below. This charge-to-energy proportionality is the fundamental design for radiation detection [101].

$$Q_0 = qN = \frac{qE}{W} \tag{14}$$

When enriched to 95% ^{6}Li, LISe could reach a thermal neutron capture efficiency of 99% if it did not have competing elements such as ^{115}In. ^{115}In also captures thermal neutrons and does not give off measurable daughters. This limits the total detector efficiency from 99% to 78%, which is still much higher than other current detector systems [102]. Current ^{10}B or ^{6}Li-containing detector systems have a maximum neutron detection efficiency of 32% [103].

1.7 Lithium indium phosphorus selenium

The computational evaluation for the DSSD design is relevant for all lithium-containing semiconductors. For these reasons, we have also explored using a new material, Lithium indium phosphorus selenium (LIPSe or $LiInP_2Se_6$), as a semiconductor in our DSSD design. LIPSe is a new material discovered by Mercouri G. Kanatzidis's Research Group out of Northwestern University (NU) in 2020, which offers high neutron detection efficiency, excellent energy resolution, and both hole/electron collection [36].

The precursors for LIPSe consist of Li_2Se, $Li_{1.03}In$, and P_2Se_5, and they are synthesized independently and then grown as bulk material. Detector-grade LIPSe is then grown by chemical vapor transport (CVT). The precursors are loaded into a carbon-coated, 13-mm fused silica tube where the bulk material is produced. A carbon-coated tube is required since it will withstand chemical attacks by Li. After purging the tube with nitrogen, it is flame-sealed under a vacuum. From here, the tube is heated to 750 ºC over 10 hours, held at this temperature for 24 hours, cooled to 350 ºC over 12 hours, and furnace-cooled to ambient temperatures. This bulk material is ground to a fine powder and loaded into a new tube for CVT growth. For an in-depth report on this CVT growth, please read "Direct thermal neutron detection by the 2D semiconductor $^{6}LiInP_2Se_6$" [36].

After growth, these 2D crystals have been fabricated into detector devices using evaporated planar gold contacts. These devices were tested with ^{241}Am sources and resolved the ^{241}Am peak for both holes and electrons, showing mobility for both charge carriers, and these results can be seen in Figure 8. Both charge carriers must have decent mobility for the DSSD design to work correctly. If they do not, you will collect most of

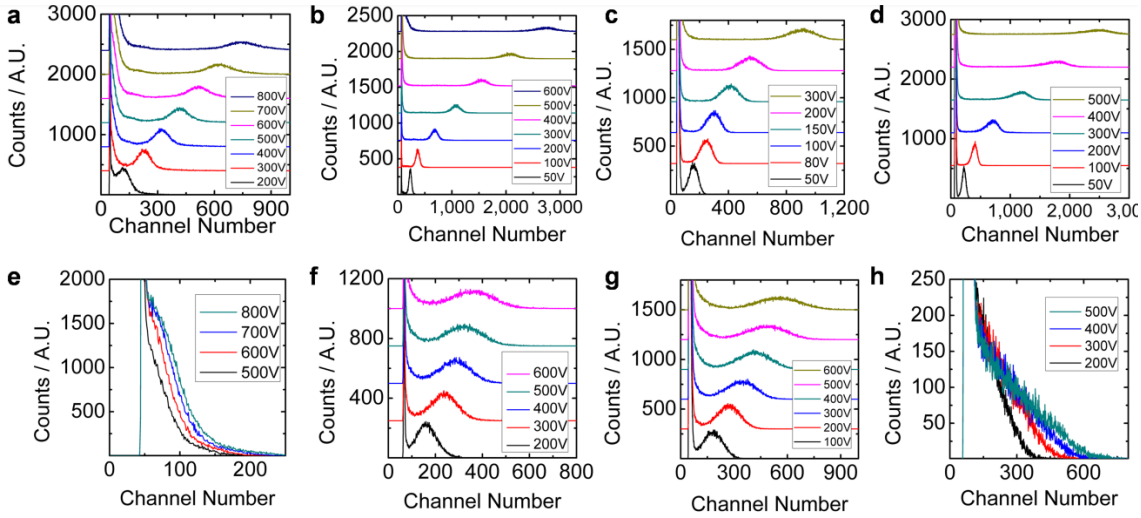

Figure 8. Pulse-height spectra for four LIPSe samples. Pulse height spectra are shown for electron (a-d) and hole (e-h) collection [36].

your charge on a single side of the device, significantly reducing the spatial resolution for a single dimension (X or Z) depending upon which side collects electrons or holes.

This lithium-based semiconductor has the same neutron capture reaction as LISe, seen in Equation(13, with the range of the alpha particle and triton being 6.7 μm and 37.5 μm, respectively. However, since it has shown decent mobility for both electrons and holes, we have selected it for our DSSD detector design. NU is performing current progress toward Bridgeman growth of this material.

CHAPTER TWO: RESULTS

This dissertation seeks to provide the neutron imaging community with the results of our effort to develop LISe or another ^{6}Li-based semiconductor as a DSSD which will be the first high-resolution (1-5 μm) neutron imaging sensor with excellent detection efficiency (>70%) and temporal resolution (<1 μs), and high-count rate capability. In addition, the lower effective-Z of LISe, in combination with the large reaction Q-value of 4.78 MeV, offers the potential for excellent gamma/neutron discrimination. As described in Chapter I, there is a demand for next-generation thermal neutron imaging detectors at neutron imaging facilities worldwide. For these reasons, this proposed research will focus on developing a state-of-the-art LISe-based neutron imaging DSSD. It is worth noting that this research work is applicable to any ^{6}Li-containing semiconductor.

First, we have developed a custom η-function for our double-sided strip design to achieve our end goal of 1-5 μm spatial resolution. This η-function defines a "center of gravity" of the pulse height distribution across the strip electrodes to identify the point of impact. For our material (LISe), the detected charged particles are alphas and tritons emitted antiparallel to each other. Using SRIM, we have determined that the total path length of the alpha particle and triton is 47.5 μm [104]. This length defines the achievable spatial resolution using ^{6}Li in scintillation screens. For semiconducting LISe, measuring the distribution of induced signals on the strip electrodes enables us to use this "center of gravity" concept to enhance the spatial resolution beyond 47.5 μm.

Second, we have taken the simulated induced signals from the strip electrodes and trained them to machine learning (ML) models to predict the interaction location. Using proper data preprocessing techniques on our dataset is important to train these models accurately. These models are then exported in C++ Code for deployment with our electronics package.

Third, we have computationally determined our double-sided strip detector's optimal strip pitch and width. It is not economically feasible to pattern and test a wide range of strip pitches and widths to determine which combination offers an optimal spatial

resolution. Due to this, we have simulated a range of electrode pitches from 15-75 μm and electrode widths from 10-50 μm. This will allow us to computationally determine the optimal width/pitch combination and use this design for our DSSD. It is worth noting that the current photolithography process at the UTK allows us to create 5 μm features on samples accurately.

2.1 η-function Design

This double-sided strip detector design works because of two secondary charged particles generated by the neutron absorption reaction within LISe. Electron-hole pairs are generated as these two particles slow down within the bulk material. By measuring the distributions of these induced signals on our strip electrodes, we can determine the interaction location and enhance the spatial resolution beyond the current ~34 μm maximum spatial resolution of LISe. The desired spatial resolution (sub-5 μm) is possible through charge sharing across adjacent strips due to the large range of the triton. To achieve our sub-5 μm spatial resolution goal, we must calculate the induced signal for a mesh throughout the LISe bulk and include a wide range of emission angles for the alpha/triton. The creation of our modified η-function started with modeling the weighting potential and electric field for a 500 μm thick LISe sensor with an applied bias of 1 V using SILVACO. The weighting potential is found by setting an electrode in the middle to a value of 1 V (source) and setting all other electrodes to ground. One of these models can be seen in Figure 9. Since SILVACO runs on a 32-bit processor, the main issue encountered when modeling these DSSD designs was memory allocation errors (running out of memory). We elected to employ a finer mesh near the electrodes, where the weighting potential changes the most. As is shown in Figure 10, the weighting potential does not change very rapidly throughout the bulk. Due to this, a coarse mesh was employed throughout the bulk.

From here, a custom MATLAB program was created to calculate the negative gradients of the electric field potential to get the electric potential, which is a scalar quantity. We use this electric potential to calculate/define the amount of energy absorbed

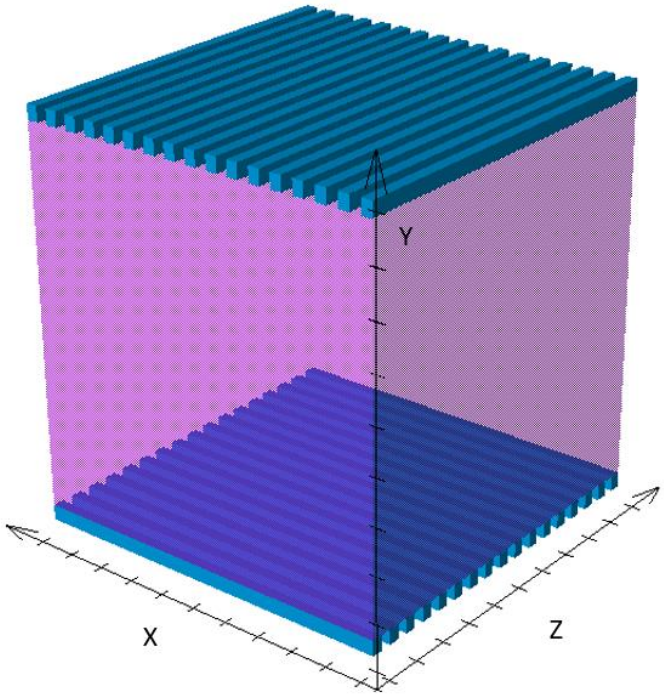

Figure 9. SILVACO design for a DSSD with strip width/pitch of 20/30 µm.

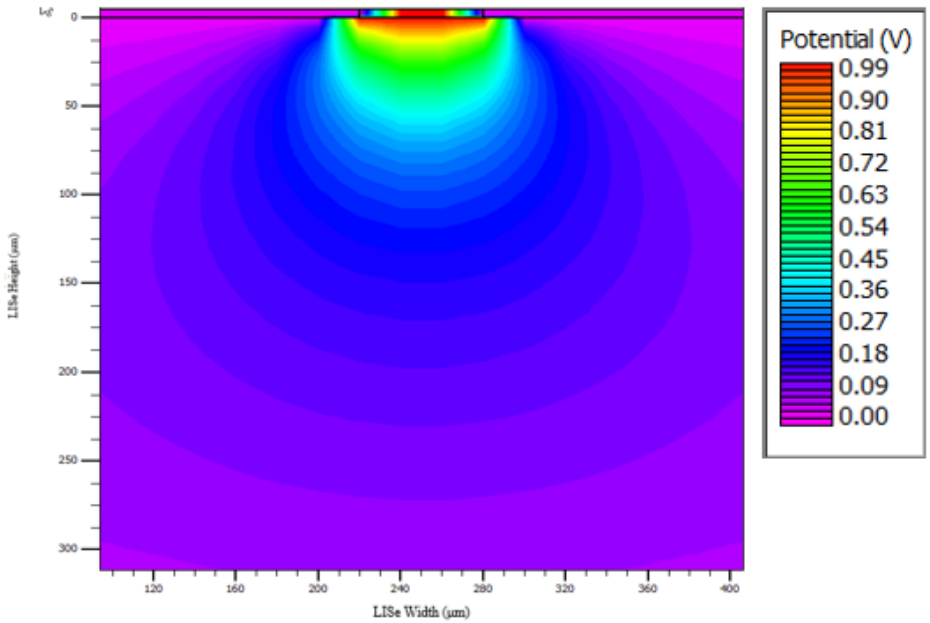

Figure 10. The weighting potential for a central electrode using SILVACO for a strip width/pitch of 40/60 µm.

by a moving charged particle in the electric field. Next, a single point deposition of charge is spawned at one μm points (making up our mesh) within the bulk material, making up our simulation space. This was done to simulate the induced charge on each electrode from a point deposition charge at a given coordinate (X,Y,Z). This was mapped for point depositions of electron-hole pairs across the LISe sensor in a one μm mesh for all (Y) coordinates (bulk), and most (X,Z) coordinates to create our subspace. Lastly, a MATLAB program imports the Bragg Curve data calculated by SRIM to simulate the energy deposited by the secondary particles onto this mapped response. If we sum the induced signal across all strips, with a W-value of 1, we get 4.78 MeV, the Q-value of the Li^6 neutron absorption reaction. The SRIM simulation results can be seen below in Figure 11 and Figure 12.

Since perfect charge collection efficiency (no charge loss) was simulated for this system, a single-point deposition of charge is equal to one. This is also used as a check on the program to ensure the calculations leading up to this point in the code are without error. The simulated charge collected from an electron generated in the middle (250,250,250) of the detector and below Electrode 17 can be seen in Figure 13. In this simulation, Electrodes 3-7 are on the top of the LISe bulk material, and Electrodes 13-17 are on the bottom. As expected, the nearest electrode collects most of the deposited charge (Electrode 5). This simulation was for an electrode width of 20 μm and pitch of 30 μm.

The desired spatial resolution (sub-5 μm) is possible using charge sharing across adjacent strips due to the large range of the triton. To achieve our sub-5 μm spatial resolution goal, we must calculate the induced signal for a mesh throughout the LISe bulk and include a wide range of emission angles for the alpha/triton. We have explored five different strip width/pitch (in μm) combinations to achieve our sub-5 μm spatial resolution detector goal. These DSSD designs include strip widths/pitches of 10/15, 20/30, 30/45, 40/60, and 50/75.

This custom eta-function can be broken down into three main steps, with a flowchart for this code in Figure 14 and the steps on page 43.

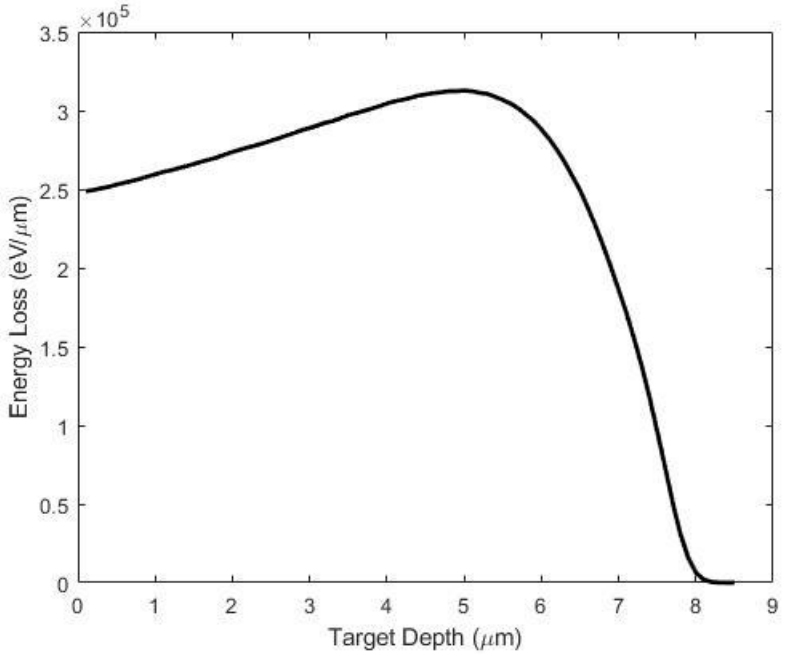

Figure 11. Simulation performed by SRIM to calculate the Bragg Curve data for an alpha particle deposition in LISe [79].

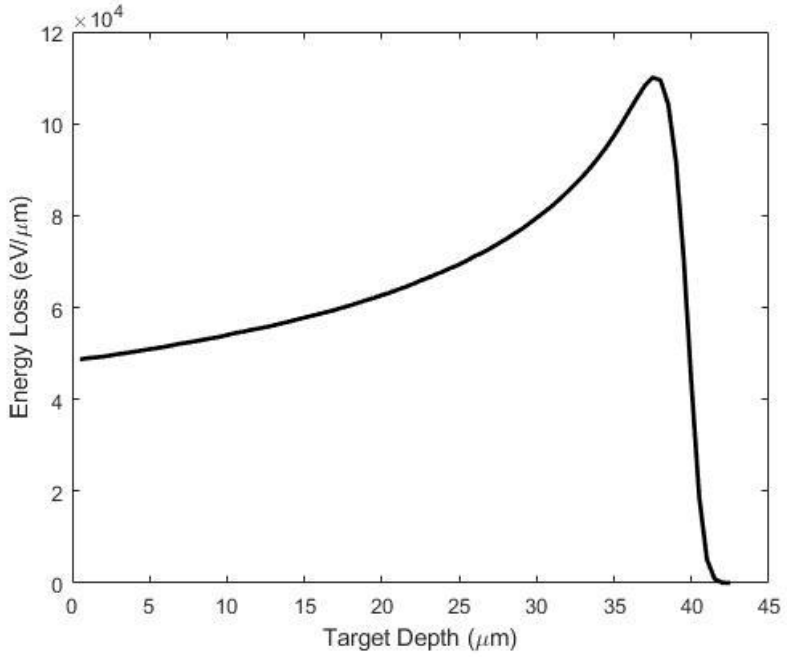

Figure 12. Simulation performed by SRIM to calculate the Bragg Curve data for triton deposition in LISe [79].

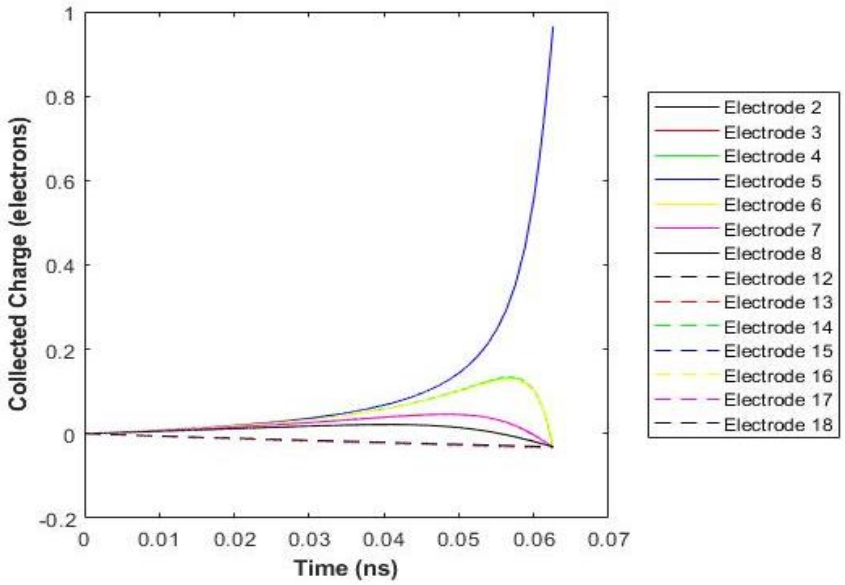

Figure 13. Simulated response of an electron generated at the middle of the detector. This electron is generated under Electrode 5. A charge collection of 1.0 signifies complete charge collection by an electrode.

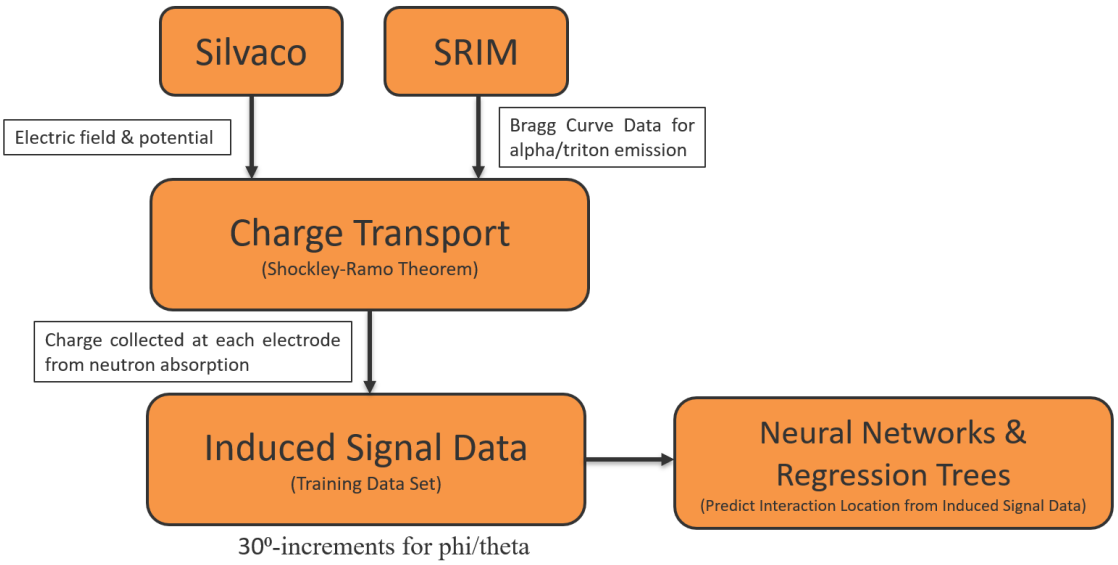

Figure 14. Coding flowchart for the modified η-function that has been developed.

STEP 1

a) Defines DSSD design (strip pitch and width)
b) Imports electric field and weighting potential data generated by SILVACO
c) It uses a scattered interpolation function to go from 10 μm to 1 um mesh
d) Creates gradients of the electric field and outputs them for use in the next step

STEP 2

a) Electron-hole (e-h) pairs are spawned at 1 μm increments within the LISe bulk material. Electrons and holes are tracked throughout the material due to the electric field. The induced charge from each is found based on the gradient of the weighting potential at each time step along their track.
b) These are spawned until they reach the edge of our material based on our DSSD design
c) The output of this code is the (X,Y,Z) coordinate of each e-h pair and the subsequent charge induced on each electrode due to the movement of that pair

STEP 3

a) The results from STEP 2 and the SRIM Bragg Curve data, seen in Figures 11-12, are used to determine the induced charge on each electrode from neutron interactions for all (X,Y,Z) coordinates.
    1. The Bragg Curve data determines the energy deposition of the triton and alpha particle throughout the bulk LISe material at various isotropic emission angles, giving charge generation at specific points.
    2. The responses are given for the top electrodes (electron collectors) and bottom electrodes (hole collectors) of the DSSD. The signal generated from the alpha particle and triton is calculated separately and summed for holes and electrons. The total induced charge on the electrode is the sum of the charge from all freed electrons and holes.

2.2 Training Dataset and Machine Learning Models

The training dataset the machine learning models are trained to consist of the X and Z coordinate and the induced signal on the strip electrodes. Since the alpha/triton are emitted in 4π, we also must simulate the emission angles (φ/θ) emitted antiparallel and include these in the dataset. Performing these simulations for all emissions in 4π is unrealistic, and these simulations take quite some time to run (months without parallelization), so we wanted to figure out the maximum possible emission angle for the simulations to achieve our goal of sub-5 μm spatial resolution. φ ranges from (0°, 360°) and θ ranges from (0°, 180°). To orient φ/θ in this simulation, it is worth noting that φ of 0° is parallel to the X-plane. To achieve our goal of ~ 5 μm spatial resolution, we have trained various machine learning models to predict the neutron interaction location based on the induced signal spread across multiple strip electrodes. Regression Trees and Neural Networks using 20% holdout validation were selected to model this dataset. Holdout validation is commonly employed for datasets where accuracy is essential [105]. The input variables for these models are the induced signal on each electrode for all possible interaction locations (one μm mesh) in our subspace. The output variables for these models are the interaction position (X and Z coordinates) in units of μm. As is typical when employing machine learning models, the model is trained to a single output variable. So, the models for the X and Z coordinates are trained separately. These models predict the neutron absorption location based on the induced signal across multiple strip electrodes. For neural networks, the induced signals are normalized to unit variance. Regression Trees do not require the data to be normalized. All models' minimum/maximum values are included in the training dataset. It is manually added to the dataset if it was not included in part of the 20% holdout validation.

For the neural networks we employed, we used rectified linear unit for the hidden nodes and the Softmax activation for the output node/nodes. The Softmax activation function scales our values into probabilities, as seen in Equation (15). In this equation, σ is the softmax, $\underset{Z}{\rightarrow}$ is the input vector, e^{z_i} is the standard exponential function for the input

vector, K is the number of classes in the multi-class classifier, and e^{z_j} is the standard exponential function for the output vector.

$$\sigma\left(\underset{z}{\rightarrow}\right)_i = \frac{e^{z_i}}{\sum_{j=1}^{K} e^{z_j}} \tag{15}$$

The F1-score is typically used when evaluating the performance of predictive models that provide a binary (yes/no or 1/0) prediction. Since our models predict a non-binary response, we have used the root mean square error (RMSE) to evaluate the model's performance. The standard deviation of the residuals (prediction errors) or RMSE is used to quantify the performance of the various machine learning models. This loss function allows us to compare the performance between varying DSSD designs and is a general-purpose error metric for numerical predictions [106]. The RMSE is often used for predictions in the same way as the standard deviation is used for a typical data set [107]. In Equation (16), N is the sample size, x_i is the predicted value, and $\hat{x}_i$ is the observed value.

$$RMSE = \sqrt{\frac{\sum_{i=1}^{N}(x_i - \hat{x}_i)^2}{N}} \tag{16}$$

We started with 90° emission angles for φ/θ and trained this dataset to coarse regression trees to determine how robust these models were. From here, we tested the model on a dataset consisting of a 1° emission angle for φ/θ to see if the RMSE was under our goal of 5 μm spatial resolution. As expected, the RMSE was greater than 5 μm, so we moved on to a training dataset that consisted of 30° emission angles for φ/θ. As before, this was tested on the same 1° emission angle dataset for φ/θ. The mean RMSE is well below our goal of sub-5 μm spatial resolution. However, bands of high RMSE values could be lowered if finer emission angle was selected for the training dataset. The tradeoff with

setting smaller/finer emission angles for φ/θ is the computational time since the emission angles will make the nested for-loops larger; because of this, the time required to run the simulations increases exponentially.

We also wanted to ensure that the trained models still perform correctly under a few regions of interest. These being mainly at the edge of our subspace, between two strips, directly under a strip, and at the edge of a strip electrode. We also wanted to determine if the interaction depth affected our model performance. Figure 15 provides a visual representation of these regions of interest. Once the areas of interest were selected, we tested the performance of our coarse trees and neural networks at these points. The coarse trees and neural networks had very similar performance, so Table 1 only contains the RMSE results for the coarse trees. As one can see from the italicized values in the table, the model has the highest RMSE (worst performance) near the edges.

A model for an electrode strip/pitch of 10/15 μm with a 1 μm mesh and 30º emission angles for the secondary charged particles was trained to Coarse Regression Trees (minimum leaf size: 36). A simulation was performed for an interaction location in the middle of the device with 1º emission angles for the secondary charged particles to prove that simulating 30º emission angles was sufficient for our goal. The RMSE versus Phi and Theta for various regions of interest can be seen in Figures 16-19. The RMSE values for these for these simulations can be found in Table 2-3. Another explored region of interest was at the edge of our subspace and the middle of our detector. As one can see from these results, the RMSE approaches the strip pitch (30 μm) at φ of 90º and θ of 90º and 270º. So, if the charge is directed upwards or downwards and not shared across adjacent strips, we see a decreased model performance. If finer emission angles for φ/θ are used when the charge is only spread across a single strip (directly upwards or downwards) then the model performance (RMSE) will increase. There is a trade-off between computational time and model fidelity, but based upon these results, 30º emission angles for φ/θ is sufficient to achieve our goal of sub-5 μm spatial resolution.

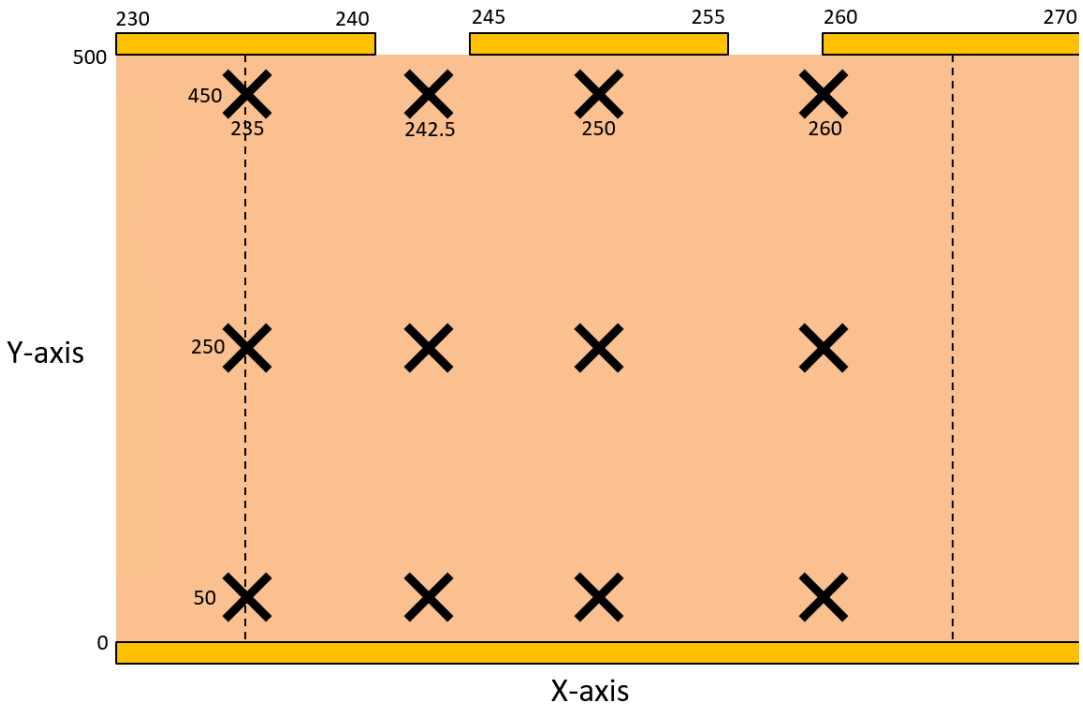

Figure 15. Schematic that identifies regions of interest for a strip pitch of 15 µm and strip width of 10 µm DSSD design. Regions of interest are designated by a black X. The training dataset subspace ranges from the dashed line on the left to the dashed line on the right.

Table 1. RMSE Dependence on Phi and Theta for a Reconstruction at the center of a 10/15 DSSD design

Phi (0º-180º)	Theta (0º-360º)	Mean RMSE (μm)
0	0-10	8.11
0	40-50	9.06
0	85-95	8.40
0	350-360	6.82
45	0-10	11.30
45	40-50	6.12
45	85-95	5.38
180	0-10	8.12
180	40-50	9.05
180	85-95	8.37
180	265-275	8.38

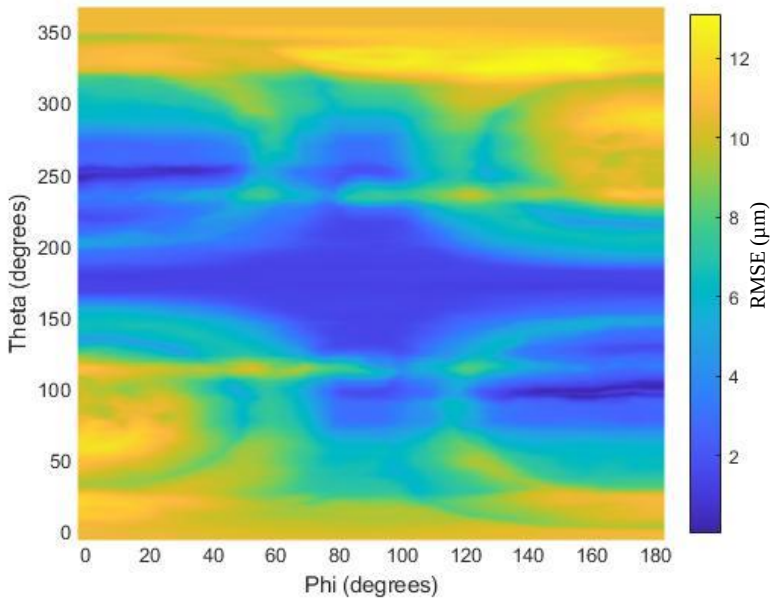

Figure 16. Coarse Regression Tree model performance (RMSE in μm) versus angular position (φ/θ). This is for a neutron interaction at the edge of our subspace and the middle of the device (235,250,235). This is tested on 1º emission angles for the secondary charge particles.

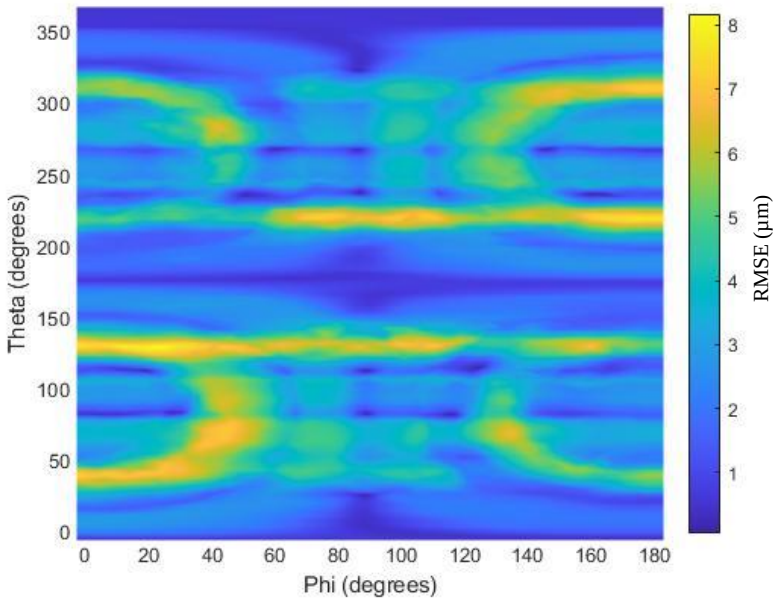

Figure 17. Coarse Regression Tree model performance (RMSE in μm) versus angular position (φ/θ). This is for a neutron interaction between two adjacent strips and the middle of the device (242.5,250,242.5). This is tested on 1º emission angles for the secondary charge particles.

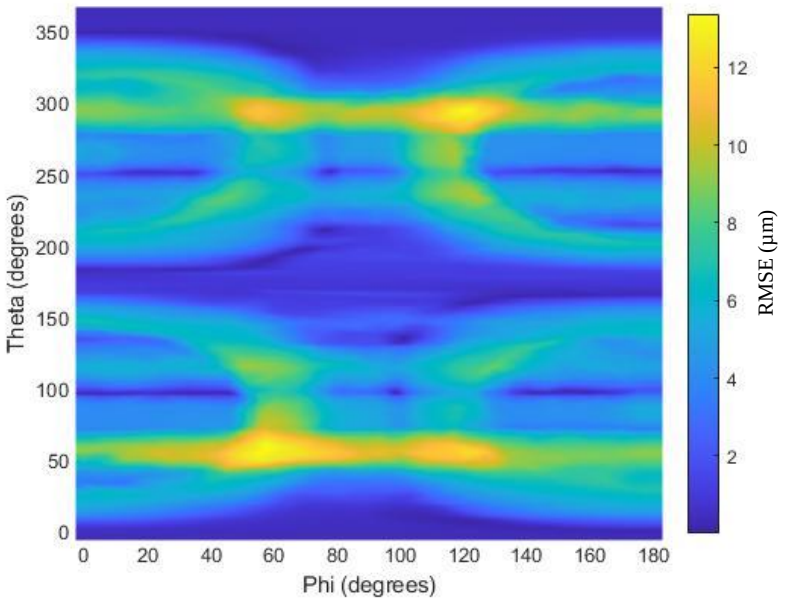

Figure 18. Coarse Regression Tree model performance (RMSE in µm) versus angular position (φ/θ). This is for a neutron interaction in the middle of the device (250,250,250) with 1º emission angles for the secondary charged particles.

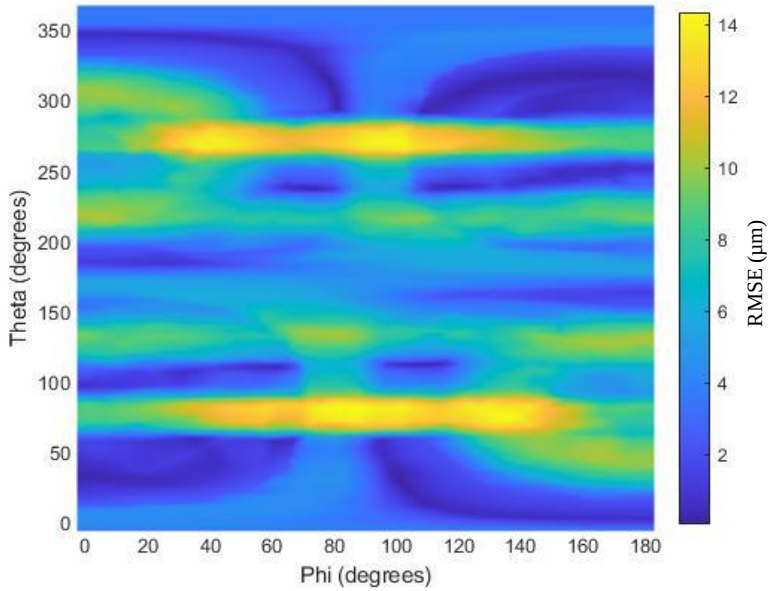

Figure 19. Coarse Regression Tree model performance (RMSE in μm) versus angular position (φ/θ). This is for a neutron interaction at the edge of the rightmost strip in our subspace and in the middle of the device (260,250,260) with 1º emission angles for the secondary charged particles.

Table 2. Coarse Regression Tree RMSE for varying positions (Y)

Coarse Tree		
Interaction Location	Mean RMSE (μm)	Median RMSE (μm)
(235,50,235)	7.19	2.01
(235,250,235)	7.26	2.01
(235,450,235)	7.26	2.01
(242.5,50,235)	2.45	1.13
(242.5,250,235)	2.52	1.52
(242.5,450,235)	2.52	1.52
(250,50,235)	2.01	1.41
(250,250,235)	2.10	1.43
(250,450,235)	2.12	1.57
(260,50,235)	2.50	2.00
(260,250,235)	2.56	2.00
(260,450,235)	2.58	2.00

Table 3. Coarse Regression Tree RMSE for varying positions (X,Y,Z)

Coarse Tree		
Interaction Location	Mean RMSE (μm)	Median RMSE (μm)
(235,250,242.5)	*6.44*	0.50
(242.5,250,242.5)	1.39	0.71
(250,250,242.5)	0.85	0.50
(260,250,242.5)	1.58	0.50
(235,250,250)	*7.32*	2.85
(242.5,250,250)	2.66	2.03
(250,250,250)	2.08	1.83
(260,250,250)	2.59	2.26
(235,250,260)	*6.41*	1.00
(242.5,250,260)	1.45	0.50
(250,250,260)	0.86	1.00
(260,250,260)	1.55	1.00

2.3 Image Reconstruction

Once the models had been trained, we were ready to test them with simulated (MCNP6.2) data. This η-function calculates the induced signal for a neutron interaction at the given MCNP6.2 simulated absorptions. Based on the previous section's results, the model were trained on a one μm gridded mesh (to the left/right of an electrode in the middle) with 30º emission angles for φ/θ. These reconstructions aimed to test our model against the MCNP6.2 data.

We used MCNP6.2 to simulate a neutron beam striking a University of Tennessee Power T in front of a LISe imager. Due to its high thermal neutron absorption cross-section, ^{157}Gd was used as the material for the object of interest. We then sorted through the Particle Track Output (PTRAC) PTRAC F8 tally and found all the ^{6}Li neutron absorption locations within LISe. These locations were used as the interaction location for the η-function, and a random emission angle was chosen for φ and θ. After running it through our η-function, we get the induced signal data from a neutron absorption at (X,Y,Z) coordinates (provided by MCNP6.2) for a 500 μm thick LISe detector. This was performed for any DSSD designs that we wanted to test.

To reconstruct images larger than the simulation subspace (2 × strip pitch), the PTRAC neutron absorption data was divided into even voxels that are equal to the dimensions of the simulated subspace and ran through the η-function. Correctly grouping and naming this data was important to have accurate reconstructions. The MCNP6.2 PTRAC raw data for the first University of Tennessee Power T can be seen in Figure 20 and divided up into small voxels to be run through the η-function in Figure 21. The coarse tree reconstruction for this can be seen in Figure 22 and was the first proof-of-concept for our modified η-function coupled with machine learning models. For all of these image reconstructions, properly binning data for pixels is very important to prevent striations or artifacts in images. After seeing these results, we decided to simulate a knife-edge test using MCNP6.2. This consisted of a neutron beam (1E9 neutrons) striking a Gadolinumium-157 knife-edge with our 500 μm thick LISe detector behind it. The PTRAC data was fed to the η-function like it was for the Power T reconstruction. The PTRAC data

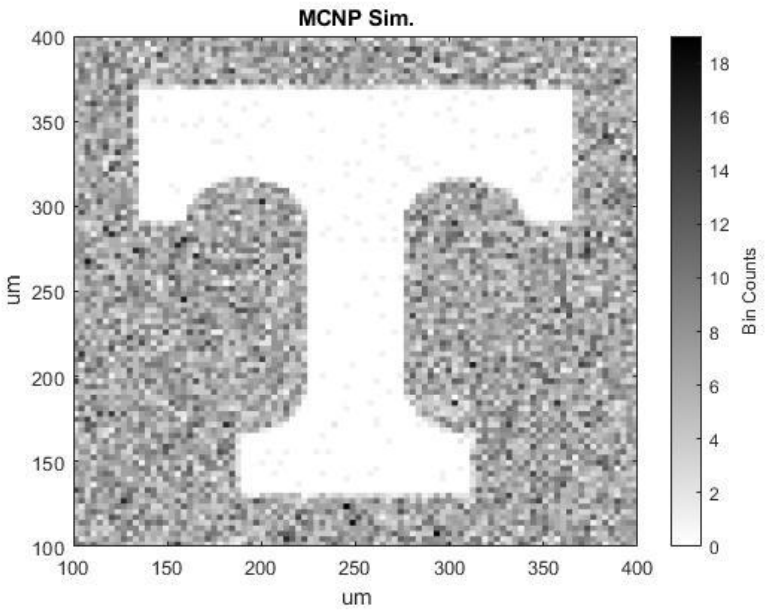

Figure 20. MCNP6.2 simulation of the University of Tennessee Power T. Neutron absorptions are binned into 4 μm pixels.

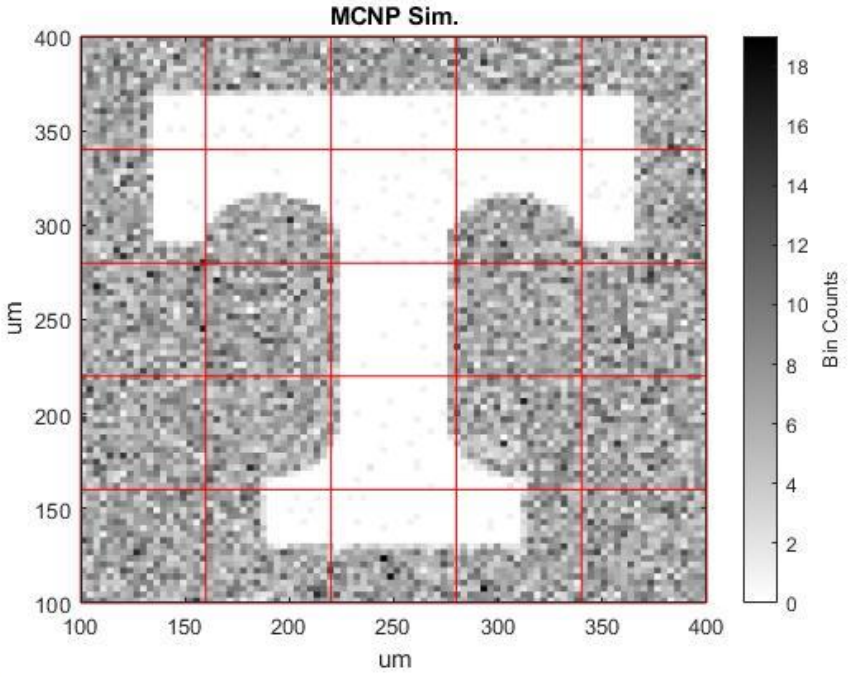

Figure 21. The raw data from was divided into 5×5 60 μm squares (for a design that has a strip width/pitch of 20/30 μm) which were then run through the custom MATLAB code to generate the induced signal from a neutron absorption at each interaction location. MCNP PTRAC ^{6}Li neutron absorptions were used as the initial interaction location (generation point) in our eta-function.

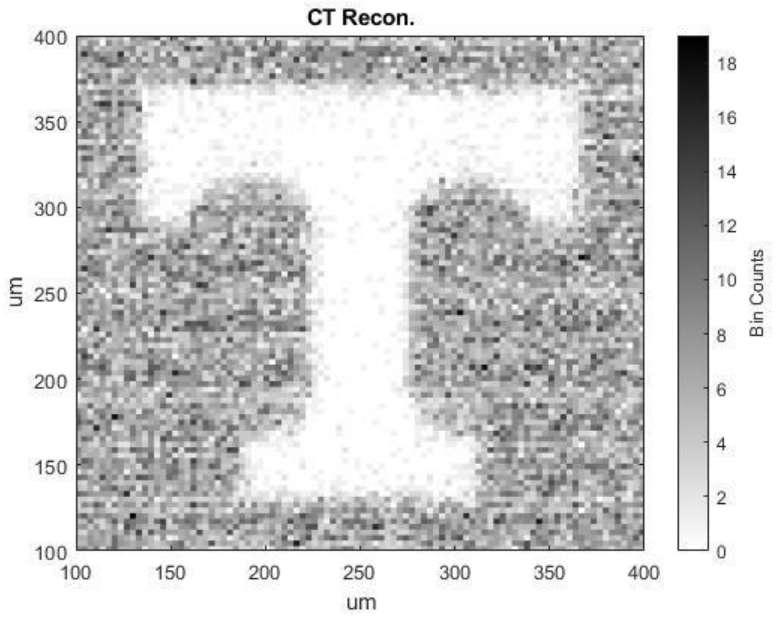

Figure 22. Coarse Tree reconstruction of the University of Tennessee Power T. Neutron absorptions are binned into 4 μm pixels. The simulated DSSD has a strip width/pitch of 20/30 μm.

can be seen in Figure 23, and the Coarse Tree reconstruction can be seen in Figure 24. The Coarse Regression Trees are able reconstruct the knife-edge; however, the edge does appear to be blurred. We wanted to find the 10% MTF to determine the absolute spatial resolution of our detector. Unfortunately, we did not have high enough bin counts on the edge to get any reliable results. Increasing the number of neutrons in the MCNP6.2 simulation would allow us to achieve reliable results and will likely be performed in the future. Ten reconstructions were performed for this knife-edge data with no fluctuations in the RMSE values for the predictions, showing that the reconstructions are reproducible and have minimal fluctuations.

From here, we simulated a smaller (10 μm) University of Tennessee Power T to test the performance of the five DSSD strip width/pitch variation. The results from this reconstruction can be seen in Figure 25 and a summary of the RMSE values can be found in Table 4. RMSE values for reconstructions of the University of Power T using different DSSD Designs. Note that in Figure 25, only four of the reconstructions are shown. Neural networks and coarse regression trees were trained to the same simulated datasets and have very different RMSE values. Coarse regression trees are the most accurate models and have RMSE values between 3-7 meanwhile, neutron networks have RMSE values between 11-24 for the same reconstruction. Considering these models are trained on simulated data (one μm mesh, perfect CCE, and 30º emission angles for φ/θ) coarse regression trees are a viable option for us to reach our goal of sub-5 μm spatial resolution. In the coming sections we will discuss the addition of noise and varying CCE on the performance of these models.

2.4 Addition of Noise

Since we have simulated LISe as an ideal semiconductor, we need to add noise to the dataset to ensure our models still perform properly under realistic/operating conditions. This is important to evaluate the effect of noise on the η-function performance. Noise is generally divided into two main categories, statistical and electronic noise. In its simplest form, statistical noise is defined as the unexplained variance in a dataset. Likewise, electronic noise refers to the unwanted electrical energy that degrades the quality of the

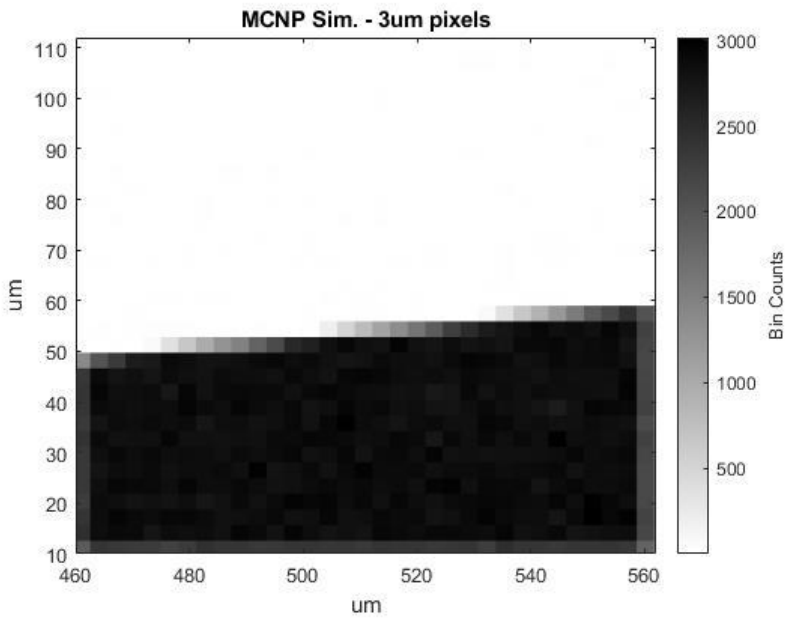

Figure 23. MCNP6.2 simulation of a Gd-157 knife-edge. Neutron absorptions are binned into 3 μm pixels.

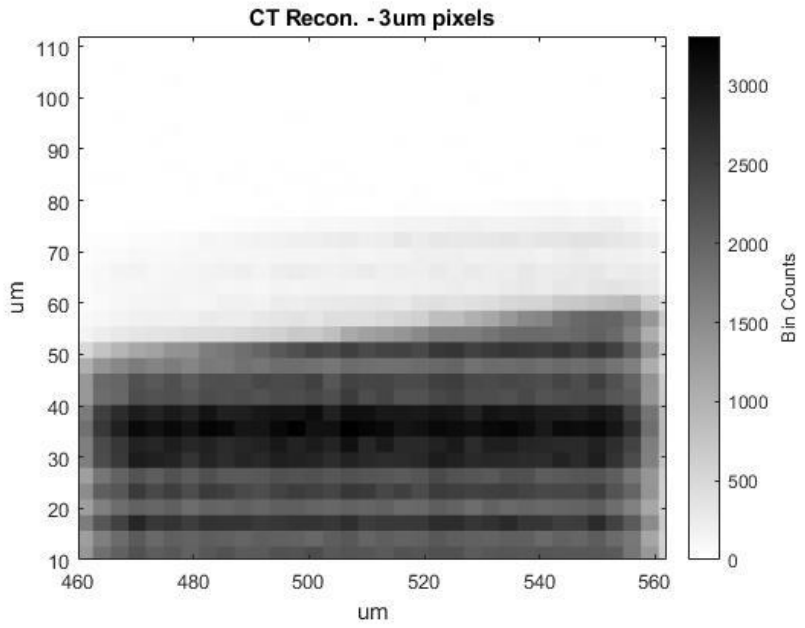

Figure 24. Coarse Tree reconstruction of a Gd-157 knife-edge. Neutron absorptions are binned into 3 μm pixels. The simulated DSSD has a strip width/pitch of 20/30 μm.

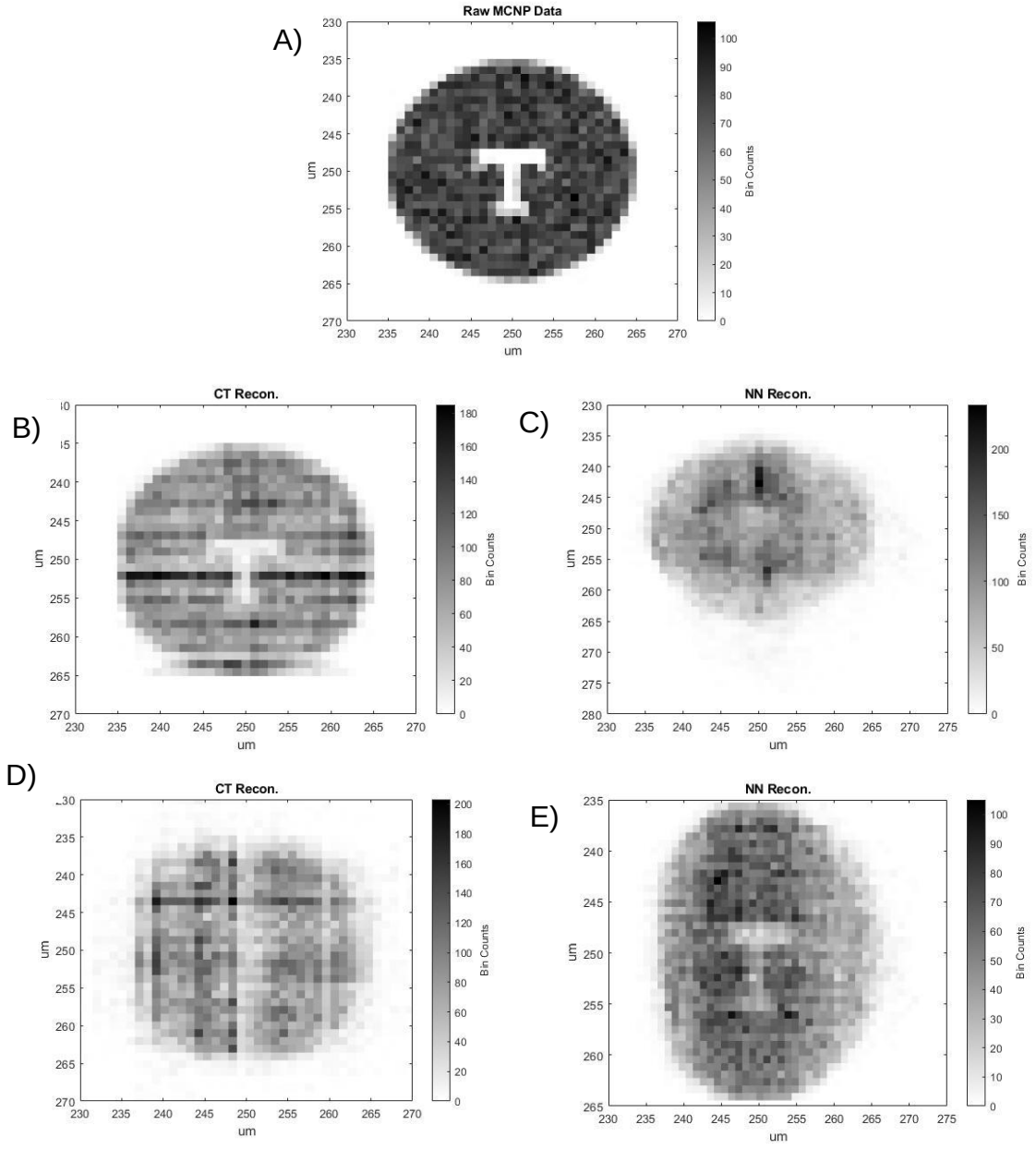

Figure 25. Reconstruction of the University of Tennessee Power T. Neutron absorptions are binned into 1 μm pixels. A) Raw MCNP Data. B) Strip width/pitch of 10/15 μm Coarse Tree Reconstruction. C) Strip width/pitch of 10/15 μm Neural Network Reconstruction. D) Strip width/pitch of 30/45 Coarse Tree Reconstruction. E) Strip width/pitch of 30/45 Neutral Network Reconstruction.

Table 4. RMSE values for reconstructions of the University of Power T using different DSSD Designs

DSSD Design Strip Width/Pitch	Coarse Tree RMSE (μm)	Neural Network RMSE (μm)
10/15	1.76	4.00
20/30	2.41	3.77
30/45	5.03	3.43
40/60	5.59	4.45
50/75	6.81	24.55

signals we receive. We elected to add 100, 500, and 1,000 e^- of Gaussian noise to the University of Tennessee Power T datasets that is shown in Figure 25. A visual representation of adding 100 e^- of gaussian noise to a dataset can be seen in Figure 26, where sigma is equal to 100 e^-. The RMSE from these reconstructions can be seen in Table 5: RMSE values for Power T reconstruction using four different DSSD designs and the addition of gaussian noise to the dataset and show where the models start to perform poorly. Please note that when the RMSE approaches 5 μm we cannot correctly reconstruct the fine features of the Power T.

Based upon the results in Table 5., the addition of Gaussian noise to the datasets before reconstruction has little effect on the ability of the model to reconstruct fine features properly. Due to this, we wanted to determine how far we could push our reconstruction models. For this reason, we added up to 10,000 e^- of Gaussian noise to our datasets and tested their performance. This was done to determine exactly where the models would break down. The strip width/pitch design of 10/15 was selected for these tests. The edge of the subspace (235,250,235) was selected as the dataset to add noise to, because it has the highest RMSE value from the results shown in Table 3. These results can be seen in Tables 6-7. From these results, the neural networks start predicting outside the subspace after 3,000 e^- of Gaussian noise is added to the datasets. The coarse tree models do not predict outside the subspace and has very little error even after adding 10,000 e^- of Gaussian noise.

2.5 Charge Collection Efficiency

Charge collection efficiency, commonly called CCE, is the amount of charge collected from the detector for a single radiation event. If all generated electron-hole pairs are also collected, the CCE would be equal to one. The deviations from perfect CCE typically come from trapping and defects in the crystal lattice. For the first iteration of the η-function, an ideal semiconductor was simulated with no charge carrier detrapping, no charge carrier loss, and perfect CCE. However, in the real world, no semiconductor is perfect. Due to this, we wanted to make our simulations more realistic by running models

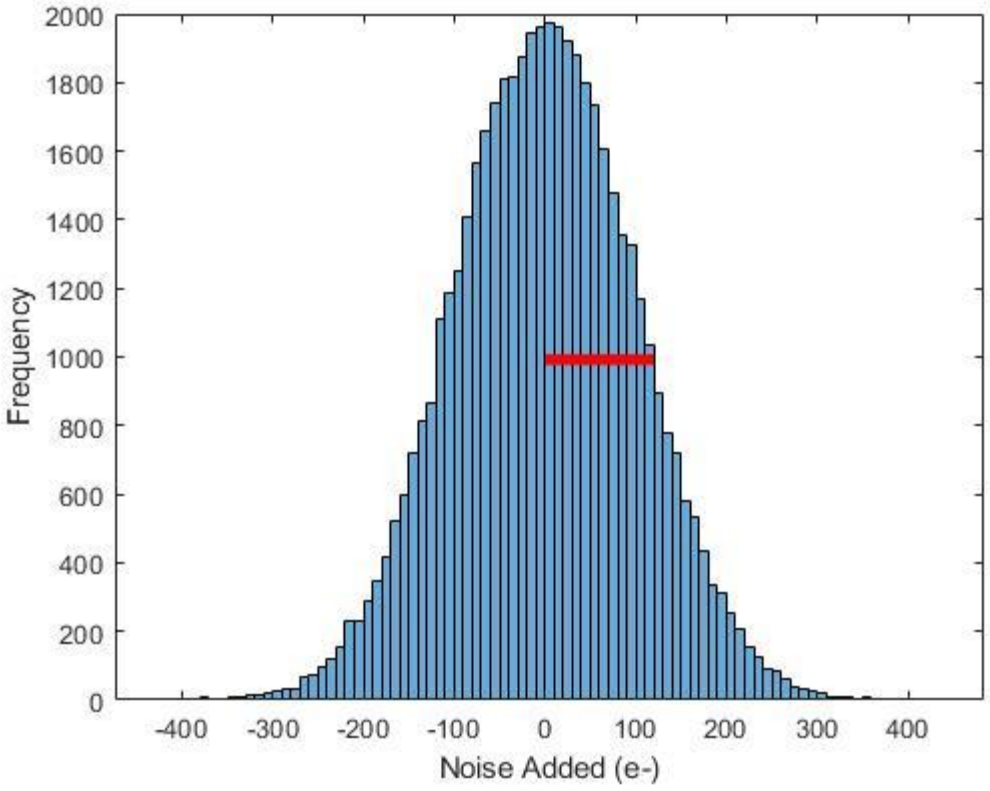

Figure 26. Gaussian noise was added to the final generated datasets to test how to models would perform in the real world with the addition of noise. Sigma is denoted by the red line in this plot and is equal to 100 e^-.

Table 5: RMSE values for Power T reconstruction using four different DSSD designs and the addition of gaussian noise to the dataset

DSSD Design	Gaussian Noise	RMSE (μm)	
Strip width/pitch	e^-	Neural Networks	Coarse Tree
10-15	0	4.00	1.76
10-15	100	4.01	1.79
10-15	500	4.30	1.96
10-15	1,000	5.10	2.20
20-30	0	3.77	2.41
20-30	100	3.78	2.43
20-30	500	3.94	3.05
20-30	1,000	4.41	4.12
30-45	0	3.43	5.03
30-45	100	3.63	5.13
30-45	500	4.46	6.52
30-45	1,000	5.79	8.61
40-60	0	4.45	5.59
40-60	100	4.48	5.67
40-60	500	5.10	7.06
40-60	1,000	6.26	9.39

Table 6. Coarse Regression Tree RMSE with the addition of noise

Coarse Tree - (235,250,235)		
Noise (e^-)	Mean RMSE (μm)	Median RMSE (μm)
0	2.51	1.52
10	2.51	1.52
100	2.50	1.57
1,000	2.53	1.88
2,000	2.70	2.00
3,000	2.86	2.19
4,000	2.98	2.25
5,000	3.06	2.31
10,000	3.26	2.57

Table 7. Neural Network RMSE with the addition of noise

Neural Network - (235,250,235)		
Noise (e^-)	Mean RMSE (μm)	Median RMSE (μm)
0	6.47	6.51
10	6.47	6.51
100	6.47	6.51
1,000	6.55	6.57
2,000	6.76	6.78
3,000	7.13	7.06
4,000	7.63	7.42
5,000	8.18	7.77
10,000	11.66	9.29

for a CCE of 0.10, 0.25, 0.5, 0.75, and 0.9. The models that are trained on perfect charge collection efficiency and are tested against these varying CCE simulations. This is due to ensure that we have plenty of realistic datasets and models for our η-function. Since the Power T reconstruction was used to test the addition of noise to the dataset and resulting model performance, the PSI Siemens Star reconstruction was used to test the varying CCE datasets against the models trained for perfect charge collection efficiency. The innermost spokes of the PSI Siemens Star were used to test the model performance, with the raw MCNP PTRAC output data shown in Figures 27-29. Figure 30 shows how the data is divided up in order to simulated the subspace for the width/pitch design of 10/15 μm. The coarse tree and neural network reconstructions for this design can be seen in Figure 31-32. In similar fashion, Figure 33 shows how the data is divided for the simulated subspace of a width/pitch of 50/75 μm and the results from the reconstruction can be seen in Figures 34-35.

From these results in Table 8, the strip width/pitch design of 10/15 shows the lowest RMSE while varying the CCE, but for perfect CCE, the 20/30 design has the lowest RMSE. All models have the worst performance when the CCE is equal to 0.1. This shows us that when working with a material that has a low CCE, the models will likely need to be trained to a simulated dataset with that corresponding CCE. As expected, all models show the best performance on datasets they were trained on, a CCE of 1. When looking at the Neural Network performance, setting the CCE equal to between 0.25 and 0.75 results in the best model performance (lowest RMSE). This was expected because Neural Networks are highly robust to variations or changes in the datasets. For coarse tree models, the 10/15 design shows the best performance, and the 20/30 design has the best performance for neural networks. Considering everything, it is best to test the CCE for any semiconductor and incorporate that value into the simulations. This will lead to higher fidelity models and allow us to reach our sub-5 μm spatial resolution goal. The only models that meet this goal for perfect CCE are the 10/15 and 20/30 DSSD designs.

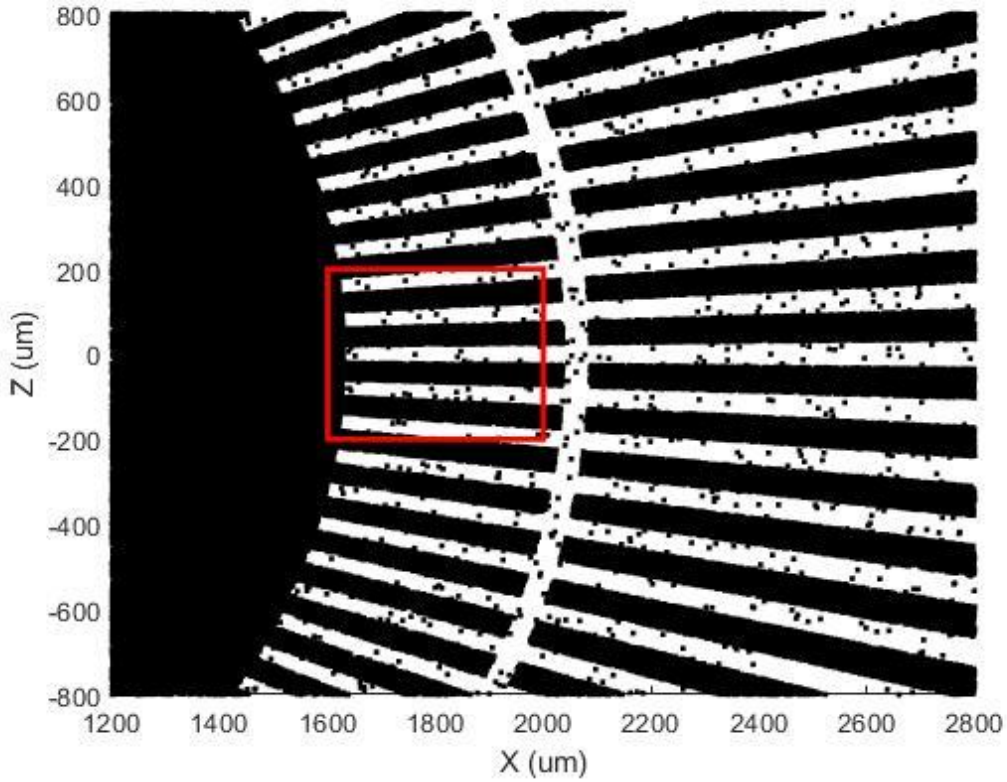

Figure 27. PSI Siemens Star test object simulated by MCNP6.2. The red box is the region that we reconstructed using our five different DSSD designs.

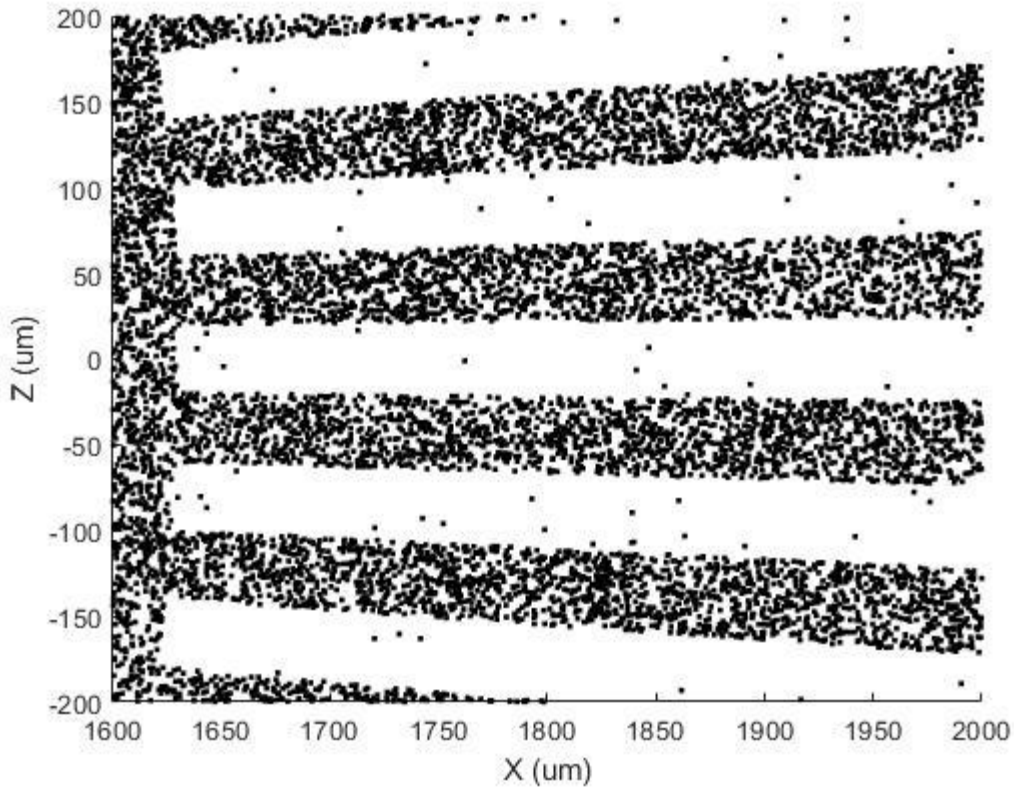

Figure 28. Zoomed-in region of the PTRAC output PSI Siemens Star that was used to test the performance of our various DSSD designs and models.

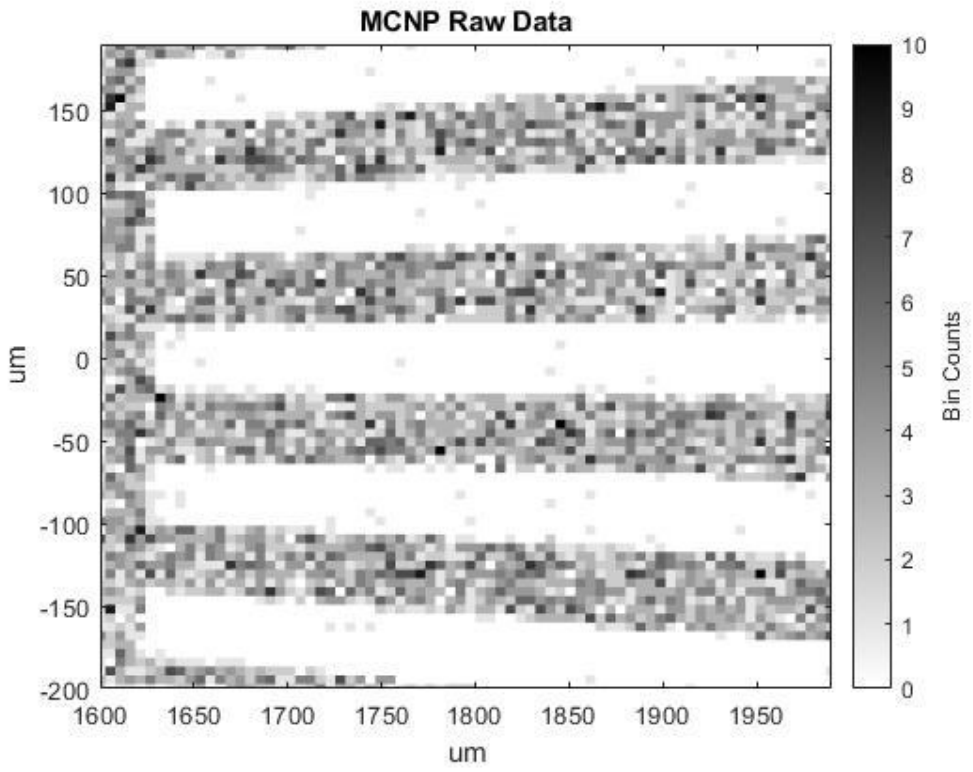

Figure 29. The raw MCNP6.2 data shown in Figure 29 is binned into 5 μm pixels.

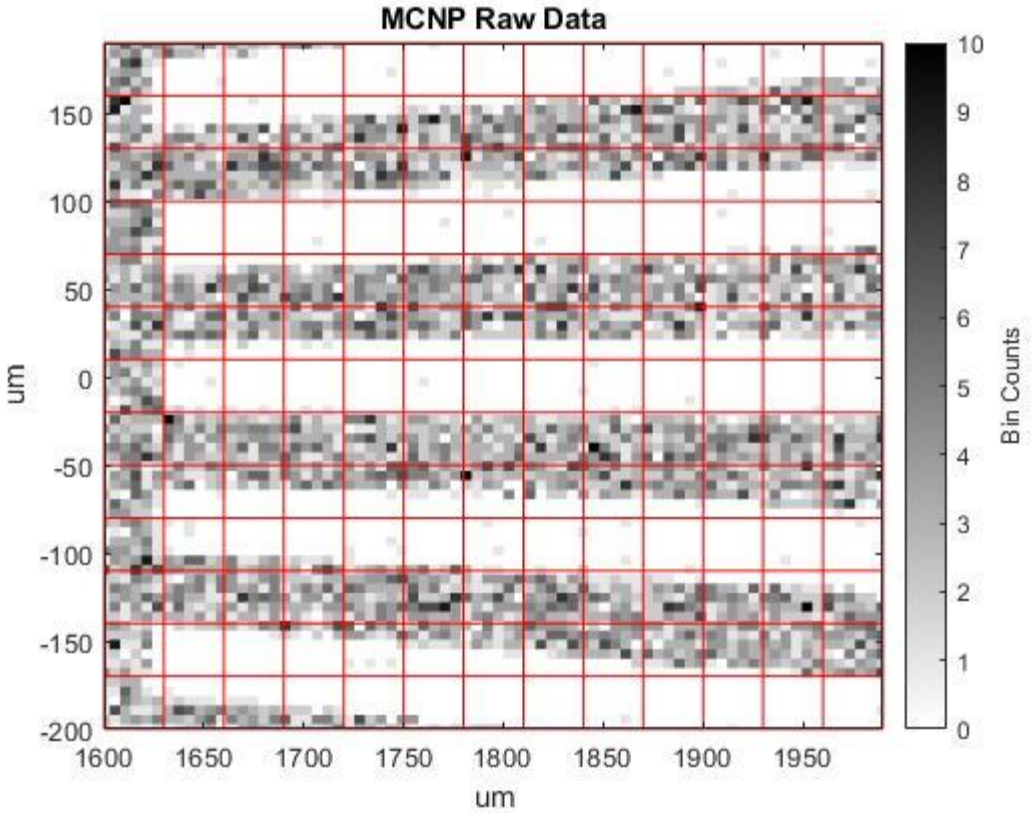

Figure 30. The raw data from Figure 28 was divided into 13×13 30 μm squares (width/pitch of 10/15) which were then run through the custom MATLAB code to generate the induced signal from a neutron absorption at each interaction location. MCNP ptrac Li-6 neutron absorptions were used as the initial interaction location (generation point) in these simulations.

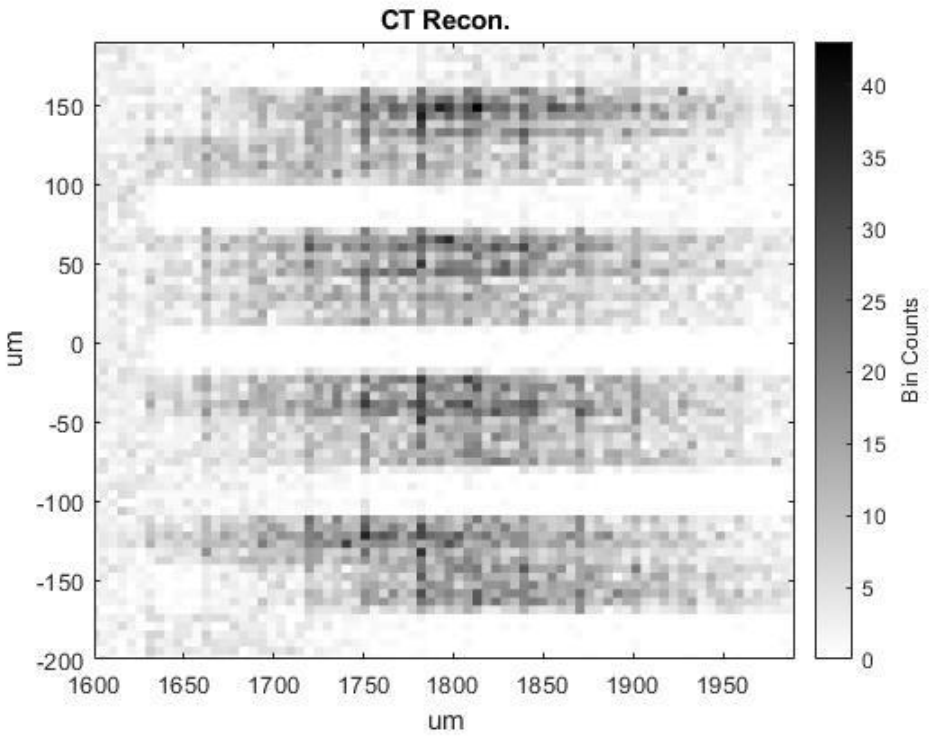

Figure 31. Coarse Tree reconstruction of the 10/15 strip width/pitch design for the PSI Siemens Star. No noise is added to this reconstruction, and data is binned into 5 µm pixels.

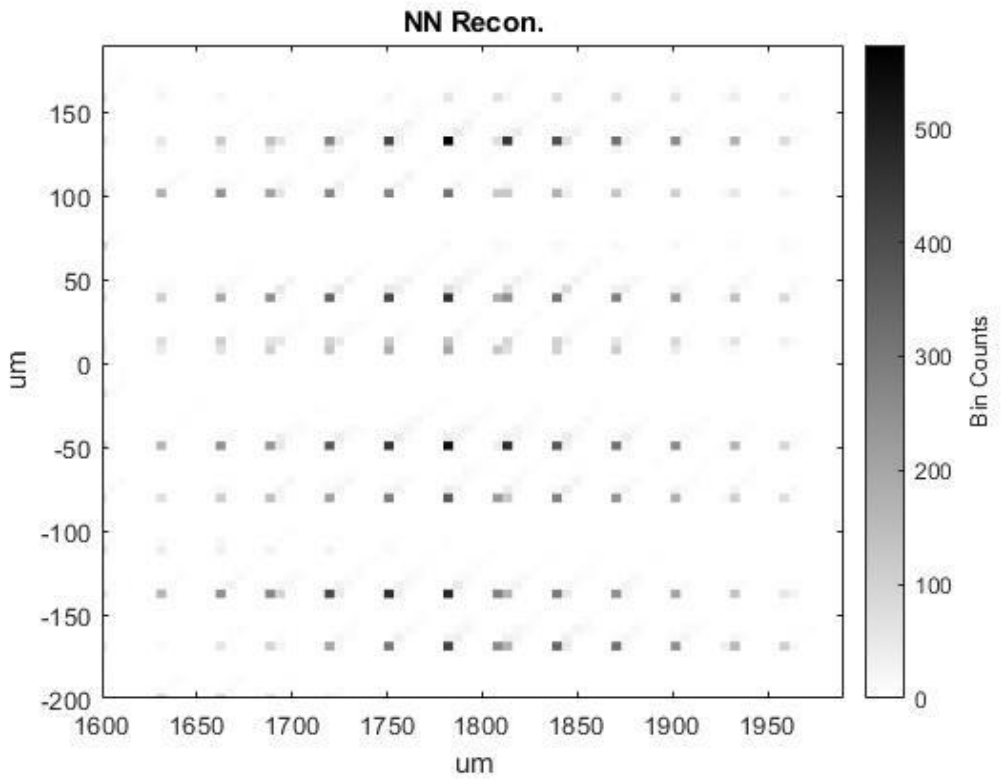

Figure 32. Neural Network reconstruction of the 10/15 strip width/pitch design for the PSI Siemens Star. No noise is added to this reconstruction, and data is binned into 5 µm pixels.

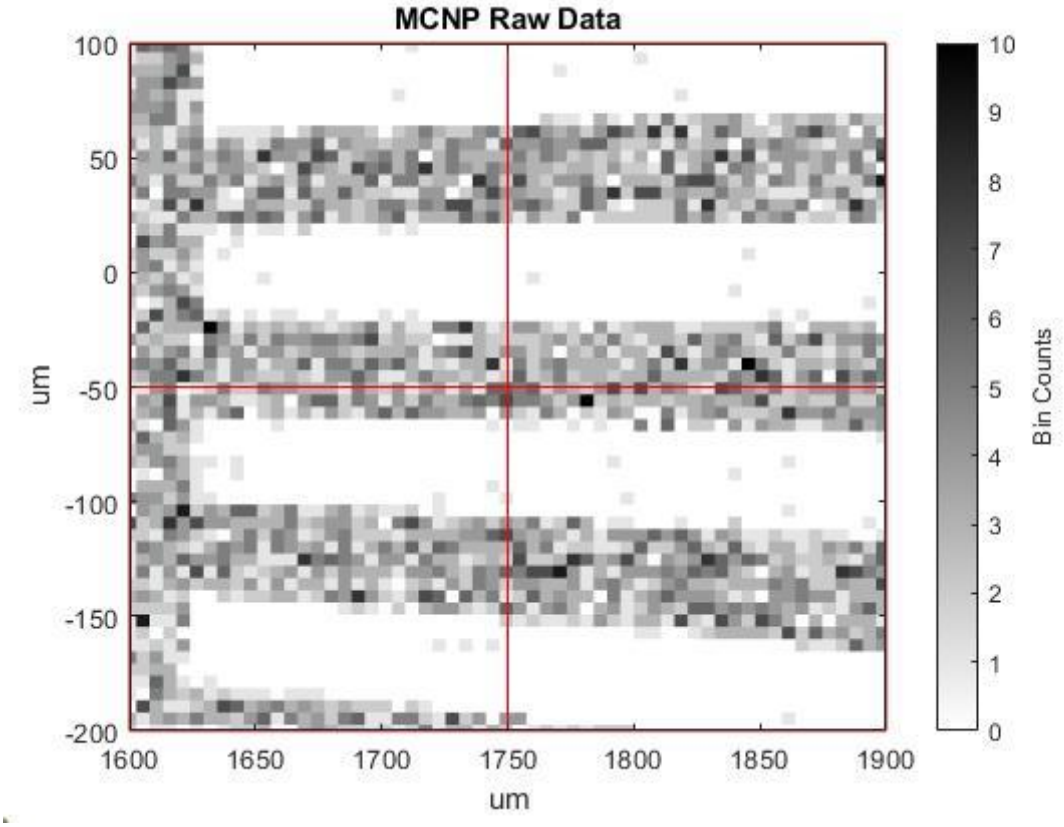

Figure 33. The raw data from Figure 28 was divided into 2×2 150 μm squares which were then run through the custom MATLAB code to generate the induced signal from a neutron absorption at each interaction location for a 50/75 strip width/pitch. MCNP ptrac Li-6 neutron absorptions were used as the initial interaction location (generation point) in our simulations.

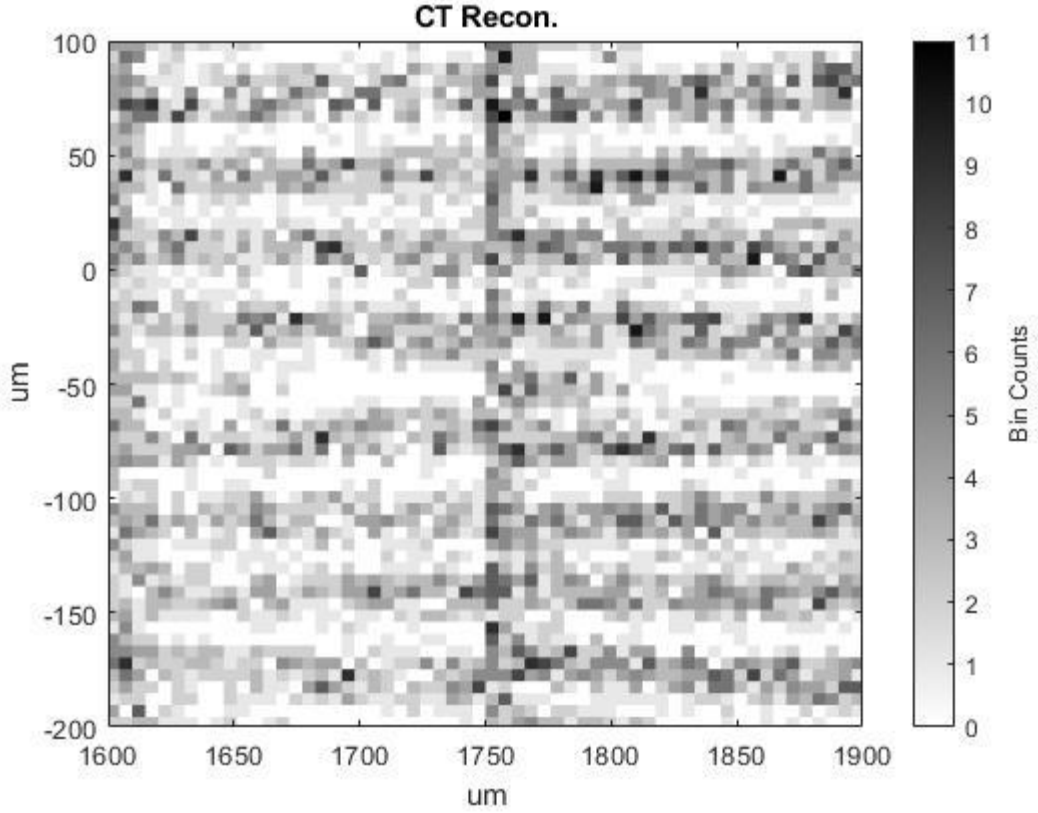

Figure 34. Coarse Tree reconstruction of the 50/75 strip width/pitch design for the PSI Siemens Star. No noise is added to this reconstruction, and data is binned into 5 μm pixels.

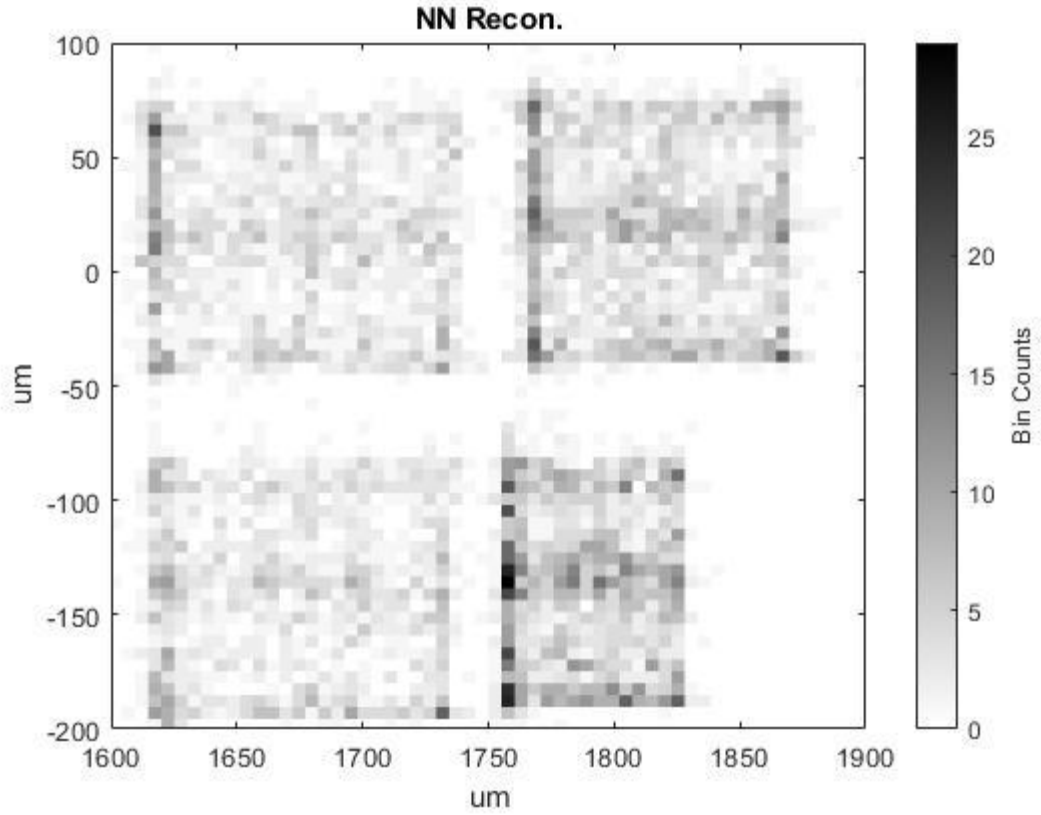

Figure 35. Neural Network reconstruction of the 50/75 strip width/pitch design for the PSI Siemens Star. No noise is added to this reconstruction, and data is binned into 5 μm pixels.

Table 8: RMSE values for PSI Siemens Star reconstruction using five different DSSD designs while varying CCE

DSSD Design		RMSE (μm)	
Strip width-pitch	CCE	Coarse Tree	Neural Networks
10-15	0.10	13.68	18.31
10-15	0.25	10.49	18.73
10-15	0.50	7.88	18.89
10-15	0.75	5.83	19.75
10-15	0.90	4.45	20.94
10-15	1	4.09	22.23
20-30	0.10	33.10	19.01
20-30	0.25	11.80	13.94
20-30	0.50	15.21	11.76
20-30	0.75	13.58	11.47
20-30	0.90	11.31	11.78
20-30	1	3.46	11.72
30-45	0.10	37.99	22.62
30-45	0.25	22.34	20.04
30-45	0.50	13.21	12.81
30-45	0.75	12.54	14.18
30-45	0.90	12.68	16.10

Table 8 continued: RMSE values for PSI Siemens Star reconstruction using five different DSSD designs while varying CCE

DSSD Design		RMSE (μm)	
Strip width-pitch	CCE	Coarse Tree	Neural Networks
30-45	1	5.89	17.65
40-60	0.10	43.23	31.45
40-60	0.25	25.84	28.96
40-60	0.50	15.64	14.25
40-60	0.75	13.90	13.46
40-60	0.90	13.58	14.12
40-60	1	6.12	15.66
50-75	0.10	51.51	46.91
50-75	0.25	30.21	37.05
50-75	0.50	15.77	26.55
50-75	0.75	15.15	25.98
50-75	0.90	15.07	24.98
50-75	1	6.81	24.55

2.6 Determining the Optimal Strip Width/Pitch

Since metalizing and testing many different DSSD designs experimentally is cost-prohibitive, we have determined computationally that several models with possible strip width/pitches meet our goal of sub-5 μm spatial resolution. As stated previously, the RMSE is used to compare the performance between different models. Gaussian noise and varying CCE values were added to all models, with the performance of these models being discussed in the previous sections. Suppose the performance of any two models is the same. In that case, the largest strip width/pitch will be selected, making designing the electronics slightly less challenging and allowing us to create a larger area device, assuming we are developing a fixed number of readout channels.

After adding Gaussian noise to the simulated datasets and calculating the RMSE, three possible strip width/pitches meet our sub-5 μm spatial resolution goal. These are the 10/15, 20/30, and 30/45 μm designs. Only two strip width/pitch combinations meet our spatial resolution goal after adding in CCE, the 10/15 and 20/30 designs. After comparing these results, we narrowed it down to the 10/15 or 20/30 design. Since these two models have a very similar RMSE, the 20/30 design has been selected as the optimal strip width/pitch to build a detector.

It is worth noting again that this η-function is applicable for any ^{6}Li-based direct conversion semiconductor. We have determined computationally which possible strip width/pitch combination offers us the best chance to meet our sub-5 μm spatial resolution goal. To compare the performance between different models, we used the RMSE and have shown that the 10/15 and 20/30 designs will meet our goal. It is worth noting that a fairly wide range of strip pitches/widths will meet our goal. We have shown that varying the CCE plays a much larger role in model performance over Gaussian noise for these cases. Since two DSSD configurations provide similar spatial resolution results, it is ideal to go with the larger strip width/pitches of the two designs.

2.7 Development of a LISe Detector

As a risk mitigation strategy, we elected to bond a LISe wafer to a Timepix ASIC to have a working detector. This section will address building this sensor and the challenges associated with this system. A raw LISe wafer was polished using a polishing machine, with the final polish being 0.1 μm, which was done to prevent sample wedging. After interferometer measurements were taken to ensure the sample had sub-5 μm wedging, it was chemically etched with a bromine/methanol solution such that it had an optical finish and was perfectly smooth. An image of the interferometer results for the Y-Profile of a polished sample can be seen in Figure 36, and a photo of the LISe sample before being etched can be seen in Figure 37. The malicious polishing and etching of the LISe wafer were done to ensure proper metallization/photolithography and bonding to the Timepix ASIC to minimize the number of dead pixels.

Photolithography is a fabrication technique that allows for small (μm) level features on a photomask to be baked by using an ultraviolet (UV) light-activated resin (also called photoresist) onto the surface of the sample. The sample is then metalized using radio frequency (RF) plasma sputtering with our ATC-Orion 5 UHV Sputtering System from AJA International. After this sputtering system metalized 250 nm of gold, the sample is placed in a photoresist remover, where the photoresist is removed. When done correctly, any surface of the sample that does not have photoresist on it will be covered with an even contact layer allowing for complex designs and fine features to be metalized. Indium and gold are both the most common metal contacts used for LISe. From here, the sample is then flip-chip bump bonded to a Timepix ASIC, which has 256 × 256 square pixels with a pitch of 55 μm. This system allows pixels to be read out individually, allowing for a system that provides 55 μm spatial resolution. It is worth noting that charge centroiding can be used for sub-55 μm spatial resolution but requires data post-processing.

From here, the ASIC/sensor stack was wire bonded to the signal bond pads of our X-Ray Imatek baby board seen on the right side of Figure 38 by a private company. The X-Ray Imatek baby board is a readout printed circuit board (PCB) that allows a single Timepix to be controlled by the readout electronics module. An image of this final system

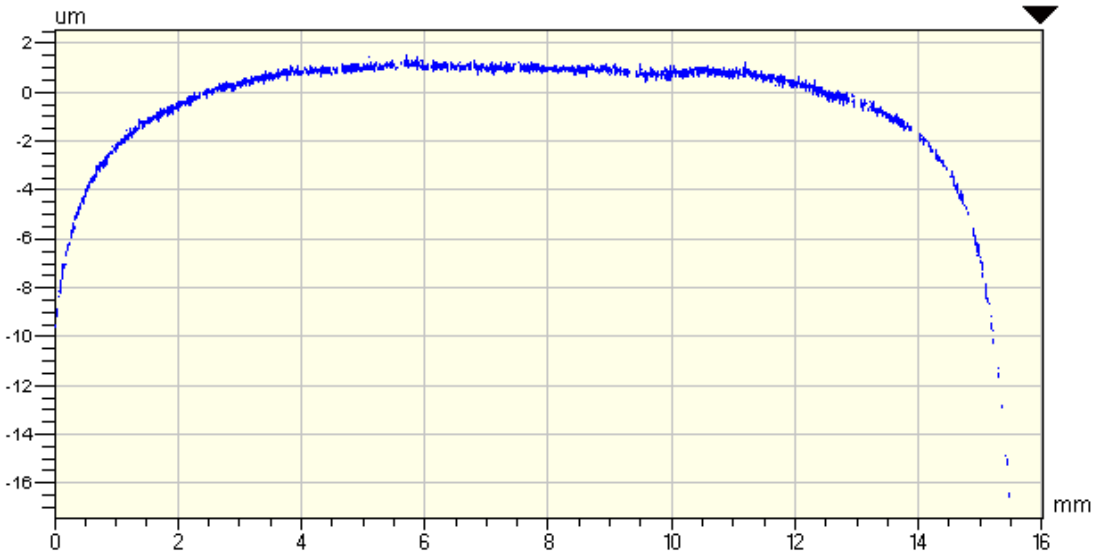

Figure 36. Interferometer results for the Y-profile (vertical) polished LISe sample. This sample was measured to be 0.7798 mm before being chemically etched.

Figure 37. A polished LISe sample before being chemically etched. The interferometer results for the Y-profile (vertical) of this sample can be seen in Figure 36.

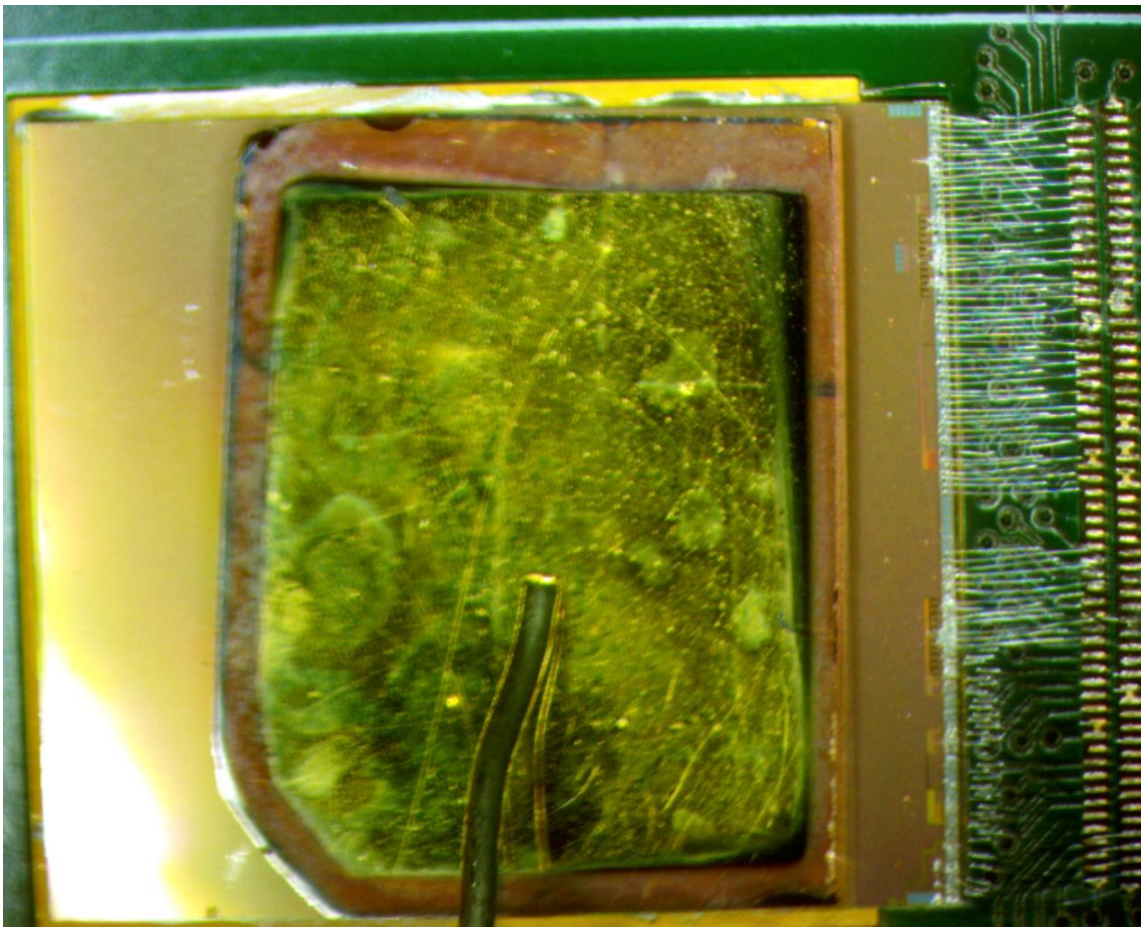

Figure 38. A LISe wafer flip-chip bump bonded to a Timepix ASIC and wire bonded to a X-Ray Imatek daughter board (eX Board). The LISe sample can be seen in Figure 37 before etching, metallization, and mounting to the ASIC. After mounting it to the ASIC, the sample was cracked and scratched.

can be seen in Figure 38, while a zoomed-in image of the vertical crack can be seen in Figure 39. Note that the sample was perfectly polished/etched and had no cracks before the flip chip bump-bonding to the ASIC. After bonding to the ASIC, two cracks appear to go through the sample, a vertical and horizontal crack. A previously published LISe imager has shown good performance even after the sample has been cracked, so this device should still work as intended [57].

After using the ribbon cable in Figure 40 to connect the X-Ray Imatek baby board to the ex Data acquisition board (ex DAQ) the graphic user interface (GUI) for the X-Ray Imatek imaging software was unable to recognize the ASIC Chip identification (ID) and operate. The chip ID is read from the chip on the same signal lines as the pixel value. For serial readout mode, it will be read out on a single line; for parallel readout, it will be read out on all 32 lines. It is evident that there are several faulty wire bonds that prevent our detector from operating correctly which can be seen in Figure 41. Reference wire bonds can be seen on the left side of Figure 41, and the wire bonds performed by a private company can be seen on the right side.

To determine the location of faulty wire bonds, we connected the ribbon cable (Figure 40) to the X-Ray Imatek baby board and read the output pin-by-pin, comparing the results to the readout circuit diagrams (provided by X-Ray Imatek). After reading out pin-by-pin and comparing the results from the electronics diagram (eX board), it was determined that eight faulty wire bonds existed between the ASIC and the X-Ray Imatek daughter board. A summary of these faulty wire bonds can be found in Table 9, where BGND stands for board ground, and the X's in the second column denote pads that were not meant to be wire bonded at all. Due to these faulty wire bonds, this LISe detector does not operate. It is worth noting that an additional two large area LISe wafers have been polished, metalized, and flip-chip bump-bonded to ASICs but have yet to be tested with a new readout system, but will likely be tested in the near future.

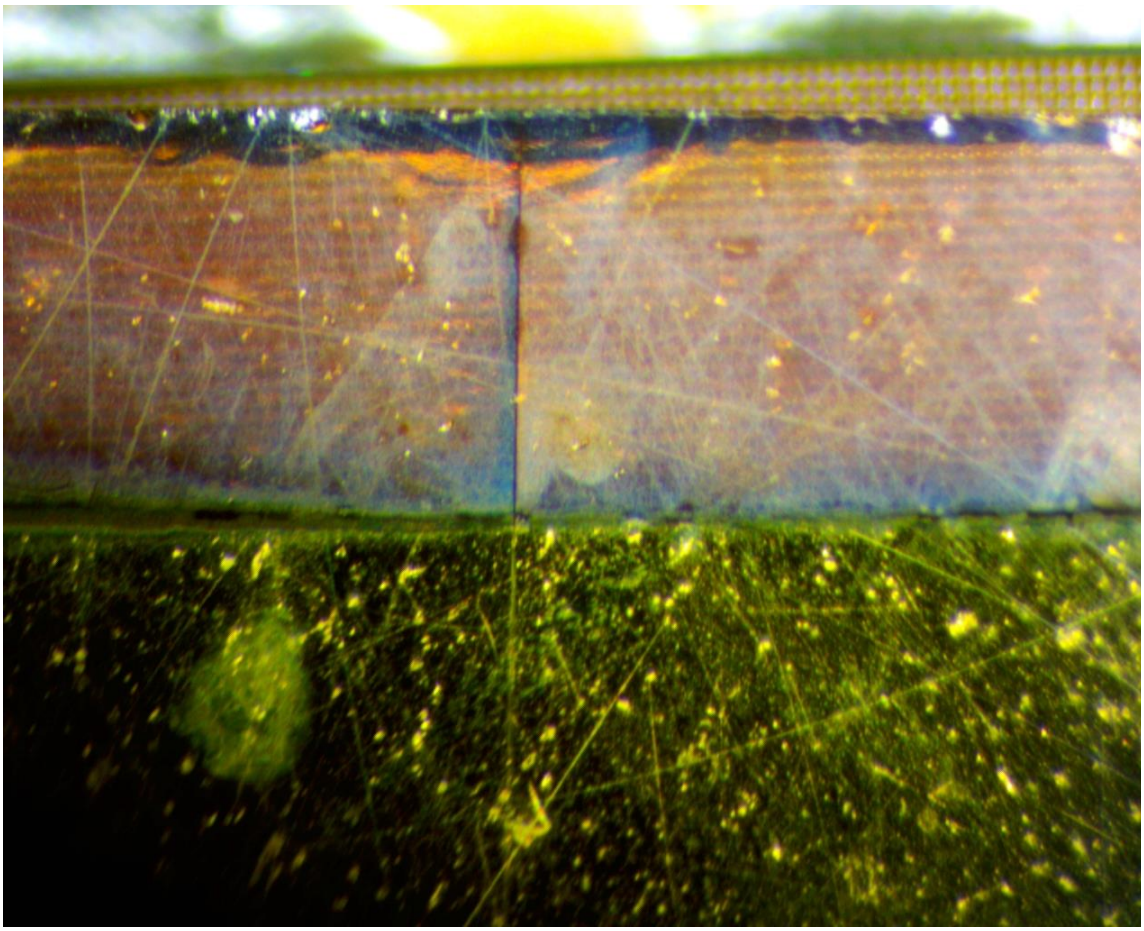

Figure 39. Zoomed-in image of the crack that appears in the top of Figure 38. This crack runs lengthwise down the LISe semiconductor and appeared during flip-chip bump bonding the LISe sample to the ASIC.

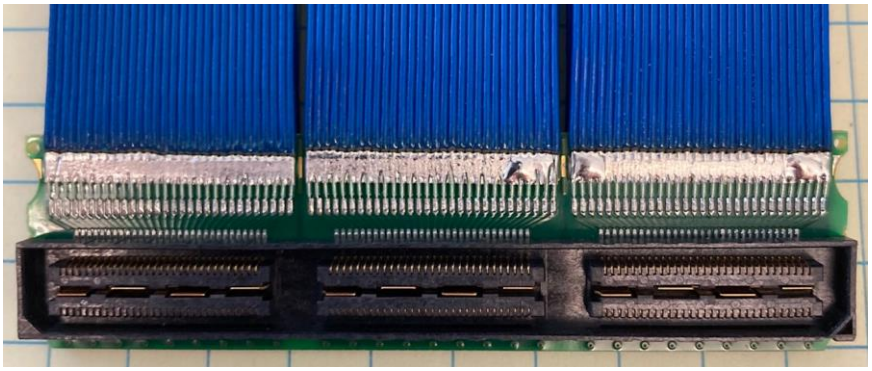

Figure 40. Ribbon Cable that is used for communication between the baby board and data acquisition board. Individual pins were read out to determine which wire bonds were faulty.

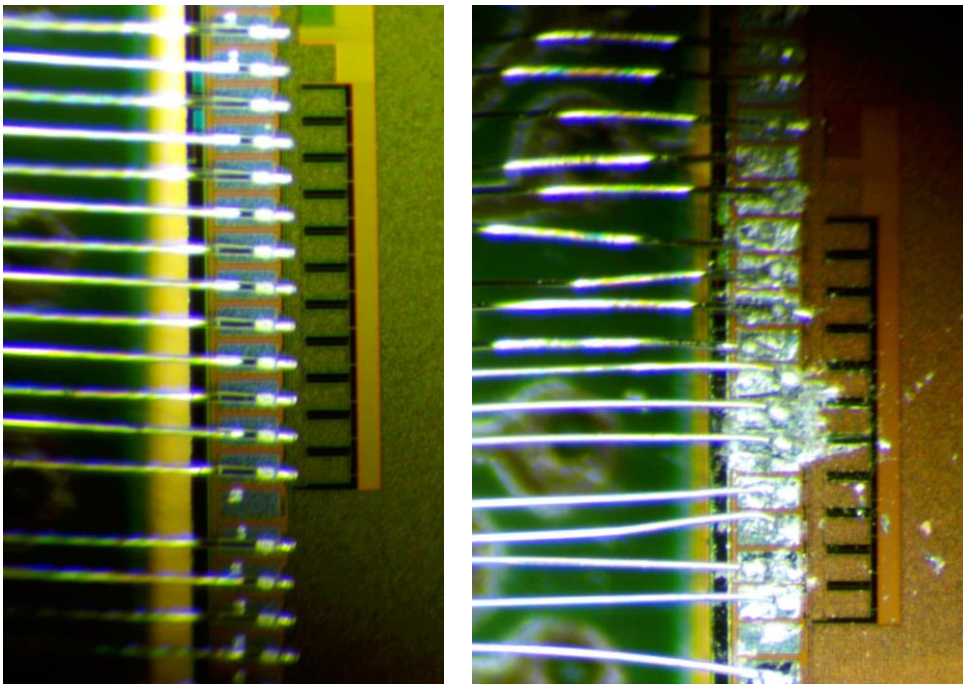

Figure 41. Left Image, reference wire bonds from a working LISe detector flip-chip bump bonded to a Timepix ASIC [57]. Right image, wire bonds for a LISe imager performed by a private company.

Table 9. Wire Bonding Summary of Shorted Pins

Pin Number	Pin Description	Shorted To
20	L0.D12	BGND
151	BGND	BGDN
152	BGND	BGND
157	X	PIN 158
158	NTC_HOT1	PIN 157
169	X	BGND
171	POLARITY_SEL	BGND
173	2V5_LANE1_A	BGND

2.8 Development of a LIPSe DSSD

Since LIPSe exhibits greater hole transport than LISe, we have selected it as the material for our Lithium-based semiconductor using a DSSD design. Since this is a new material, several small-scale tests must be performed to build a working detector. First, we tested the chemical compatibility of LIPSe with a new non-water-based photoresist for photolithography. Next, we tested wire bonding a large area (strip width/pitch of 200/350 µm) LIPSe DSSD. Lastly, we developed a novel layered detector design for a small area (strip width/pitch of 20/30 µm). This section will discuss the results of these endeavors.

LIPSe is very hydrophilic (dissolves in water), so we had to find a new positive photoresist for photolithography. Due to the high cost of this new photoresist (PR1-1000A), we tested the chemical compatibility of a LIPSe sample with all components of the photoresist, developer, thinner, resist remover, and stopper. To this end, a LIPSe sample was submerged for 30 minutes in a petri dish containing dibasic esters, ethylbenzene, anisole, dimethyl succinate, and octane. These chemicals comprise all components of the water-free photolithography process, and the LIPSe sample was stable after 30-minute exposures to each.

Due to the soft nature of LIPSe, we wanted to see if wire bonding was a viable option for connecting the strip electrodes to the readout board. Wire bonding is used to mount the top face of a DSSD semiconductor to the readout electronics and is a critical step. To this end, we metalized a preliminary LIPSe sample with a DSSD design using a shadow mask with an internal dimension of 4.4×4.4 mm^2, with a strip width of 200 µm and strip pitch of 350 µm. Eleven strips are on each side of the LIPSe sample, which is ~150 thick. This small area LIPSe sample metalized with 250 nm of gold can be seen in Figure 42 and was sent to the Princeton Material Institute for wire bonding. Both ball and wedge bonding were tested at the Princeton Material Institute, and some of the results can be seen in Figure 43. Due to this material's ductile/malleable nature, it craters during the compression stage for ball bonding and the sonication stage for wedge bonding. A LIPSe sample with an indium contact was also tested at the Princeton Material Institute with similar results. Another LIPSe sample was metalized with planar indium contacts and

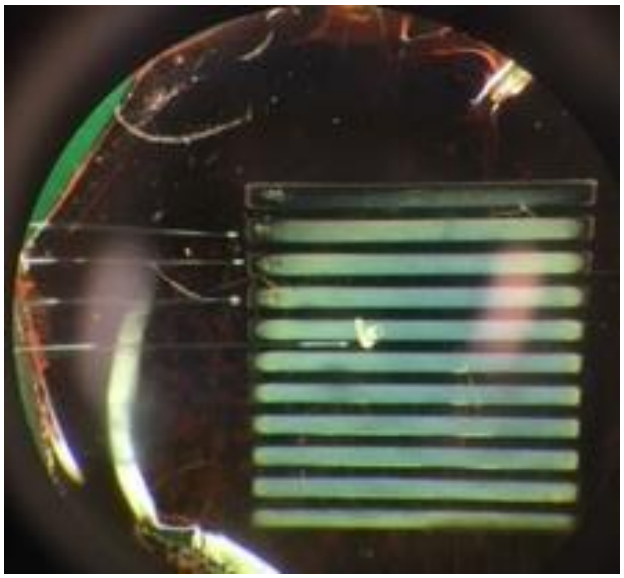

Figure 42. LIPSe DSSD wire bonded at Princeton Materials Institute.

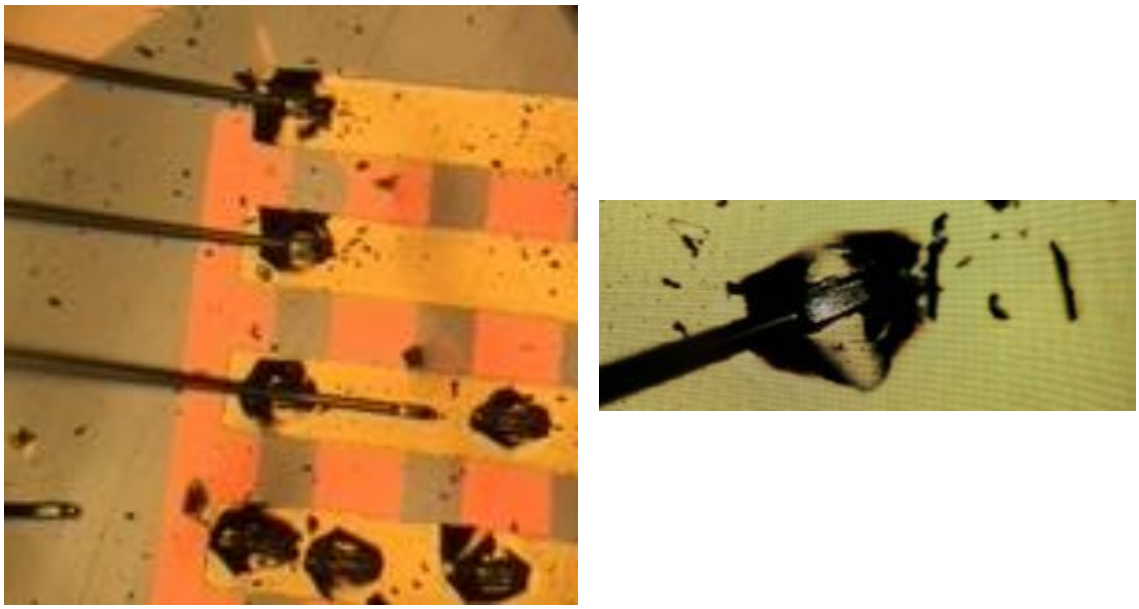

Figure 43. Zoomed-in image of a LIPSe DSSD wire bonded at Princeton Materials Institute. Right image is of a single wire bond. Take note of the cratering around the bond.

tested for adhesion; no usable data was taken with this sample because the contacts peeled off after touching the test-board contact pin. An image of the planar contact post-testing can be seen in Figure 44. It is worth noting that indium and gold contacts do not appear to have excellent adhesion to LIPSe, but offer excellent adhesion to LISe. Laser bonding was also researched; however, the minimum ribbon current systems can laser bond is just under 1 mm. Since we cannot wire bond with LIPSe, we explored using an anisotropic conductive film (ACF) adhesive to bond the LIPSe detector to the readout electronics on both sides of the sensor. The conductive particles in this film have a diameter of 3 μm and are made of a Ni-Au polymer, allowing us to connect strip electrodes as small as 10 μm to the PCB. The bottom side of the sensor will be bonded directly to the PCB, and the top side will be connected to a readout flex cable that will be plugged into the board. Bonding a LIPSe DSSD to a readout flex cable resulted in the gold contact being peeled off of LIPSe. This indicates to us that there is poor contact adhesion between gold and LIPSe. For this reason, it is recommended that we explore more materials for LIPSe contacts in the future.

We have developed a novel DSSD design to preliminary test the performance of the η-function. A schematic of this design can be seen in Figure 45. This design uses a non-conductive contact (SiO_2) to cover the sample's surface except for a small square in the middle for strip electrodes. Allowing for thirty-two strip electrons with a strip width/pitch of 20/30 on each sample side. The strips end with large area contact pads (110×110 μm) for connecting the sample to the board using ACF. The SOLIDWORKS design for the photomask of this electrode design can be seen in Figure 46, and for the non-conductive contact in Figure 47. This was developed after the first initial test bond of LIPSe with ACF to the readout cable removed the contact from the surface of LIPSe. The gold contacts should not peel off since the gold will be sputtered onto SiO_2 instead of directly on the surface of LIPSe. This non-conductive contact should allow for much better adhesion between the strip electrodes, ACF, and the flex readout cable.

SiO_2, also known as glass, is used in a variety of applications as a non-conductive contact. Various reports in the literature state that SiO_2 must be sputtered with excess oxygen, while other reports contradict this statement [108, 109]. Without adding an oxygen tank to our sputtering system, we wanted to determine if we could sputter SiO_2 under a

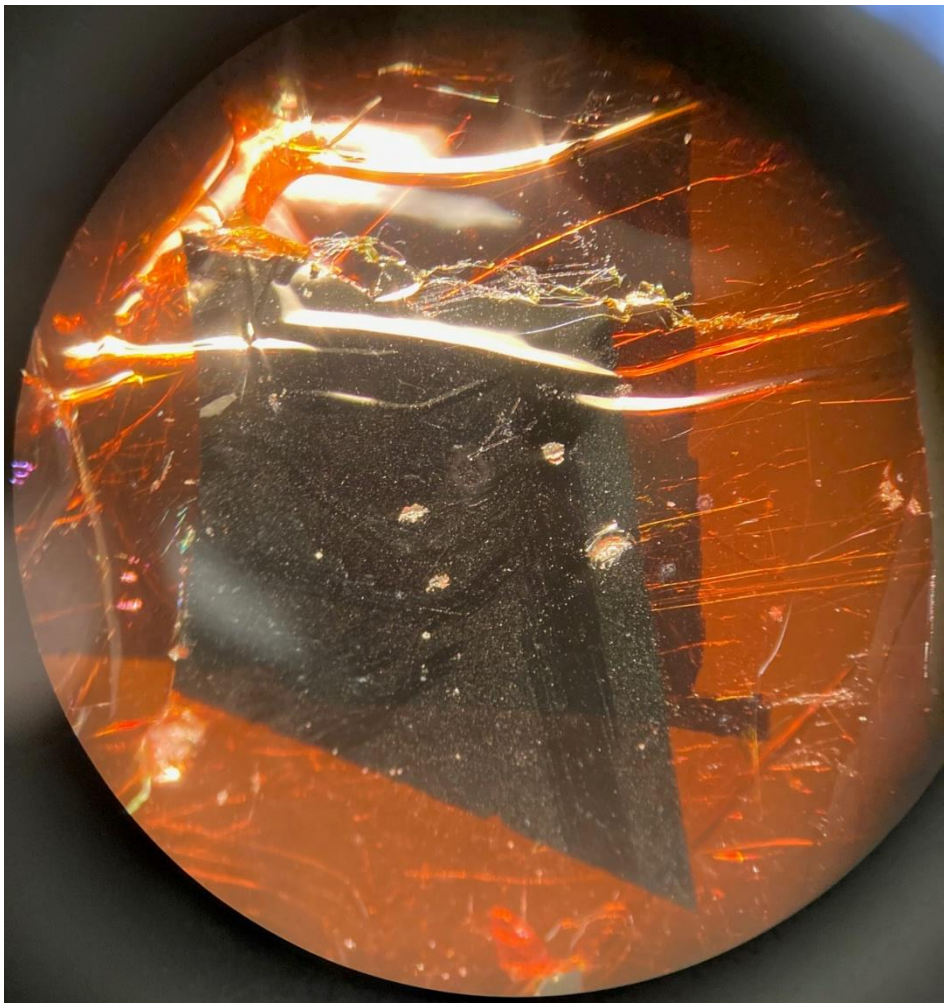

Figure 44. Image of a LIPSe sample metalized with planar indium contacts for testing. Note that the pogo contact pin peeled the contact away wherever it touched the indium contact.

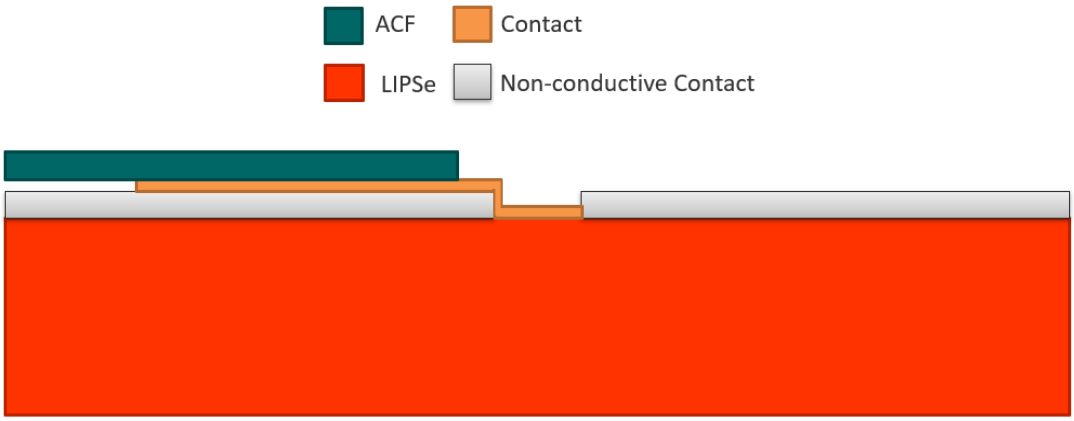

Figure 45. Novel detector design for a 32 strip DSSD Design with a strip width/pitch of 20/30 µm.

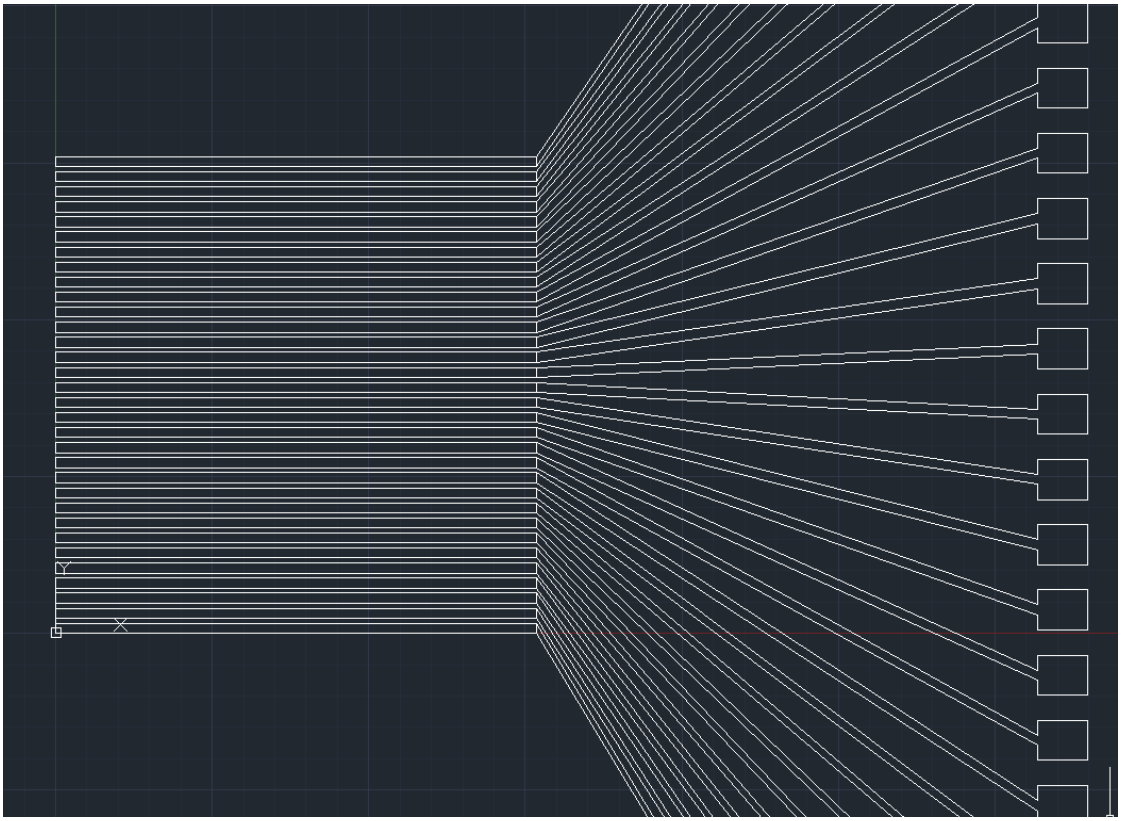

Figure 46. Shadow mask for a DSSD strip width/pitch of 20/30. There are 32 strips on each side.

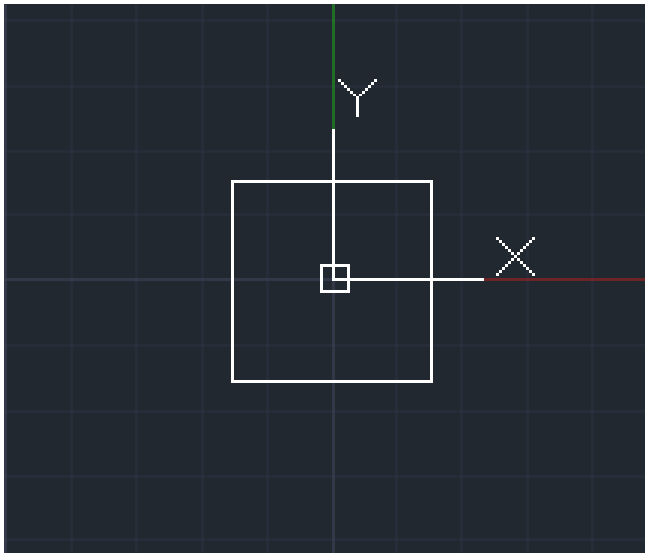

Figure 47. Shadow mask for the non-conductive contact to be applied to LIPSe before metalizing with gold for the DSSD Design. SiO_2 was selected for the non-conductive contact. The length of the large square in the middle is 960 µm.

vacuum without excess oxygen. Additionally, we wanted to ensure that we were sputtering SiO_2 instead of either Si or SiO. To do this, 10 nm of SiO_2 was sputtered on half of a LIPSe sample, seen in Figures 48-49, and interferometer, scanning electron microscope (SEM), and energy dispersive X-ray spectroscopy (EDS) measurements were taken.

The interferometer results can be seen in Figure 50 and show a clear indication that either Si, SiO, or SiO_2 was sputtered on the sample's surface. To confirm the presence of oxygen on the surface of the sample, SEM and EDS measurements were taken at the Electron Microscopy Center using a Zeiss EVO SEM and Bruker EDS system. An SEM image of SiO_2 on the surface of LIPSe can be seen in Figure 51. EDS was taken at three different points on the sample, and the results can be seen in Table 10. From these results, it is evident that excess oxygen is not required to rf-sputter SiO_2 onto the surface of LIPSe.

Further research needs to be performed to determine the optimal contact for LIPSe; gold and indium are good but not excellent contacts with this newly discovered semiconductor. The photolithography process to make this device will consist of a four-step process. First, photolithography with the non-conductive photomask will need to be performed. Then, the sample must be metalized with a thin layer (~4 nm) of SiO_2, and photolithography with the DSSD design will be performed. From here, the sample would need to be flipped and repeated to create perpendicular strips on the back face of the sample. From here, the bottom side of the sample would be bonded with ACF directly to the PCB. The top side of the sample would be bonded with ACF to a flexible readout cable. The research thus far lays the groundwork for making a DSSD with LIPSe.

2.9 LIPSe Gamma/Neutron Discrimination

In addition to DSSD designs, we are developing pixelated LIPSe detectors for an imaging beamline. The current sensors at this beamline employ Lithium-6 loaded glass, offering 1 mm spatial resolution and a neutron-gamma discrimination ratio of approximately 105 [105]. We have been tasked with providing a detector that increases the spatial resolution to 0.5 mm and offers neutron-gamma discrimination greater than 107. A

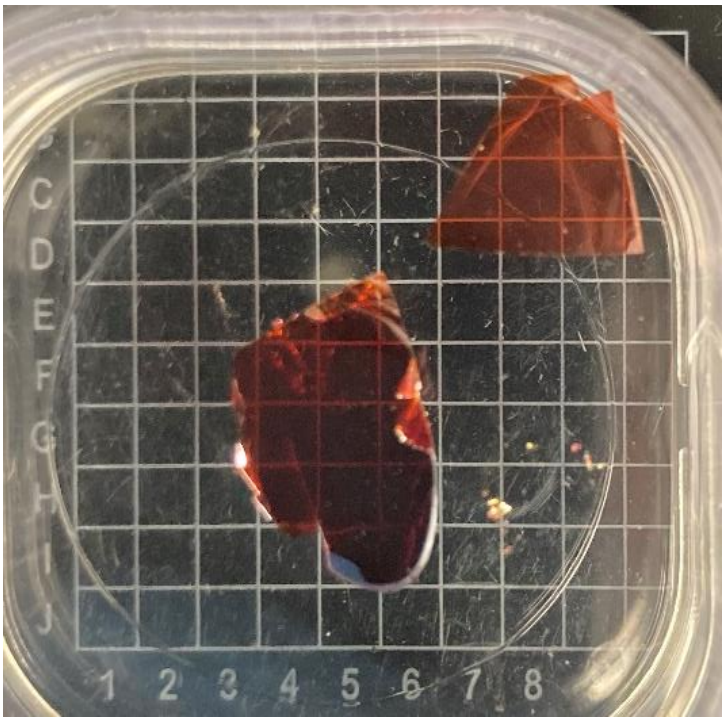

Figure 48. LIPSe sample (top-right) before metallization with indium, which can be seen in Figure 44. LIPSe sample (middle) was metalized with SiO_2 to test the adhesion, which can be seen in Figure 49.

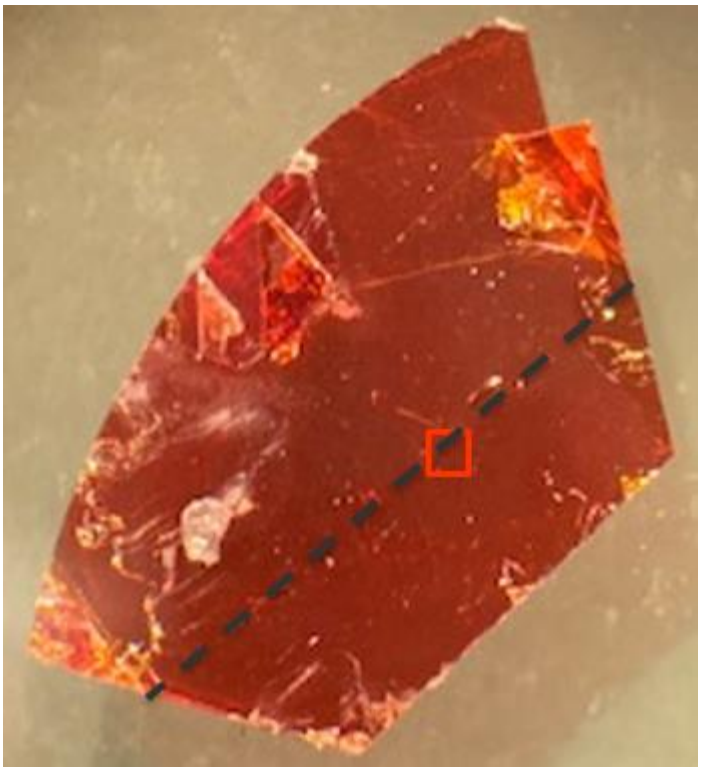

Figure 49. LIPSe sputtered with SiO_2. The top side of the dashed black line is where SiO_2 was sputtered. The red box is where interferometer measurements were taken.

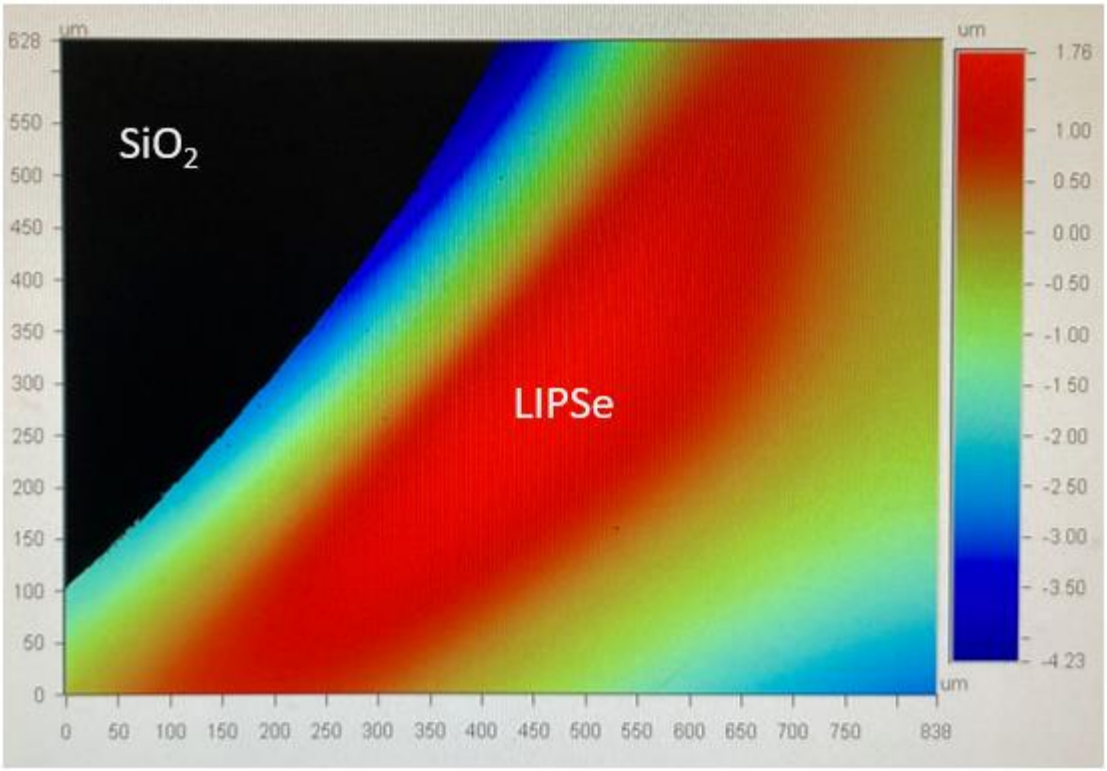

Figure 50. Interferometer measurements for the boxed region in Figure 49. Note the sharp line indicating SiO_2 is present on the surface of the sample.

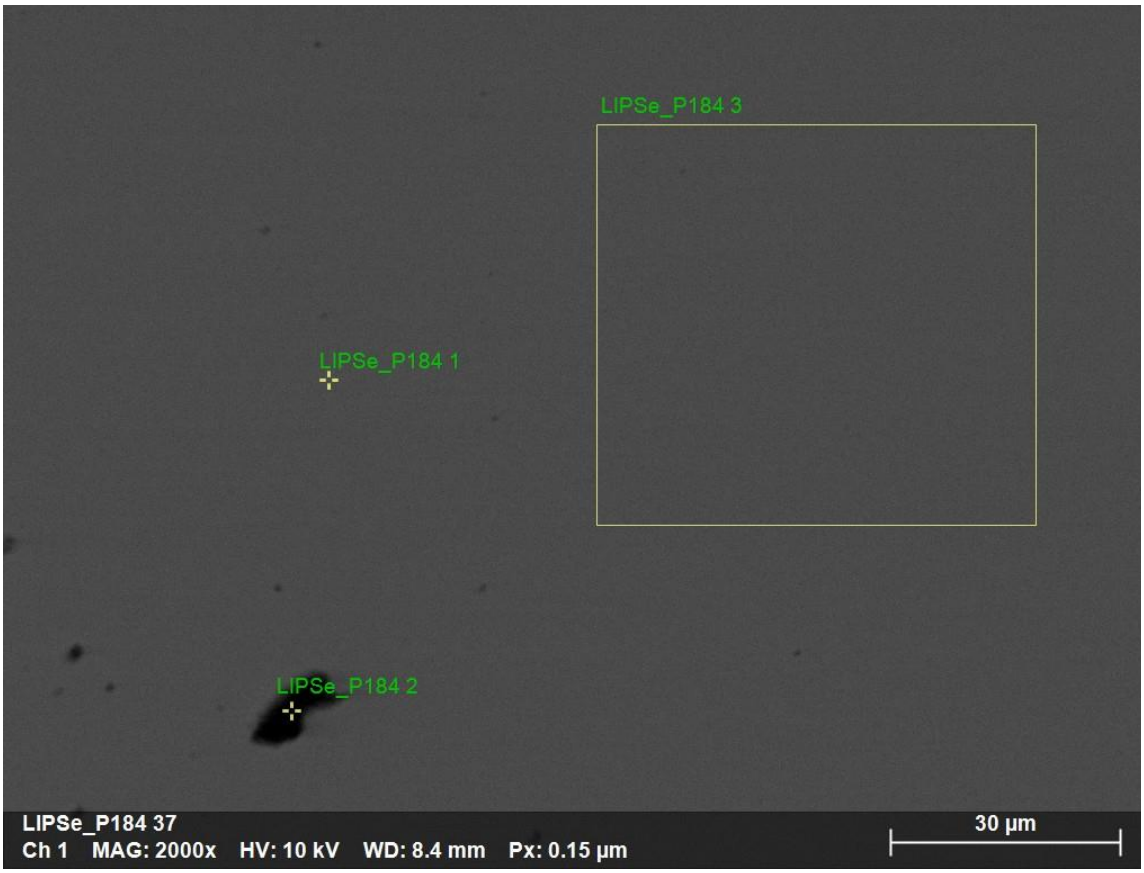

Figure 51. SEM image of a LIPSe sample with 10 nm of SiO_2 sputtered on the surface. SEM-EDS measurements were taken at the three regions identified above. SEM-EDS does not measure lithium content.

Table 10: SEM-EDS results for normalized mass concentration (%).

Spectrum	Oxygen	Silicon	Phosphorus	Selenium	Indium
LIPSe_P184 1	1.96	2.22	8.37	70.81	16.63
LIPSe_P184 2	3.83	3.47	8.84	68.95	14.91
LIPSe_P184 3	2.37	2.28	8.48	70.50	16.37
Mean	2.72	2.66	8.56	70.09	15.97
Sigma	0.98	0.70	0.24	0.99	0.93
Sigma Mean	0.57	0.41	0.14	0.57	0.54

review of interactions with matter can be found in the Appendix. The goal of these simulations is to computationally evaluate LIPSe to replace these detectors, related explicitly to gamma-neutron discrimination. Since LIPSe is a recently discovered material, we wanted to computationally show that by using threshold discrimination in a pixelated device, neutron/gamma discrimination is possible.

When a gamma ray interacts with LIPSe or LISe, an electron is created that causes direct ionization, allowing us to generate a signal from our detector. We can use the attenuation coefficients of LIPSe, in Figure 52, to determine the mode of interaction that occurs. To this end, a unique material was created using ESTAR to assess the range of electrons in LIPSe, as seen in Figure 53. We conducted MCNP6.2 simulations of a 1.5 mm thick LIPSe sensor with a 300 μm pixel pitch to evaluate the signal spread over a pixelated device. An isotopically emitting monoenergetic electron source was generated in the middle of the 3×3 pixelated device. We evaluated the energies for the electron source of 0.1 MeV, 0.5 MeV, 2.5 MeV, and 7 MeV. In a pixelated device, the signal generated on the pixels is a function of the weighting potential of that individual pixel, with the weighting potential being a function of the pixel pitch and device thickness. As one can see, when the bulk material (in this case, LIPSe) is thicker relative to the pixel pitch, most of the signal is generated by the charge moving near the collecting electrode. The weighting potential for this device can be seen in Figure 54, and a two-dimensional slice of this weighting potential can be seen in Figure 55.

At very low energies, 0.1 MeV, the electron cloud is localized under a single pixel and can be seen in Figure 56. Increasing the electron's energy to 0.5 MeV results in the energy deposited by this electron spread across multiple pixels in Figure 57. As the energy of the electrons increases from 0.5 MeV to 2.7 and 7 MeV in Figures 58-59, most of the energy deposited by these electrons will be shared across all of the pixels and escape the simulated device. Considering these results, time-over-threshold (TOT) methods will allow for easy discrimination of gamma/neutrons interactions in LIPSe.

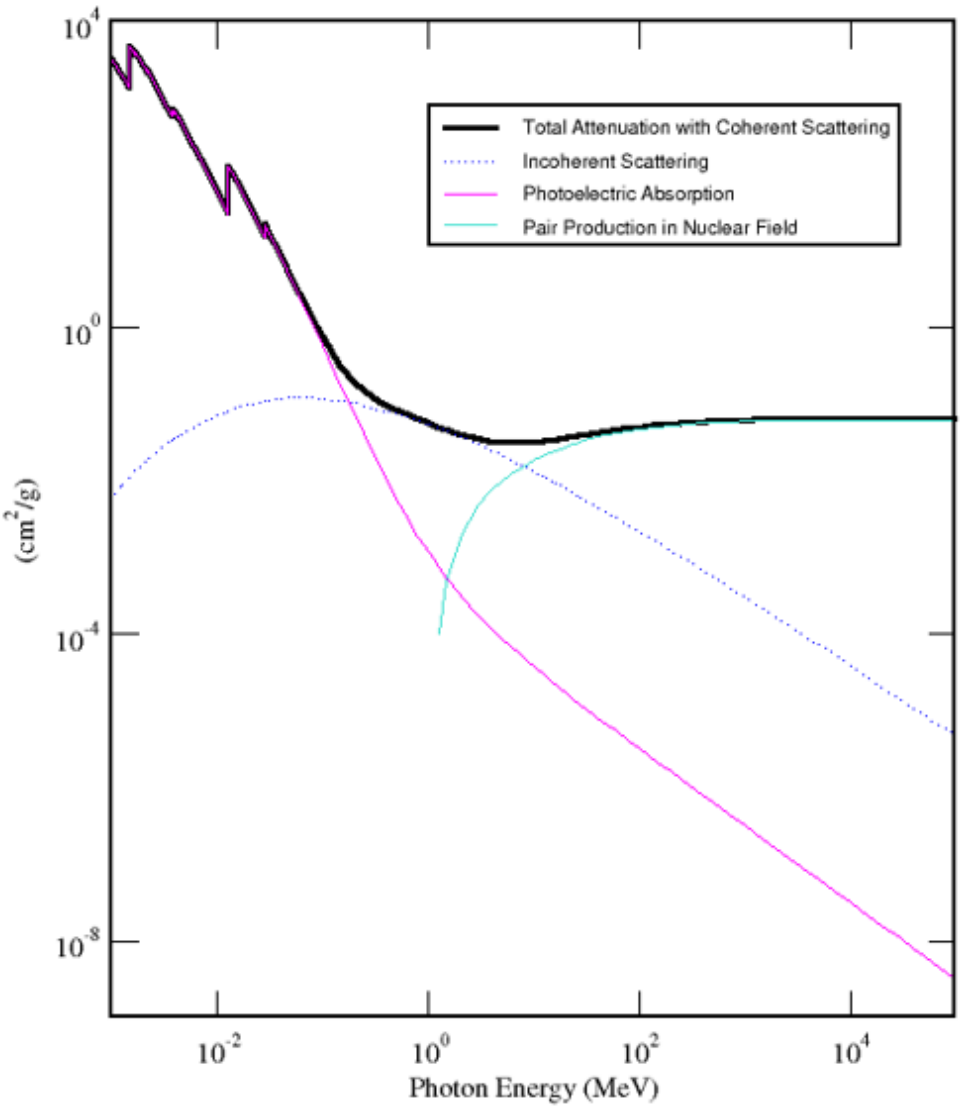

Figure 52. Mass attenuation coefficient of gamma rays interacting with LIPSe.

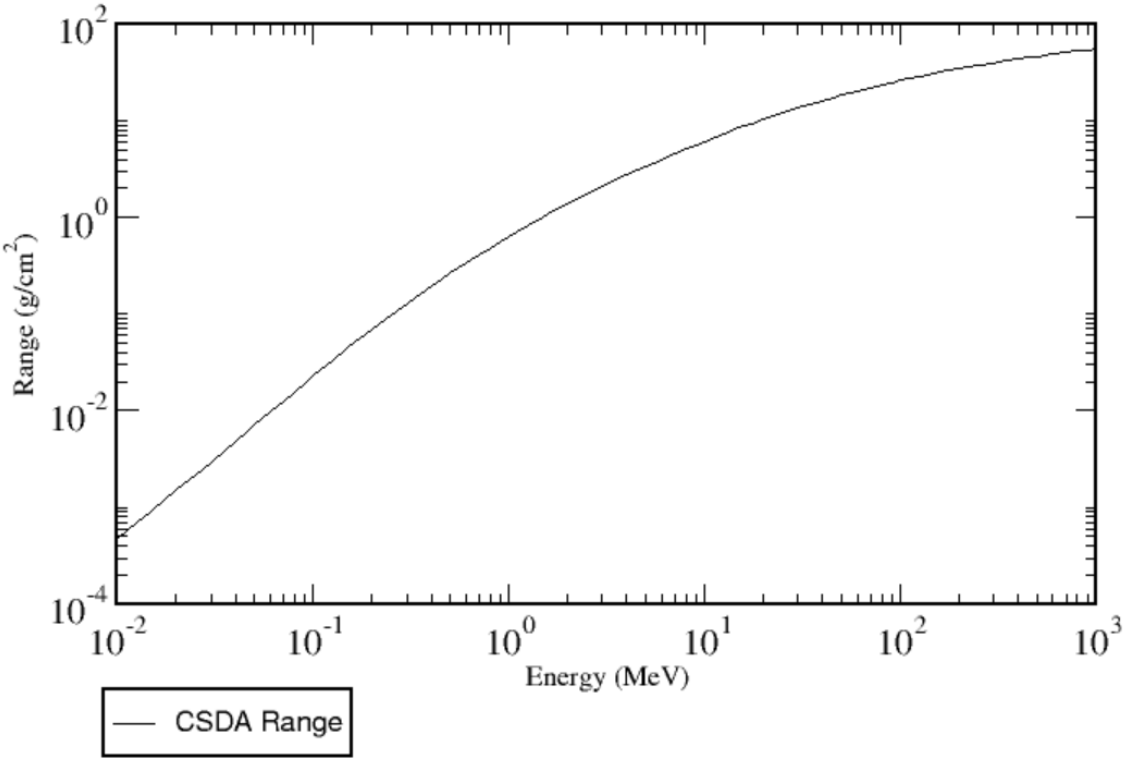

Figure 53. ESTAR-calculated CSDA range of electrons in LIPSe. A mean excitation energy of 335.4 eV and density of 4.615 g/cm^3 were used for this simulation.

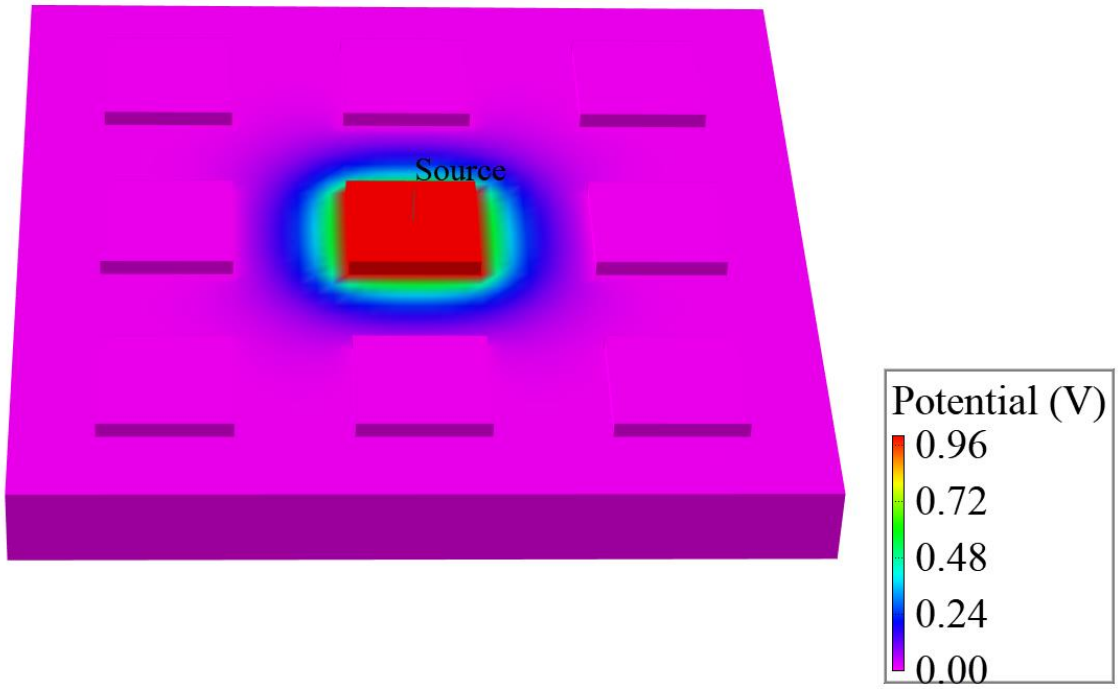

Figure 54. SILVACO simulation for the weighting potential of a pixelated LIPSe device. The contacts are the raised square pixels seen in the image above.

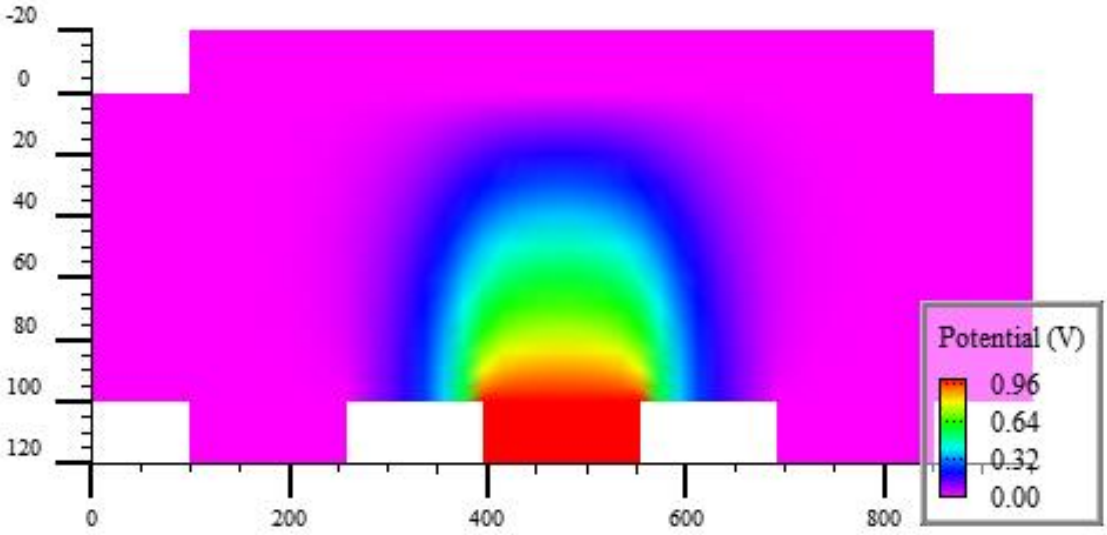

Figure 55. Two-dimensional slice of the weighting potential in the middle of a pixelated LIPSe device. The gold contacts extend from -20 to 0 and 100 to 120 in the Y-dimension.

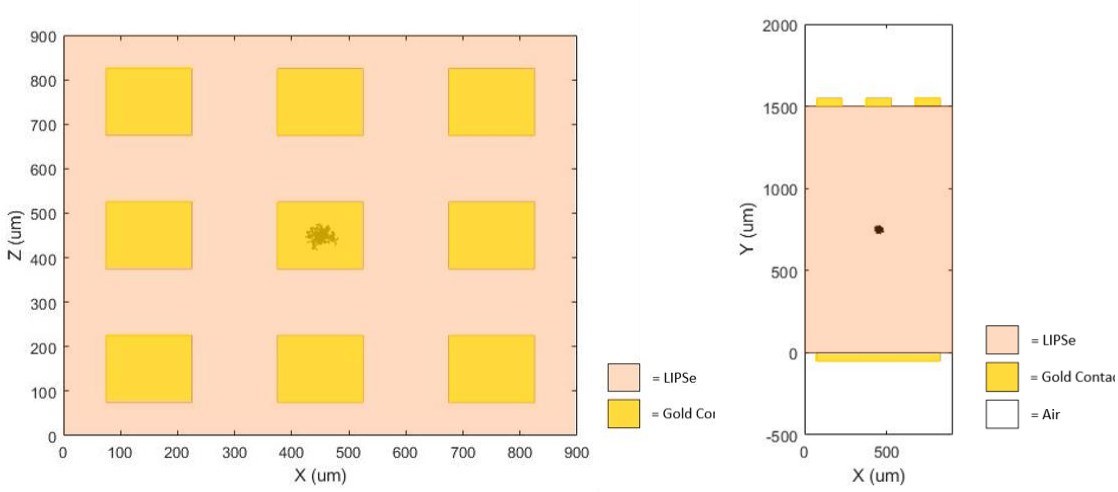

Figure 56. Left: Top-down view of a MCNP6 simulation of 100 keV electrons generated below the center pixelated electrode. Right: Side view of a MCNP6 simulation of 100 keV electrons generated in the middle of the LIPSe detector.

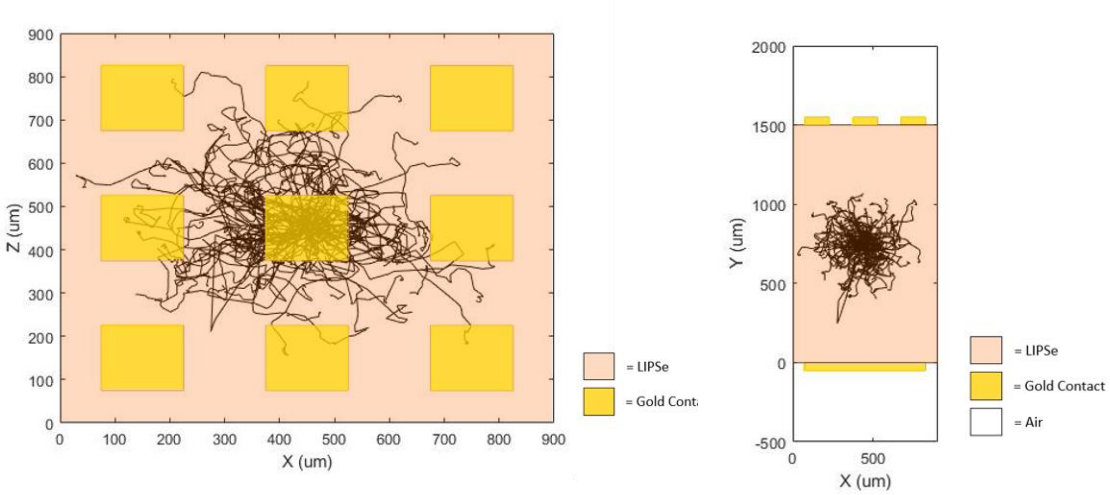

Figure 57. Left: Top-down view of a MCNP6 simulation of 500 keV electrons generated below the center pixelated electrode. Right: Side view of a MCNP6 simulation of 500 keV electrons generated in the middle of the LIPSe detector.

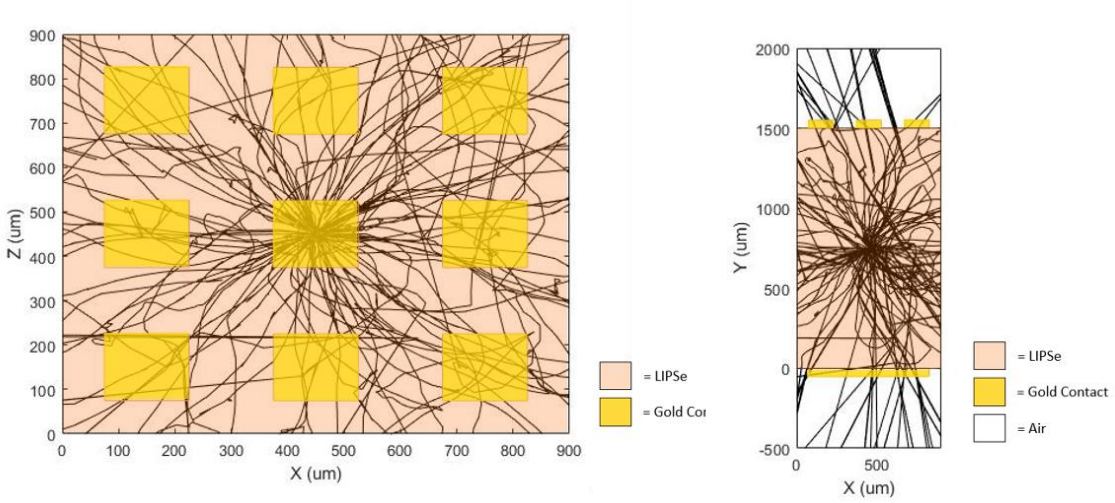

Figure 58**.** Left: Top-down view of a MCNP6 simulation of 2.5 MeV electrons generated below the center pixelated electrode. Right: Side view of a MCNP6 simulation of 2.5 MeV electrons generated in the middle of the LIPSe detector.

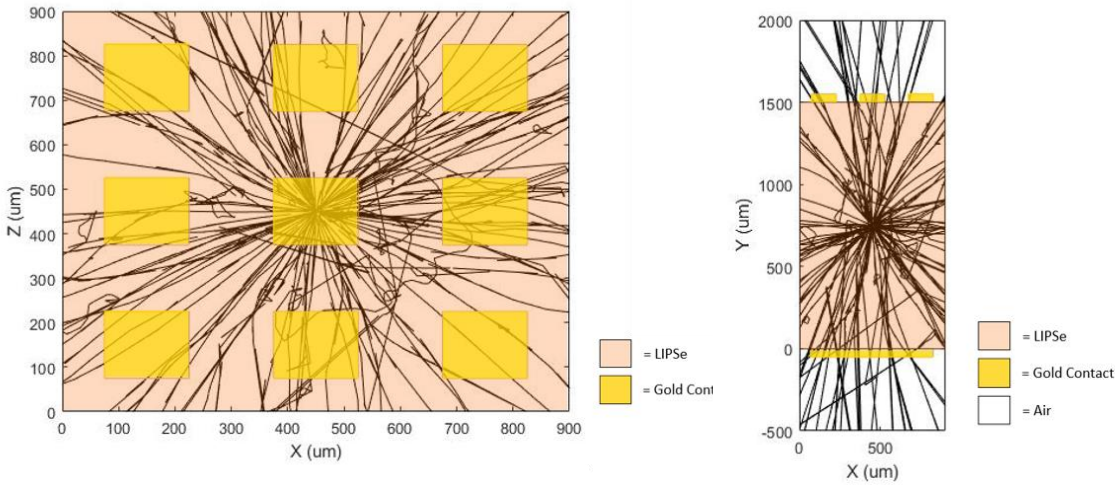

Figure 59. Left: Top-down view of a MCNP6 simulation of 7 MeV electrons generated below the center pixelated electrode. Right: Side view of a MCNP6 simulation of 7 MeV electrons generated in the middle of the LIPSe detector.

2.10 Converting a η-function into C++ for a LIPSe DSSD

It is essential to deploy the models that have been trained into a format that can be used by the detector system. Additionally, some progress still needs to be made on the FPGA programming to make this detector system a functional DSSD for neutron imaging. The goal of this system is to offer real-time imaging with high spatial resolution, with a focus on energy resonance imaging. The models selected to deploy with our detector system must be programmed in C++ for implementation. This will allow our detector to provide a real-time reconstruction of the neutron interaction locations at neutron imaging facilities.

The MATLAB Code Generation Application is used to generate the trained models into C++ code to fit into a format we can package with our detector system. These models can make between 2.6×10^6 and 2.7×10^6 observations or predictions per second. Considering the average thermal neutron flux at SNS is 4×10^{13} neutrons per centimeter squared per second and the LIPSe DDSD design is for an active imaging area of ~1 mm, 4×10^{12} neutrons will hit our detector each second. Additionally, it is worth factoring in the neutron detection efficiency of LIPSe, which is ~22 percent for a 1 mm sample and ~70 percent for a 1 cm sample. Since most LIPSe samples are on the order of 1 mm thick, our detector interacts with (records) ~8.8×10^{11} neutrons per second. From here, a 10-minute neutron experiment at SNS would result in a post-processing time of ~3.9 days. Due to this, it is recommended that after recording data on the detector side, the prediction (ML Models) are run in parallel such that the post-processing time is greatly diminished. The ML Models in our detector package allow for real-time imaging up to ~2.6×10^6 neutron counts per second for our small area LIPSe design but will require some minimal post-processing time if the count rate is above this.

CHAPTER THREE: CONCLUSIONS

A modified η-function for lithium-based semiconductors has been developed that is comprised of high-fidelity semiconductor simulations (based on Shockley-Ramo Theorem), neutron interactions within LISe and LIPSe, charge induction on strip electrodes, and machine learning models. These simulations have allowed us to computationally determine the strip electrode width/pitch that optimizes the tradeoff between signal integrity and reconstruction of the neutron absorption location to consist of two DSSD designs, using a strip width/pitch of 10/15 and 20/30 μm. Either of these designs will enable us to meet our spatial resolution goal of sub-5 μm. To date, there is no public record of anyone simulating a neuron-sensitive semiconductor for neutron imaging that meets our goal spatial resolution of sub-5 μm. This research will allow us to achieve unparalleled neutron detection efficiency, spatial resolution, and timing resolution detection. The improvements upon current neutron imaging systems has the opportunity to open new avenues of research that are not possible today.

The coarse regression trees and neutron networks have shown that they are robust enough to perform well even with the addition of 1,000 e^- of Gaussian noise to validation datasets. We also learned that CCE plays a vital role in the model performance. When the CCE is low (0.1) compared to the ideal simulations (1) neutral networks and regression trees are unable to reconstruct simulated induced signal data. Before an η-function is developed for new Lithium-based semiconductors, the CCE should be measured and incorporated into the simulations such that the models are able to accurately reconstruct real-world induced signal data. Radiation damage will change the expected response of the semiconductor, and will need to be accounted for in future simulations. Future work should focus on improving the fidelity of and making the charge transport code more realistic by adding things such as detrapping and diffusion. Additionally, some progress still needs to be made on the FPGA programming to make this detector system a functional DSSD for neutron imaging.

Significant effort has been made to produce working LISe detectors coupled to the Timepix ASIC and a small-area LIPSe DSSD detector. The main challenges with the LISe detector have been sample cracking while flip-chip bump-bonding to the ASIC, and faulty wire bonds to the readout PCB. It was determined that there were eight faulty wire bonds that prevented this detector from operating. In addition to this faulty detector, two large area LISe wafers were polished, metalized, and flip-chip bump-bonded to ASICs, and properly wire bonded to a new readout system for testing this year. Seeing as LIPSe is a recently discovered material, my research has laid the groundwork for using this material in a DSSD design. The chemical compatibility of LIPSe with a new non-water-based photoresist has been tested and the photolithography recipe has been optimized for use. It was discovered that due to LIPSe's ductile/malleable nature it craters during wire bonding, so we are unable to wire bond the strips of a DSSD design directly to the readout board. To this end, a novel DSSD design has been developed to test the performance of the η-function

For the η-function to work ideally, the semiconductor must have both electron and hole transport. To this end, it is important to improve the quality of LISe semiconductors and increase the thickness of LIPSe semiconductors produced. LIPSe has both electron and hole transport, but is currently limited in its' thickness due to the current growth method, CVT growth. On the other hand, LISe is grown using the vertical Bridgeman method, but has poor hole response. It would be valuable to the scientific community to explore improvements, growth and quality, for these two lithium-based semiconductors.

LIST OF REFERENCES

1. Chadwick, J.J.N., *Possible existence of a neutron.* 1932. **129**(3252): p. 312-312.
2. Kallmann, H.J.R., a.j.o. science, and i. applications, *Neutron radiography.* 1948. **1**(6): p. 254-260.
3. Thewlis, J.J.B.J.o.A.P., *Neutron radiography.* 1956. **7**(10): p. 345.
4. Hartmut, K. and K. Ernst, *Photographic detection of slowly moving neutrons*. 1940, Google Patents.
5. Hawkesworth, M. and J.J.J.o.M.S. Walker, *Radiography with neutrons.* 1969. **4**(9): p. 817-835.
6. Berger, H., W.J.N.S. Beck, and Engineering, *Neutron radiographic inspection of radioactive irradiated reactor fuel specimens.* 1963. **15**(4): p. 411-414.
7. Gabriel, T.A., J.R. Haines, and T.J.J.J.o.N.M. McManamy, *Overview of the Spallation Neutron Source (SNS) with emphasis on target systems.* 2003. **318**: p. 1-13.
8. Kim, S.-H., et al., *Overview of ten-year operation of the superconducting linear accelerator at the Spallation Neutron Source.* 2017. **852**: p. 20-32.
9. Mansur, L., et al., *R&D for the Spallation Neutron Source mercury target.* 2001. **296**(1-3): p. 1-16.
10. Floyd, C.E., et al., *Introduction to neutron stimulated emission computed tomography.* 2006. **51**(14): p. 3375.
11. Akiba, K., et al., *Charged particle tracking with the Timepix ASIC.* 2012. **661**(1): p. 31-49.
12. Riedel, R.J.O.i.r., *Overview of Data Acquisition at the SNS.* 2004.
13. Granroth, G., et al. *SEQUOIA: A newly operating chopper spectrometer at the SNS*. in *Journal of Physics: Conference Series*. 2010. IOP Publishing.
14. Strobl, M., et al., *Advances in neutron radiography and tomography.* 2009. **42**(24): p. 243001.
15. Harms, A.A. and D.R. Wyman, *Mathematics and physics of neutron radiography*. Vol. 1. 1986: Springer Science & Business Media.
16. Tremsin, A., et al., *Detection efficiency, spatial and timing resolution of thermal and cold neutron counting MCP detectors.* 2009. **604**(1-2): p. 140-143.

17. Carini, G., P. Denes, and S.J.D.O.o.S. Gruner, *Neutron and X-ray Detectors: Report of the Basic Energy Sciences Workshop on Neutron and X-ray Detectors.* 2012.
18. Kozhevnikov, S., et al., *Divergence of neutron microbeams from planar waveguides.* 2019. **915**: p. 54-64.
19. Anderson, I.S., R.L. McGreevy, and H.Z.J.S.S.B.M. Bilheux, LLC, *Neutron imaging and applications.* 2009. **2209**: p. 987-0.
20. Banhart, J., et al., *X-ray and neutron imaging–Complementary techniques for materials science and engineering.* 2010. **101**(9): p. 1069-1079.
21. Brooks, F., et al., *Neutron spectrometry—historical review and present status.* 2002. **476**(1-2): p. 1-11.
22. Martz, H.E., et al., *X-ray Imaging: fundamentals, industrial techniques and applications*. 2016: CRC Press.
23. Myhre, K.G., et al., *Nondestructive Tomographic Mapping of Uranium and Gadolinium Using Energy-Resolved Neutron Imaging*. 2018, Oak Ridge National Lab.(ORNL), Oak Ridge, TN (United States).
24. Shinohara, T., et al. *Final design of the energy-resolved neutron imaging system "RADEN" at J-PARC*. in *Journal of Physics: Conference Series*. 2016. IOP Publishing.
25. Koide, J., et al. *Super resolution for resonance absorption imaging by reconstruction with sub-pixel shifting*. in *2017 IEEE Nuclear Science Symposium and Medical Imaging Conference (NSS/MIC)*. 2017. IEEE.
26. Kardjilov, N., et al., *Advances in neutron imaging.* 2018. **21**(6): p. 652-672.
27. Granja, C., et al. *Spatially correlated and coincidence detection of fission fragments with the pixel detector timepix*. in *IEEE Nuclear Science Symposuim & Medical Imaging Conference*. 2010. IEEE.
28. Day, D., R.J.N.I. Sinclair, and Methods, *Neutron moderator assemblies for pulsed thermal neutron time-of-flight experiments.* 1969. **72**(3): p. 237-253.
29. Pomerance, H.J.P.R., *Thermal neutron capture cross sections.* 1952. **88**(2): p. 412.
30. Hamm, D.S., *Development and Characterization of Lithium Indium Diselenide for Neutron Detection and Imaging Applications.* 2018.

31. McGregor, D., et al., *Thermal neutron detection with pyrolytic boron nitride.* 2008. **591**(3): p. 530-533.
32. Kargar, A., et al., *LiInSe 2 for Semiconductor Neutron Detectors.* 2020. **8**: p. 78.
33. Manfredotti, C., et al., *SiC detectors for neutron monitoring.* 2005. **552**(1-2): p. 131-137.
34. Eschenauer, M., et al., *Resolution enhancement of gamma-spectroscopy data from neutron-damaged coaxial n-type HPGe-detectors.* 1994. **340**(2): p. 364-370.
35. Chaudhari, P., et al., *Fabrication and characterization of silicon based thermal neutron detector with hot wire chemical vapor deposited boron carbide converter*. 2015. **779**: p. 33-38.
36. Chica, D.G., et al., *Direct thermal neutron detection by the 2D semiconductor 6LiInP2Se6.* 2020. **577**(7790): p. 346-349.
37. Limousin, O.J.N.I., S. Methods in Physics Research Section A: Accelerators, Detectors, and A. Equipment, *New trends in CdTe and CdZnTe detectors for X-and gamma-ray applications.* 2003. **504**(1-3): p. 24-37.
38. Knoll, G.F., *Radiation detection and measurement*. 2010: John Wiley & Sons.
39. Bala, A., *Design and Simulation of a New Generation Radiation Detector for Oil and Gas Exploration*. 2021, University of York.
40. Riedel, R., et al., *Design and performance of a large area neutron sensitive anger camera.* 2015. **794**: p. 224-233.
41. Mayer, M., et al., *Development and characterization of a neutron detector based on a lithium glass–polymer composite.* 2015. **785**: p. 117-122.
42. Yehuda-Zada, Y., et al., *Optimization of 6LiF: ZnS (Ag) scintillator light yield using GEANT4.* 2018. **892**: p. 59-69.
43. Kouzes, R.T., et al., *Progress in alternative neutron detection to address the helium-3 shortage.* 2015. **784**: p. 172-175.
44. Shea, D.A. and D.L. Morgan, *The helium-3 shortage: Supply, demand, and options for congress*. 2010, Congressional Research Service Washington, DC.
45. Lukosi, E., et al., *Lithium indium diselenide: A new scintillator for neutron imaging.* 2016. **830**: p. 140-149.

46. Gallagher, J., et al. *Neutron imaging with lithium indium diselenide semiconductors*. in *2020 IEEE Nuclear Science Symposium and Medical Imaging Conference (NSS/MIC)*. 2021. IEEE.
47. Lowe, B.G. and R.A. Sareen, *Semiconductor X-ray detectors*. 2014: CRC Press Boca Raton, Fl.
48. Owens, A., *Compound semiconductor radiation detectors*. 2016: Taylor & Francis.
49. Devanathan, R., et al., *Signal variance in gamma-ray detectors—A review.* 2006. **565**(2): p. 637-649.
50. Lukosi, E., et al., *Response functions of semiconducting lithium indium diselenide.* 2016. **822**: p. 9-14.
51. Owens, A., A.J. Peacock, and M. Bavdaz. *Progress in compound semiconductors*. in *X-Ray and Gamma-Ray Telescopes and Instruments for Astronomy*. 2003. SPIE.
52. Tsoulfanidis, N. and S. Landsberger, *Measurement & detection of radiation*. 2021: CRC press.
53. Cowen, A., A. Davies, and M.J.C.R. Sivananthan, *The design and imaging characteristics of dynamic, solid-state, flat-panel x-ray image detectors for digital fluoroscopy and fluorography.* 2008. **63**(10): p. 1073-1085.
54. Mirzaei, A., et al., *Room temperature hard radiation detectors based on solid state compound semiconductors: an overview.* 2018. **14**(3): p. 261-287.
55. Cao, R.L., et al., *The measurement of the presampled MTF of a high spatial resolution neutron imaging system.* 2007. **582**(2): p. 621-628.
56. Bossi, R., J. Cason, and C. Jackson Jr, *MODULATION TRANSFER FUNCTION AND EFFECTIVE FOCAL SPOT AS RELATED TO NEUTRON RADIOGRAPHY*. 1972, Hanford Engineering Development Lab., Richland, WA (United States).
57. Herrera, E., et al., *Neutron imaging with timepix coupled lithium indium diselenide.* 2018. **4**(1): p. 10.
58. Rossmann, K.J.R., *Point spread-function, line spread-function, and modulation transfer function: tools for the study of imaging systems.* 1969. **93**(2): p. 257-272.
59. Jerri, A.J.J.P.o.t.I., *The Shannon sampling theorem—Its various extensions and applications: A tutorial review.* 1977. **65**(11): p. 1565-1596.

60. Hamm, D.S., et al., *Semiconducting lithium indium diselenide: Charge-carrier properties and the impacts of high flux thermal neutron irradiation.* 2018. **112**(24): p. 242104.
61. Lukosi, E., et al., *Intrinsic lithium indium diselenide: Scintillation properties and defect states.* 2019. **205**: p. 346-350.
62. Tremsin, A.S., et al., *Non-destructive study of bulk crystallinity and elemental composition of natural gold single crystal samples by energy-resolved neutron imaging.* 2017. **7**(1): p. 1-9.
63. Tremsin, A., et al., *Neutron resonance transmission spectroscopy with high spatial and energy resolution at the J-PARC pulsed neutron source.* 2014. **746**: p. 47-58.
64. Timothy, J.G.J.R.o.S.I., *Curved-channel microchannel array plates.* 1981. **52**(8): p. 1131-1142.
65. Siegmund, O., et al., *Large area event counting detectors with high spatial and temporal resolution.* 2014. **9**(04): p. C04002.
66. Tremsin, A. and J.J.R.M. Vallerga, *Unique capabilities and applications of Microchannel Plate (MCP) detectors with Medipix/Timepix readout.* 2020. **130**: p. 106228.
67. Tremsin, A., J. Vallerga, and O.J.R.o.S.I. Siegmund, *"Detector walk" in position-sensitive detectors with biased microchannel plates.* 2000. **71**(10): p. 3758-3761.
68. Tremsin, A.S., et al., *Photon-counting MCP/Timepix detectors for soft X-ray imaging and spectroscopic applications.* 2021. **28**(4).
69. Llopart, X., et al., *Timepix4, a large area pixel detector readout chip which can be tiled on 4 sides providing sub-200 ps timestamp binning.* 2022. **17**(01): p. C01044.
70. Tremsin, A.S., et al., *High Resolution Photon Counting With MCP-Timepix Quad Parallel Readout Operating at $> 1~{\rm KHz} $ Frame Rates.* 2012. **60**(2): p. 578-585.
71. Lukosi, E., et al. *Investigation of a Lithium Indium Diselenide detector for neutron transmission imaging*. in *Hard X-Ray, Gamma-Ray, and Neutron Detector Physics XVI*. 2014. SPIE.
72. Ballabriga, R., et al., *Asic developments for radiation imaging applications: The medipix and timepix family.* 2018. **878**: p. 10-23.
73. Yule, H., et al., *Utilization of reactor fast neutrons for activation analysis.* 1965. **33**(2): p. 277-282.

74. Tremsin, A., et al., *Non-contact measurement of partial gas pressure and distribution of elemental composition using energy-resolved neutron imaging.* 2017. **7**(1): p. 015315.
75. Frano, R.L., G. Pugliese, and G.J.E. Forasassi, *Thermal analysis of a spent fuel cask in different transport conditions.* 2011. **36**(4): p. 2285-2293.
76. Tremsin, A.S., et al., *Neutron radiography with sub-15 μm resolution through event centroiding.* 2012. **688**: p. 32-40.
77. Ehlers, G., A.A. Podlesnyak, and A.I.J.R.o.S.I. Kolesnikov, *The cold neutron chopper spectrometer at the Spallation Neutron Source—A review of the first 8 years of operation.* 2016. **87**(9): p. 093902.
78. Tremsin, A.S., et al., *In-situ observation of phase separation during growth of Cs2LiLaBr6: Ce crystals using energy-resolved neutron imaging.* 2017. **17**(12): p. 6372-6381.
79. Strobl, M., et al., *Time-of-flight neutron imaging for spatially resolved strain investigations based on Bragg edge transmission at a reactor source.* 2012. **680**: p. 27-34.
80. Tremsin, A.S., et al., *Investigation of dissimilar metal welds by energy-resolved neutron imaging.* 2016. **49**(4): p. 1130-1140.
81. Kabra, S., et al. *Energy-dispersive neutron imaging and diffraction of magnetically driven twins in a Ni2MnGa single crystal magnetic shape memory alloy*. in *Journal of Physics: Conference Series*. 2016. IOP Publishing.
82. Sun, T., et al., *Investigation of residual stress distribution and texture evolution in AA7050 stationary shoulder friction stir welded joints.* 2018. **712**: p. 531-538.
83. Cereser, A., et al., *Time-of-flight three dimensional neutron diffraction in transmission mode for mapping crystal grain structures.* 2017. **7**(1): p. 1-11.
84. Rossi, L., et al., *Pixel detectors: From fundamentals to applications*. 2006: Springer Science & Business Media.
85. Belau, E., et al., *Charge collection in silicon strip detectors.* 1983. **214**(2-3): p. 253-260.
86. He, Z.J.N.I., S. Methods in Physics Research Section A: Accelerators, Detectors, and A. Equipment, *Review of the Shockley–Ramo theorem and its application in semiconductor gamma-ray detectors.* 2001. **463**(1-2): p. 250-267.

87. Affolder, A., et al., *Silicon detectors for the sLHC.* 2011. **658**(1): p. 11-16.
88. Köhler, M.J.F.o.P. and Mathematics, *Double-sided 3D silicon detectors for the High-Luminosity LHC.* 2011.
89. Kohler, M., et al., *Beam test measurements with planar and 3D silicon strip detectors irradiated to sLHC fluences.* 2011. **58**(3): p. 1308-1314.
90. Zoboli, A., et al., *Double-sided, double-type-column 3-D detectors: design, fabrication, and technology evaluation.* 2008. **55**(5): p. 2775-2784.
91. Aad, G., et al., *The ATLAS experiment at the CERN large hadron collider.* 2008. **3**: p. S08003.
92. Matei, L., et al., *Lithium indium diselenide—An advanced material for neutron detection.* 2021. **1020**: p. 165898.
93. Siemek, K., et al., *Optical and positron annihilation studies of structural defects in LiInSe2 single crystals.* 2020. **109**: p. 110262.
94. Badikov, V., et al., *Optical properties of lithium indium selenide.* 2003. **23**(3-4): p. 575-581.
95. Golduber, R., et al., *Evaluation of Neutron-Radiation Tolerance of Lithium Indium Diselenide Semiconductors.* 2023.
96. Isaenko, L.I., et al. *Growth and characterization of single crystals of ternary chalcogenides for laser applications*. in *International Conference on Solid State Crystals 2000: Growth, Characterization, and Applications of Single Crystals*. 2001. SPIE.
97. Kamijoh, T. and K.J.J.o.C.G. Kuriyama, *Single crystal growth and characterization of LiInSe2.* 1981. **51**(1): p. 6-10.
98. Stowe, A., et al., *Crystal growth in LiGaSe2 for semiconductor radiation detection applications.* 2013. **379**: p. 111-114.
99. Neyman, M. and K. Sadilenko, *Thermonuclear Weapons*. 1960, FOREIGN TECHNOLOGY DIV WRIGHT-PATTERSON AFB OH.
100. Johns, P.M. and J.C.J.J.o.A.P. Nino, *Room temperature semiconductor detectors for nuclear security.* 2019. **126**(4): p. 040902.
101. Lutz, G., *Semiconductor radiation detectors*. 2007: Springer.
102. Lukosi, E.D., et al., *Neutron imaging with lithium indium diselenide: Surface properties, spatial resolution, and computed tomography.* 2017. **872**: p. 181-186.

103. Persons, T. and G.J.U.S.G.A.O.G.-.-. Aloise, *Neutron detectors: Alternatives to using helium-3.* 2011.
104. Ziegler, J.F., et al., *SRIM–The stopping and range of ions in matter (2010).* 2010. **268**(11-12): p. 1818-1823.
105. Pal, K. and B.V. Patel. *Data classification with k-fold cross validation and holdout accuracy estimation methods with 5 different machine learning techniques*. in *2020 fourth international conference on computing methodologies and communication (ICCMC)*. 2020. IEEE.
106. Faber, N.K.M.J.C. and I.L. Systems, *Estimating the uncertainty in estimates of root mean square error of prediction: application to determining the size of an adequate test set in multivariate calibration.* 1999. **49**(1): p. 79-89.
107. Council, N.R., *Improving Information for Social Policy Decisions--The Uses of Microsimulation Modeling: Volume I, Review and Recommendations*. Vol. 1. 1991: National Academies Press.
108. Holmén, G. and H.J.J.o.a.p. Jacobsson, *The influence of oxygen on SiO2 sputtering.* 1990. **68**(6): p. 2962-2965.
109. Jones, R., et al., *Effect of Oxygen on the rf-Sputtering Rate of SiO 2.* 1968. **5**(3): p. 84-87.
110. Wang, C.-L. and R.A.J.R.o.S.I. Riedel, *Improved neutron-gamma discrimination for a 6Li-glass neutron detector using digital signal analysis methods.* 2016. **87**(1): p. 013301.

APPENDIX

Overview

This section is to act as a review for radiation interactions with matter. It is essential to understand what goes into neutron/gamma discrimination by determining the mode of interaction and expected energy of the neutrons and gamma rays. Radiation can be broken down into two different types: ionizing or non-ionizing. Non-ionizing refers to a type of low-energy radiation that does not have enough energy to remove an electron from an atom; this means they do not have enough energy to cause a significant effect on materials. Unlike non-ionizing radiation, ionizing radiation has enough energy to remove electrons from atoms and molecules of materials. Ionizing radiation can be further broken down into two more categories: directly ionizing radiation and indirectly ionizing radiation.

Ionizing Radiation

Directly ionizing radiation refers to electrically charged particles such as electrons, protons, alpha particles, and fission fragments with sufficient kinetic energy to produce ionization by collisions—each interaction by these particles with matter cause the particle to lose energy until it is eventually stopped. Since larger particles will interact more frequently within a material, they will have a shorter range. When comparing the range of an alpha particle to a triton in the same material, the triton will travel much further than the triton because it is smaller.

Photon Interactions with Matter

Indirectly ionizing radiation ionizes the medium it interacts with through secondary reactions and typically refers to interactions by photons or neutrons with matter. Photons consist of both X-rays and gamma-rays, which interact in identical ways. The only difference is where they originate from. Gamma rays originate from the atom's nucleus,

and X-rays are generated from the electron shells. Photon interactions can be broken down into three main categories, as shown in Figure 60, which will be discussed in further detail.

Photoelectric Effect

The photoelectric effect is typically described as a low-energy phenomenon that consists of the emission of electrons when a photon, such as light, interacts with the atoms in a medium and produces photoelectrons from an inner shell. The energy of the ejected photoelectron (E_e) is determined by Equation (17), where E is the energy of the incident photon and E_b is the binding energy of the electron shell [38]. After an inner shell electron ejects, the vacancy is typically filled by an outer shell electron. The photoelectric effect is the primary mode of interaction for low-energy gamma and X-rays.

$$E_e = E - E_b \tag{17}$$

Compton Scattering

Compton scattering is typically described as a mid-energy phenomenon where a photon is scattered off a free electron. As can be seen in Figure 61, the incoming (Incident) photon transfers a portion of its energy to the electron, called a Recoil electron. Equation (18) is used to describe the energy of the scattered electron as a function of the incident photon energy, E in MeV, and photon scattering angle, θ_s. The value of 0.511 is the rest mass of an electron in MeV. Since the scattering angle of the photon is a stochastic property, it can range between 0º (minimum energy transfer) to 180º (maximum energy transfer). As a result of this, the resulting electron energy can vary from 0 MeV to transfer). As a result of this, the resulting electron energy can vary from 0 MeV to E_e, found using Equation (18).

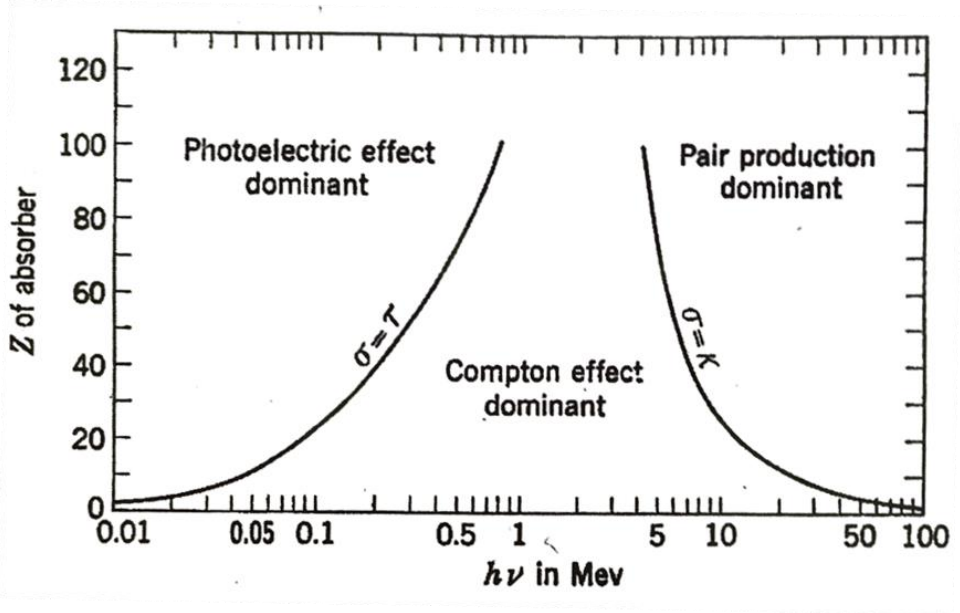

Figure 60. The relative importance of the three major types of gamma-ray interactions: photoelectric effect, Compton effect, and pair production as a function of atomic number and photon energy. The lines show the values of Z and $h\nu$ for which the two neighboring effects are just equal [38].

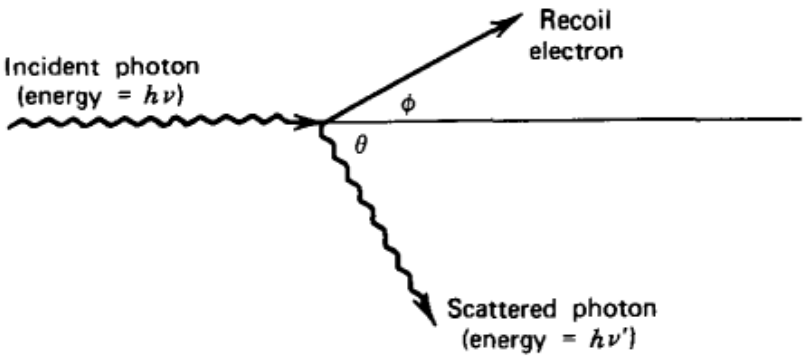

Figure 61. A schematic that relates the energy transfer and the scattering angle for any given interaction [31].

$$E_e = E\left[1 - \frac{1}{1 + \frac{E}{0.511}(1 - cos\theta_s)}\right] \quad (18)$$

Since the probability of Compton scattering depends on the number of electrons available as scattering targets, it increases linearly with the atomic number, Z.

Pair Production

Pair production is possible when the photon's energy exceeds 1.022 MeV, which is twice the rest mass of an electron. The probability of this interaction occurring is low until the photon energy reaches several MeV. Pair production is the phenomenon where the nucleus absorbs the photon and is replaced by an electron-positron pair. All excess kinetic energy carried by the photon (E_γ) is divided evenly between the electron (E_{e-}) and positron (E_{e+}), seen below in Equation (19). It is worth noting that 1.022 MeV of the photon's energy is used to create the masses of the electron and position. Since the positron typically annihilates as it slows down in the medium, it will produce two photons moving in opposite directions, each with an energy of 0.511 MeV.

$$E_\gamma = E_{e+} + E_{e-} \quad (19)$$

Photonuclear Reaction

The photonuclear reaction is the absorption of a highly energetic photon into the atomic nucleus. This can result in the emission of nucleons, protons, or heavy charged particles. The reaction can occur for photons typically ranging from 10 MeV to 30 MeV. Photons with these energy levels are normally only seen in an accelerator, so it is not of great interest for neutron imaging.

VITA

Jake Gallagher was born in Louisiana and received his Bachelor of Science degree in chemical engineering from the University of Missouri-Columbia in December of 2018, and worked for the University of Missouri Research Reactor until August of 2019, where he began his dissertation research for his Ph.D. in nuclear engineering at the University of Tennessee-Knoxville (UTK) under the advisement of Dr. Eric Lukosi. While at UTK, Jake also received a Masters of Science degree in nuclear engineering in 2022. He has experience working at the University of Missouri Chemistry Department, University of Missouri Research Reactor, and Y-12 National Security Complex in radiochemistry, neutron imaging, and nuclear nonproliferation, and has received the NRC University Nuclear Leadership Program Fellowship and STEPS Fellowship.